Pertanika Journal of

SCIENCE & TECHNOLOGY

VOL. 33 (S2) 2025

A Special Issue devoted to
Applied Engineering and Science

Guest Editors
Tohru Kamiya, Kentaro Kitamura and Yoshito Ando

PERTANIKA
JOURNALS

A scientific journal published by Universiti Putra Malaysia Press

PERTANIKA JOURNAL OF SCIENCE & TECHNOLOGY

About the Journal

Overview

Pertanika Journal of Science & Technology is an official journal of Universiti Putra Malaysia. It is an open-access online scientific journal. It publishes original scientific outputs. It neither accepts nor commissions third party content.

Recognised internationally as the leading peer-reviewed interdisciplinary journal devoted to the publication of original papers, it serves as a forum for practical approaches to improve quality on issues pertaining to science and engineering and its related fields.

Pertanika Journal of Science & Technology currently publishes 6 issues a year (*January, March, April*, *July, August,* and *October*). It is considered for publication of original articles as per its scope. The journal publishes in **English** and it is open for submission by authors from all over the world.

The journal is available world-wide.

Aims and scope

Pertanika Journal of Science & Technology aims to provide a forum for high quality research related to science and engineering research. Areas relevant to the scope of the journal include: bioinformatics, bioscience, biotechnology and bio-molecular sciences, chemistry, computer science, ecology, engineering, engineering design, environmental control and management, mathematics and statistics, medicine and health sciences, nanotechnology, physics, safety and emergency management, and related fields of study.

History

Pertanika Journal of Science & Technology was founded in 1993 and focuses on research in science and engineering and its related fields.

Vision

To publish a journal of international repute.

Mission

Our goal is to bring the highest quality research to the widest possible audience.

Quality

We aim for excellence, sustained by a responsible and professional approach to journal publishing. Submissions can expect to receive a decision within 90 days. The elapsed time from submission to publication for the articles averages 180 days. We are working towards decreasing the processing time with the help of our editors and the reviewers.

Abstracting and indexing of Pertanika

Pertanika Journal of Science & Technology is now over 33 years old; this accumulated knowledge and experience has resulted the journal being abstracted and indexed in SCOPUS (Elsevier), Journal Citation Reports (JCR-Clarivate), EBSCO, ASEAN CITATION INDEX, Microsoft Academic, Google Scholar, and MyCite.

Citing journal articles

The abbreviation for Pertanika Journal of Science & Technology is *Pertanika J. Sci. & Technol.*

Publication policy

Pertanika policy prohibits an author from submitting the same manuscript for concurrent consideration by two or more publications. It prohibits as well publication of any manuscript that has already been published either in whole or substantial part elsewhere. It also does not permit publication of manuscript that has been published in full in proceedings.

Code of Ethics

The *Pertanika* journals and Universiti Putra Malaysia take seriously the responsibility of all of its journal publications to reflect the highest in publication ethics. Thus, all journals and journal editors are expected to abide by the journal's codes of ethics. Refer to *Pertanika*'s **Code of Ethics** for full details, or visit the journal's web link at http://www.pertanika.upm.edu.my/code_of_ethics.php

Originality

The author must ensure that when a manuscript is submitted to *Pertanika*, the manuscript must be an original work. The author should check the manuscript for any possible plagiarism using any program such as Turn-It-In or any other software before submitting the manuscripts to the *Pertanika* Editorial Office, Journal Division.

All submitted manuscripts must be in the journal's acceptable similarity index range:

≤ 20% – PASS; > 20% – REJECT.

International Standard Serial Number (ISSN)

An ISSN is an 8-digit code used to identify periodicals such as journals of all kinds and on all media–print and electronic.

Pertanika Journal of Science & Technology: e-ISSN 2231-8526 (Online).

Lag time

A decision on acceptance or rejection of a manuscript is reached in 90 days (average). The elapsed time from submission to publication for the articles averages 180 days.

Authorship

Authors are not permitted to add or remove any names from the authorship provided at the time of initial submission without the consent of the journal's Chief Executive Editor.

Manuscript preparation

For manuscript preparation, authors may refer to Pertanika's **INSTRUCTION TO AUTHORS**, available on the official website of *Pertanika*.

Editorial process

Authors who complete any submission are notified with an acknowledgement containing a manuscript ID on receipt of a manuscript, and upon the editorial decision regarding publication.

Pertanika follows a **double-blind peer-review** process. Manuscripts deemed suitable for publication are sent to reviewers. Authors are encouraged to suggest names of at least 3 potential reviewers at the time of submission of their manuscripts to *Pertanika*, but the editors will make the final selection and are not, however, bound by these suggestions.

Notification of the editorial decision is usually provided within 90 days from the receipt of manuscript. Publication of solicited manuscripts is not guaranteed. In most cases, manuscripts are accepted conditionally, pending an author's revision of the material.

The journal's peer review

In the peer-review process, 2 to 3 referees independently evaluate the scientific quality of the submitted manuscripts. At least 2 referee reports are required to help make a decision.

Peer reviewers are experts chosen by journal editors to provide written assessment of the **strengths** and **weaknesses** of written research, with the aim of improving the reporting of research and identifying the most appropriate and highest quality material for the journal.

Operating and review process

What happens to a manuscript once it is submitted to *Pertanika*? Typically, there are 7 steps to the editorial review process:

1. The journal's Chief Executive Editor and the Editor-in-Chief examine the paper to determine whether it is relevance to journal needs in terms of novelty, impact, design, procedure, language as well as presentation and allow it to proceed to the reviewing process. If not appropriate, the manuscript is rejected outright and the author is informed.
2. The Chief Executive Editor sends the article-identifying information having been removed, to 2 to 3 reviewers. They are specialists in the subject matter of the article. The Chief Executive Editor requests that they complete the review within 3 weeks.

   Comments to authors are about the appropriateness and adequacy of the theoretical or conceptual framework, literature review, method, results and discussion, and conclusions. Reviewers often include suggestions for strengthening of the manuscript. Comments to the editor are in the nature of the significance of the work and its potential contribution to the research field.

3. The Editor-in-Chief examines the review reports and decides whether to accept or reject the manuscript, invite the authors to revise and resubmit the manuscript, or seek additional review reports. In rare instances, the manuscript is accepted with almost no revision. Almost without exception, reviewers' comments (to the authors) are forwarded to the authors. If a revision is indicated, the editor provides guidelines for attending to the reviewers' suggestions and perhaps additional advice about revising the manuscript.
4. The authors decide whether and how to address the reviewers' comments and criticisms and the editor's concerns. The authors return a revised version of the paper to the Chief Executive Editor along with specific information describing how they have addressed' the concerns of the reviewers and the editor, usually in a tabular form. The authors may also submit a rebuttal if there is a need especially when the authors disagree with certain comments provided by reviewers.
5. The Chief Executive Editor sends the revised manuscript out for re-review. Typically, at least 1 of the original reviewers will be asked to examine the article.
6. When the reviewers have completed their work, the Editor-in-Chief examines their comments and decides whether the manuscript is ready to be published, needs another round of revisions, or should be rejected. If the decision is to accept, the Chief Executive Editor is notified.
7. The Chief Executive Editor reserves the final right to accept or reject any material for publication, if the processing of a particular manuscript is deemed not to be in compliance with the S.O.P. of *Pertanika*. An acceptance letter is sent to all the authors.

The editorial office ensures that the manuscript adheres to the correct style (in-text citations, the reference list, and tables are typical areas of concern, clarity, and grammar). The authors are asked to respond to any minor queries by the editorial office. Following these corrections, page proofs are mailed to the corresponding authors for their final approval. At this point, **only essential changes are accepted**. Finally, the manuscript appears in the pages of the journal and is posted on-line.

Pertanika Journal of

SCIENCE & TECHNOLOGY

A Special Issue devoted to
Applied Engineering and Science

Vol. 33 (S2) 2025

Guest Editors
Tohru Kamiya, Kentaro Kitamura and Yoshito Ando

A scientific journal published by Universiti Putra Malaysia Press

PJST
Pertanika Journal of Science & Technology
AN INTERNATIONAL PEER-REVIEWED JOURNAL

EDITOR-IN-CHIEF
Luqman Chuah Abdullah
Chemical Engineering

CHIEF EXECUTIVE EDITOR

UNIVERSITY PUBLICATIONS COMMITTEE

CHAIRMAN
Zamberi Sekawi

EDITORIAL STAFF
Journal Officers:
Ellyianur Puteri Zainal
Kanagamalar Silvarajoo
Siti Zuhaila Abd Wahid

Editorial Assistants:
Siti Juridah Mat Arip
Zulinaardawati Kamarudin

English Editor:
Norhanizah Ismail

PRODUCTION STAFF
Pre-press Officers:
Ku Ida Mastura Ku Baharom
Nur Farrah Dila Ismail

WEBMASTER
IT Officer:
Kiran Raj Kaneswaran

EDITORIAL OFFICE
JOURNAL DIVISION
Putra Science Park
1st Floor, IDEA Tower II
UPM-MTDC Technology Centre
Universiti Putra Malaysia
43400 Serdang, Selangor Malaysia.

General Enquiry
Tel. No: +603 9769 1622 | 1616
E-mail:
executive_editor.pertanika@upm.edu.my
URL: http://www.pertanika.upm.edu.my

PUBLISHER
UPM Press
Universiti Putra Malaysia
43400 UPM, Serdang, Selangor, Malaysia.
Tel: +603 9769 8855
E-mail: dir.penerbit@upm.edu.my
URL: http://penerbit.upm.edu.my

ASSOCIATE EDITOR
2024-2026

Miss Laiha Mat Kiah
Security Services Sn: Digital Forensic, Steganography, Network Security, Information Security, Communication Protocols, Security Protocols
Universiti Malaya, Malaysia

Saidur Rahman
Renewable Energy, Nanofluids, Energy Efficiency, Heat Transfer, Energy Policy
Sunway University, Malaysia

EDITORIAL BOARD
2024-2026

Abdul Latif Ahmad
Chemical Engineering
Universiti Sains Malaysia, Malaysia

Ahmad Zaharin Aris
Hydrochemistry, Environmental Chemistry, Environmental Forensics, Heavy Metals
Universiti Putra Malaysia, Malaysia

Azlina Harun@ Kamaruddin
Enzyme Technology, Fermentation Technology
Universiti Sains Malaysia, Malaysia

Bassim H. Hameed
Chemical Engineering: Reaction Engineering, Environmental Catalysis & Adsorption
Qatar University, Qatar

Biswajeet Pradhan
Digital image processing, Geographical Information System (GIS), Remote Sensing
University of Technology Sydney, Australia

Ho Yuh-Shan
Water research, Chemical Engineering and Environmental Studies
Asia University, Taiwan

Hsiu-Po Kuo
Chemical Engineering
National Taiwan University, Taiwan

Ivan D. Rukhlenko
Nonliner Optics, Silicon Photonics, Plasmonics and Nanotechnology
The University of Sydney, Australia

Lee Keat Teong
Energy Environment, Reaction Engineering, Waste Utilization, Renewable Energy
Universiti Sains Malaysia, Malaysia

Mohamed Othman
Communication Technology and Network, Scientific Computing
Universiti Putra Malaysia, Malaysia

Mohd Shukry Abdul Majid
Polymer Composites, Composite Pipes, Natural Fibre Composites, Biodegradable Composites, Bio-Composites
Universiti Malaysia Perlis, Malaysia

Mohd Zulkifly Abdullah
Fluid Mechanics, Heat Transfer, Computational Fluid Dynamics (CFD)
Universiti Sains Malaysia, Malaysia

Mohd. Ali Hassan
Bioprocess Engineering, Environmental Biotehnology
Universiti Putra Malaysia, Malaysia

Nor Azah Yusof
Biosensors, Chemical Sensor, Functional Material
Universiti Putra Malaysia, Malaysia

Norbahiah Misran
Communication Engineering
Universiti Kebangsaan Malaysia, Malaysia

Roslan Abd-Shukor
Physics & Materials Physics, Superconducting Materials
Universiti Kebangsaan Malaysia, Malaysia

Sodeifian Gholamhossein
Supercritical technology, Optimization, nanoparticles, Polymer nanocomposites
University of Kashan, Iran

Wing Keong Ng
Aquaculture, Aquatic Animal Nutrition, Aqua Feed Technology
Universiti Sains Malaysia, Malaysia

INTERNATIONAL ADVISORY BOARD
2024-2027

Hiroshi Uyama
Polymer Chemistry, Organic Compounds, Coating, Chemical Engineering
Osaka University, Japan

Mohamed Pourkashanian
Mechanical Engineering, Energy, CFD and Combustion Processes
Sheffield University, United Kingdom

Mohini Sain
Material Science, Biocomposites,Biomaterials
University of Toronto, Canada

Yulong Ding
Particle Science & Thermal Engineering
University of Birmingham, United Kingdom

ABSTRACTING AND INDEXING OF PERTANIKA JOURNALS

Pertanika Journal of Science & Technology is indexed in Journal Citation Reports (JCR-Clarivate), SCOPUS (Elsevier), EBSCO, ASEAN Citation Index, Microsoft Academic, Google Scholar and MyCite.

The publisher of Pertanika will not be responsible for the statements made by the authors in any articles published in the journal. Under no circumstances will the publisher of this publication be liable for any loss or damage caused by your reliance on the advice, opinion or information obtained either explicitly or implied through the contents of this publication.
All rights of reproduction are reserved in respect of all papers, articles, illustrations, etc., published in Pertanika. Pertanika provides free access to the full text of research articles for anyone, web-wide. It does not charge either its authors or author-institution for refereeing/publishing outgoing articles or user-institution for accessing incoming articles.
No material published in Pertanika may be reproduced or stored on microfilm or in electronic, optical or magnetic form without the written authorization of the Publisher.
Copyright ©2021 Universiti Putra Malaysia Press. All Rights Reserved.

Pertanika Journal of Science & Technology
Vol. 33 (S2) 2025

Contents

Preface

The 2023 11th International Symposium on Applied Engineering and Sciences (SAES 2023) was held successfully at the Universiti Putra Malaysia (UPM) from 20th–21st November 2023, hosted by UPM. SAES has provided a unique platform for researchers, students, scientists, and engineers to share their knowledge and latest research since 2013. After three years of virtual meetings (SAES2020, 2021, and 2022) due to the pandemic, SAES2023 was held physically and provided various opportunities to expand the international academic network and enhance academic collaborations.

We are pleased to introduce this special edition of the PERTANIKA Journal of the 11th International Symposium on Applied Engineering and Sciences (SAES2023), focusing on the intersection of applied engineering and sciences.

The five articles in this edition represent diverse research, insights, and practices from scholars. They investigate topics such as the design of a stimuli-responsive surface, numerical analysis of the load-carrying capacity, sharing electricity using photovoltaic panels and storage batteries, ceiling-hanging panels and their impact, and dynamic hand gesture recognition. As editors, we believe this collection will contribute significantly to engineering and science.

We sincerely thank the authors for contributing their expertise and perspective to this special edition. We also thank the reviewers and editorial team members, Dr. Yoshito Ando and Dr. Kentaro Kitamura, who have dedicated their time to ensuring the quality and relevance of the published works. We hope that you will find this useful for your research.

Warm regards.

Guest Editors
Tohru Kamiya (Prof. Dr.)
Kentaro Kitamura (Prof. Dr.)
Yoshito Ando (Prof. Dr.)

Pertanika J. Sci. & Technol. 33 (S2): 1 - 11 (2025)

SCIENCE & TECHNOLOGY

Journal homepage: http://www.pertanika.upm.edu.my/

Design of Stimuli-responsive Surface for Reversible Wettability Switching by Vapor-Phase Assisted Photo-polymerization

Yoshito Andou[1,2]* and Wang Ruozhu[1]

[1]*Graduate School of Life Science and Systems Engineering, Kyushu Institute of Technology, 2-4 Hibikino Wakamatsu-ku, Kitakyushu, Fukuoka 808-0196, Japan*

[2]*Collaborative Research Centre for Green Materials on Environmental Technology, Kyushu Institute of Technology, 2-4 Hibikino, Wakamatsu, Kitakyushu, Fukuoka 808-0196, Japan*

ABSTRACT

In exploring the development of stimuli-responsive surfaces capable of reversible wettability switching, our study delved into the efficacy of vapor-phase-assisted surface photo-polymerization (photo-VASP). This innovative approach modulated Si-wafer and cotton surfaces' chemical and physical attributes. The method involved strategically using a blend of hydrophobic and hydrophilic vinyl monomers, enabling fine-tuning surface properties. By carefully selecting monomer combinations, we achieved seamless copolymerization, effectively grafting the polymers onto the surfaces. The efficacy of this grafting process was validated through contact angle measurements post-solvent extraction of unattached polymers. Crucially, the surfaces engineered through this process demonstrated a remarkable capacity for reversible wettability switching, a feature dynamically controlled by the application and removal of external stimuli. This capability underscores the potential of our approach in creating advanced functional surfaces with tunable properties.

Keywords: Hydrophilic-hydrophobic property, photo-polymerization, stimuli-responsive, vapor-phase assisted surface polymerization (VASP)

ARTICLE INFO

Article history:
Received: 13 February 2024
Accepted: 18 October 2024
Published: 25 February 2025

DOI: https://doi.org/10.47836/pjst.33.S2.01

E-mail addresses:
yando@life.kyutech.ac.jp (Yoshito Andou)
wang.ruozhu809@mail.kyutech.jp (Wang Ruozhu)
* Corresponding author

INTRODUCTION

The burgeoning field of surface functionalization on substrates is experiencing a surge in interest, underscored by the critical role of precise surface modifications in diverse areas such as printing, coating, and the utilization of fibers, membranes, and biomedical materials (Xi et al., 2023). The development of advanced materials with responsive surfaces capable

ISSN: 0128-7680
e-ISSN: 2231-8526

of reversible switching between distinct states has garnered significant attention. Such precise control over the functionalities at the interface can be achieved through reversible chemical reactions involving both covalent and non-covalent bonds. This enables the tuning of properties in two-dimensional or three-dimensional structures with spatial and temporal accuracy. These sophisticated techniques for reversible manipulation of surfaces have become a focal point of research, holding immense potential for applications in controlled drug release, chromatographic separations, enhanced oil recovery, and optical switching (Chenglong et al., 2023; Guan et al., 2020; Mostafavi et al., 2023; Nagase et al., 2009; Onome et al., 2023; Thang et al., 2023). Researchers have successfully created "adaptive" or "active" surfaces that exhibit dual hydrophobic-hydrophilic behavior in response to stimuli like pH, temperature, or both, utilizing polymer brushes (Lin et al., 2022). These "stimuli-responsive" polymers undergo an abrupt change in properties, such as conformation or solubility, upon exposure to external stimuli like solvent, temperature, or pH. This dynamic alteration of interfacial properties like wettability in response to stimuli such as electrical potentials represents a leap forward in material science, robotics, and electronics (Brotherton et al., 2023).

The functional groups or radicals already present are employed in the following procedure to covalently link polymer chains to enhance substrate surfaces without altering the content. Immobilization of polymer chains onto a solid surface is mainly achieved through two methods: (1) the "grafting to" approach, which attaches pre-existing chains to surface-active groups via chemical reactions, as detailed by researchers such as Maity and Dawn (2020) and Wang et al. (2020); (2) the "grafting from" strategy that initiates the polymerization of monomers directly from the surface, noted by Gouget-Laemmel et al. (2023) and Higaki et al. (2018). Nevertheless, controlled functionalization of polymer surfaces poses a significant challenge, with these surface modification techniques often facing drawbacks like limited control over the chemical composition or mechanical discrepancies in the top layer leading to potential delamination, as observed by Hester et al. (1999).

A unique approach, the vapor-phase-assisted surface polymerization (VASP) technique, has been recognized as an effective method for generating microarchitectures on solid substrate surfaces. Highlighted by its solvent-free nature and precision (Andou et al., 2006, 2007; Chan & Gleason, 2005; Fu et al., 2002; Gu et al., 2003; Lau & Gleason, 2006; Wang & Chang, 2003; Yasutake et al., 2003), VASP offers additional advantages conducive to creating intricately structured composites (Nishida et al., 2005) and coatings (Gupta et al., 2008; Lau et al., 2003). This is achieved through the diffusion and adsorption of vaporized monomers onto the substrate's interstitial surfaces, where they polymerize in a "pseudo-grafting from" fashion. This process fosters the growth of polymer chains that fill in the gaps, ensuring a robust anchoring effect and exceptional binding strength at the polymer/

substrate boundary. Moreover, integrating physically controlled VASP with photo-induced polymerization has been a focus, leading to the generation of block copolymers through the covalent attachment of azo-type free-radical initiators to Si-wafers.

In this study, we describe the preparation of stimuli-responsive surfaces that contain both hydrophilic and hydrophobic segments on the surface, utilizing the vapor-phase assisted photo-polymerization (Photo-VASP) technique.

MATERIALS AND METHODS

Reagents

(3-Aminopropyl) trimethoxysilane (purchased from DAIKIN FINECHEMICAL LABORATORY, LTD. in Japan) and 2,2,2,3,3-pentafluoropropylmethacrylate (FMA) (also from DAIKIN FINECHEMICAL LABORATORY, LTD., Japan) were purified by distillation immediately before use. Acrylic acid (AA) (obtained from Wako Fujifilm, Japan) underwent the same purification process. 4-*tert*-butylprocatechol (Tokyo Kasei Kogyo Co. Ltd., Japan) was used as received without further purification. Ethylene glycol dimethacrylate (EGDMA), 2-Hydroxyethyl methacrylate (HEMA), and benzoin isobutyl ether (BIBE) (all purchased from Sigma-Aldrich) were purified by distillation before use. All other solvents were commercially available and underwent purification by distillation prior to use.

Typical Polymerization Method

The homopolymerization of FMA was conducted using an H-shaped glass reactor with a vacuum cock, a quartz cap for sealing, and a glass filter separator (pore size 20–30 μm) at the bridge. Photopolymerization was carried out through a 5320 W high-pressure mercury lamp (MORITEX Co., MUV-202-U).

An immobilized azo-type initiator on a 30 mm x 30 mm Si wafer was placed at the bottom of the H-shaped glass tube. FMA (2.0 ml) and 4-*tert*-butylcatechol (20 mg), as a polymerization inhibitor, were introduced via a syringe through the bottom-mounted glass cock under an Ar gas flow. The FMA within the tube underwent three additional freeze-pump-thaw cycles and was then sealed with a quartz cap under vacuum. The reaction proceeded with saturated FMA vapor (94.0 x 10^3 Pa) at 40°C, with UV irradiation directed at the Si-wafer surface through the quartz cap from 10 cm (illumination intensity on the surface was 3.2×10^3 lux through the saturated FMA vapor). After a predetermined reaction time, the product formed on the Si-wafer surface was dried under reduced pressure for 24 hours to remove adsorbed or absorbed monomers. Subsequently, the static contact angle of a water droplet on the product was measured, and the product was dissolved in chloroform for chemical structure analysis using SEM.

Characterization Methods

Fourier transform infrared (FT-IR) spectroscopy was analyzed using a JASCO FTIR 460 Plus spectrometer. The examination of polymers deposited on cotton fabric via scanning electron microscopy (SEM) was executed using a HITACHI S3000N scanning electron microscope, employing an accelerating voltage of 25.0 kV. The static contact angle measurement for water on the samples was conducted using a Drop Master 500 instrument by Kyowa Interface Science Co., Ltd. The contact angle of a water drop (2.0 µl, Milli-Q) was measured at five random points on each sample's surface.

RESULTS AND DISCUSSIONS

In this study, we described the fabrication of stimuli-responsive surfaces with both hydrophilic and hydrophobic segments on the surface using the (Photo-VASP) technique. The development of these stimuli-responsive surfaces was achieved through two approaches: Firstly, a component consisting of 2,2,3,3,3-pentafluoropropylacrylate (FA) as the hydrophobic segment and acrylic acid (AA) as the hydrophilic segment was used to prepare a pH-responsive surface with a block copolymer in several steps (Scheme 1). The preparation of a diblock copolymer on the surface by Photo-VASP, utilizing an azo-type free-radical initiator immobilized on a Si-wafer, has been previously reported and was successfully implemented (Andou et al., 2006). Microscopic reflection absorption FTIR and AFM characterized the block copolymers to evaluate the structure and determine the chemical composition. Secondly, the immobilization of cross-linked copolymer on fabric was achieved using Photo-VASP, a mixture of EGDMA and HEMA with BIBE as a photoinitiator.

To fully leverage the living radical-active species of the VASP method (Yasutake et al., 2003), we attempted the construction of a stimuli-responsive surface through block copolymerization by consecutively applying VASP. In this process, the monomer vapors of FA and AA were sequentially introduced onto the azo-functionalized Si-wafer surface. The photo-VASP of FA with AA was carried out through UV irradiation. Scheme 1

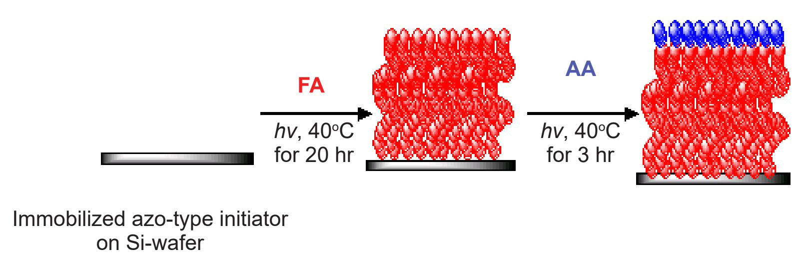

Scheme 1. Poly (FA-*b*-AA) is prepared on a Si surface and immobilized with an azo-type free radical initiator using the consecutive photo-VASP method

outlines constructing a grafted copolymer through this consecutive method. Initially, FA was polymerized on the surface within the reactor tube, after which the FA vapor was evacuated under argon flow. Subsequently, AA was introduced to commence the second stage of photo-VASP. Following photo-VASP, the polymer deposit on the surface was analyzed by SEM with a Backscattered Electron (BSE) detector. As depicted in Figure 1, the photo-VASP resulted in micro-separation composed of poly(FA-*b*-AA) grafted from the Si-wafer surface. Subsequently, free polymer deposits were eliminated through dissolution and washing with a suitable solvent. Compositional SEM analysis with a BSE detector revealed that covalently grafted polymer chains were present. The SEM images showed that the micro-separation structure on the surface disappeared after washing, resulting in a homogeneous surface appearance. This indicates that the micro-separation structure consisted of adsorbed monomers and deposited oligomers, which exhibited different wettability properties.

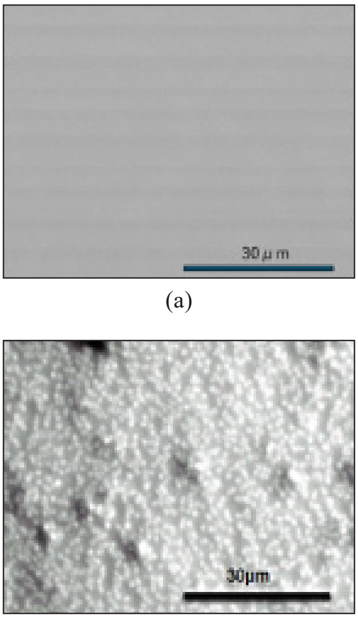

(b)

Figure 1. SEM images of Si-wafer before (a) and after (b) consecutive photo-VASP of FA/AA. Bar 30 μm

To verify the formation of a block copolymer on the surface, the modified Si-wafer surface was assessed by measuring the static contact angle with a water droplet, performed randomly at five points on the surface. The grafted poly (FA-*b*-AA) demonstrated water contact angles of 51° without the need for any external stimuli such as pH changes, suggesting the presence of poly (AA) segments due to the continuous Vapor-phase Assisted Surface Polymerization (VASP) process. In contrast, surfaces with poly (FA) typically exhibited water contact angles 102°.

To alter the surface property to a hydrophilic state, samples were immersed in 0.1M NaOH aqueous solution for several minutes to ionize the carboxyl groups of the AA units. Then, the sample was heated at 100°C under vacuum to transition the surface to a hydrophobic state, during which the carboxyl groups could aggregate and become buried under the flexible PFA chains. These treatments were repeated, with the surface property monitored via static contact angle measurement. The results, presented in Figure 2, illustrate the typical hydrophilic and hydrophobic properties achieved in the first cycle of the process, demonstrating the reversible wettability of the surface. However, the change in surface property was less pronounced after the second cycle. It is believed that the poly (FA) units may gradually hydrolyze in the presence of 0.1 M NaOH aqueous solution, leading to a transition to a completely hydrophilic surface. Thus, selecting more appropriate conditions for external stimulation is necessary to achieve repeatable functionality on the surface.

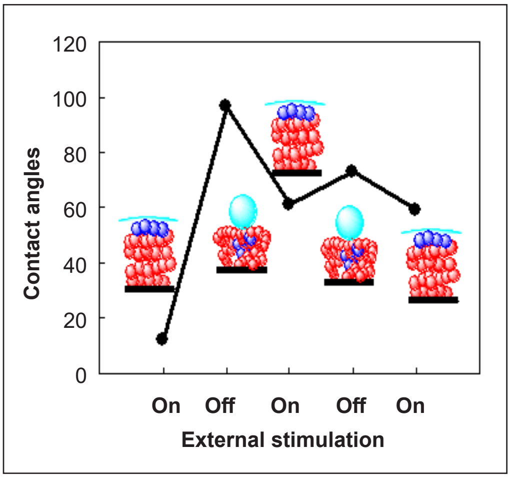

Figure 2. Reversible hydrophobic-hydrophilic conversion of the grafted poly (FA-*b*-AA) on Si-wafer under the cycle of external stimuli. Conditions of external stimuli are as follows: On means that the sample is dipped into 0.1M NaOH aq. Off means that the sample is heated at 100°C in vacuo

Several strategies for achieving reversible wettability switching surfaces have been developed. Depending on the approach, linear and cross-linked amphiphilic polymer layers can be obtained. The architecture of polymer grafts significantly impacts the wettability of a modified surface due to the dynamic motion of the grafted polymer chains with varying architectures (Yakushiji et al., 1998). Liang et al. (2000) reported that cross-linked polymer surfaces exhibit temperature-sensitive characteristics. However, the range of temperature changes is broad, indicating that the surface's sensitivity to temperature is relatively weak.

The second approach introduces a novel method for generating a cross-linked polymer layer on the surface to develop a surface capable of reversible wettability switching. This new method offers two main advantages: it allows for modifying the grafting layer's morphology. It ensures covalently strong bonding with the surface, enabling the substrate to be changed from a Si-wafer to fabric during the VASP process. Cotton fabric, known for its artificial and delicate surface morphology, demonstrates typical surface properties such as wettability, characterized by the smooth absorption of water droplets. It is well-documented that surface roughness significantly influences apparent hydrophobicity through the lotus effect (Jung et al., 2002). Furthermore, Ogiwara et al. (1974) demonstrated that the graft copolymerization of methyl methacrylate on cellulose occurs under UV irradiation. Consequently, surface modification of cotton fabrics by photo-VASP is anticipated to create durable surfaces resistant to external stimuli.

Utilizing BIBE as a photoinitiator, the photo-VASP process of EGDMA, a bifunctional monomer employed for creating cross-linked polymer networks, was performed. Scheme 2 presents a detailed, step-by-step illustration of the anticipated mechanism governing the VASP process under UV irradiation. The procedure initiates with step (a), which involves the distribution and subsequent adsorption of the vaporized initiator on the textile surface. This is followed by step (b), wherein the vapor phase is substituted with monomer molecules. Step (c) comprises the photolysis of the initiator upon UV exposure, leading to steps (c) to (d), during which the active species produced commence the polymerization of the monomer that has been adsorbed on the surfaces. Initially, cotton fabrics of dimensions 35 × 55 mm undergo pre-coating with BIBE via vapor phase adsorption for 1 hour at a temperature of 60°C. Post vapor phase adsorption, these fabrics are exposed to photo-irradiation for 24 hours at 40°C, as delineated in Table 1.

The treated cotton fabrics were subsequently dried in vacuo for 24 hours, and the contact angle with water droplets was measured. The modified cotton surface exhibited high contact angle values of 120° to water droplets, maintaining its hydrophobicity for over 10 minutes. The cotton surface treated with VASP of EGDMA and FMA demonstrated the same high value as those treated solely with VASP of FMA. Thus, EGDMA serves not only as a crosslinker but also as a hydrophobic monomer.

To fabricate a cross-linked copolymer hydrogel on fabric surfaces, photo-VASP of 2-hydroxyethyl methacrylate (HEMA, 1ml) as a hydrophilic monomer and ethylene glycol dimethacrylate (EGDMA, 1ml), with benzoin isobutyl ether (BIBE) as a photoinitiator, was performed. The cotton fabrics, measuring 35 × 55 mm, were initially pre-coated with BIBE via vapor phase adsorption for 1 hour at 80°C, followed by photo-VASP with the monomers for 2 hours at 40°C (Table 1). Subsequently, the cotton fabrics were dried in vacuo for 24 hours. Their contact angles (CA) with water droplets were measured under two conditions: “dry” condition,

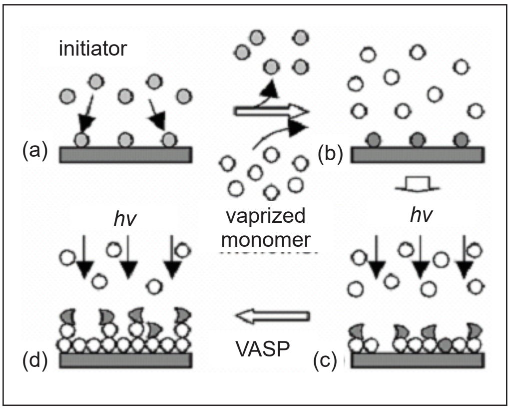

Scheme 2. Mechanism of Photo-VASP process

Table 1

Results of VASP of vinyl monomers on cotton fabric surfaces under UV-irradiation[a]

	1st Step[b]			2nd Step				C.A.[b]	External stimuli	
	BIBE	**Time**	**Temp.**			**Time**	**Temp.**		**Dry**[c]	**Wet**[d]
No.	**(ml)**	**(h)**	**(˚C)**	**Monomers**	**(ml)**	**(h)**	**(˚C)**	**(˚)**	**C.A.**[b] **(˚)**	**C.A.**[b] **(˚)**
1	1	1	80	EGDMA	2	2	40	131	123	126
2	1	1	80	HEMA	2	2	40	0	0	0
3	1	1	80	EGDMA/ HEMA	1/1	2	40	127	134	0

[a] Reaction conditions: initiator adsorption, at 80 °C for 1 hr (BIBE); polymerization of vinyl monomers, at 40 °C under UV irradiation. The distance from the UV lamp to the substrate surface was 10cm. [b] Measured 5 s after setting a water droplet of 2.0 μL on the surface at 25°C. [c] Dry condition indicates heating at 110ºC for 30 min in a drying oven. [d] wet condition indicates exposing to steam at 100ºC for 10 min

where the surface was dried at 110°C for 30 minutes in a drying oven before measuring the CA, and "wet" condition, where the surface was equilibrated under steam at 100°C for 10 minutes before measuring the CA. The CA was recorded after 2 minutes under "dry" conditions and after 10 seconds under "wet" conditions. Interestingly, the CA values significantly varied based on the conditions, attributed to changes in the surface morphology of cotton due to thermal stimuli.

The cotton surface modified by poly(HEMA-*r*-EGDMA) exhibited reversible wettability behavior, responding to external stimuli. This wettability-switching phenomenon was reproducible, demonstrating a clear alteration in surface properties (Figure 3), indicative of the functionality's repeatability. The observed phenomena are attributed to the hydroxyl groups of poly(HEMA) on the modified cotton surface forming hydrogen bonds under "dry" conditions. Conversely, under "wet" conditions, these hydrogen bonds are disrupted by steam, resulting in a transition to a hydrophilic surface. The alternation in surface properties is believed to be governed by the balance between the hydrogen bonding among the hydroxyl groups of the HEMA units and the cross-linking density introduced by the EGDMA units.

This study illustrates that the photo-VASP techniques reported here offer straightforward methods for reversible wettability switching surfaces through two distinct approaches. The poly(FA-*b*-AA) grafted onto Si-wafers exhibited reversible wettability in response to external stimuli, although some defects were observed. The reversibility of the grafted linear polymer surfaces is limited by repeated application of stimuli, as the water contact angles progressively transition towards hydrophilic properties. It is clear that the poly(FA-*b*-AA) on the Si surface, covalently bonded to the substrate through the self-assembly monolayer technique, gradually deteriorates the chemical structure of the thin film under external stimuli. The current limitations of grafted poly(FA-*b*-AA) on Si-wafers include the need for continuous multiple reaction steps and the maintenance of surface structure. These could potentially be addressed by employing simultaneous photo-VASP of a bifunctional monomer on fabrics. From the second approach, the simultaneous photo-VASP technique applied to fabrics produced cross-linked poly(HEMA-*r*-EGDMA) on fabrics immobilized on the substrate, demonstrating the versatility and potential of photo-VASP techniques in surface modification applications.

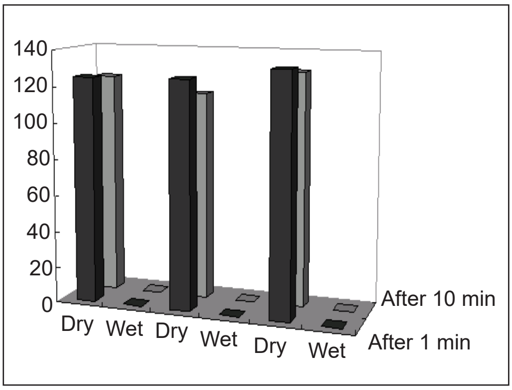

Figure 3. Effect of external stimuli on static contact angles of cotton surfaces modified by cross-linked poly(HEMA-*r*-EGDMA) layers

CONCLUSION

The products obtained demonstrated reversible wettability in response to external stimuli, underscoring the repeatability of this intelligent function. Two critical factors—the surface morphology and the chain transfer reaction to fabric surfaces under photo-irradiation—are essential for achieving distinct switching of reversible wettability properties, effectively overcoming damage from external stimuli.

The immobilization of the polymer layer on fabric through photo-irradiation proved highly reproducible and scalable. The resulting coatings were exceptionally robust, with the cross-linked poly(HEMA-*r*-EGDMA) surfaces maintaining their switching behavior even after being exposed to heat for 30 minutes at 110°C or steam for 10 minutes at 100°C. We believe this method endows surfaces/materials with unique properties suitable for fabric applications. Its significant advantages—solvent-free, allowing easy control of reaction parameters, maintaining constant monomer concentration, and requiring low energy consumption—offer an alternative approach for synthesizing various copolymer thin films.

These findings enable us to control and achieve numerous combinations using various monomers. The concepts introduced in this study are not confined to hydrogels alone but are applicable and should be extended to other categories of copolymers.

ACKNOWLEDGEMENT

This work was partly supported by Henkel KGaA, and the authors express their deep gratitude to Prof. Takeshi Endo and Prof. Haruo Nishida.

REFERENCES

Andou, Y., Nishida, H., & Endo, T. (2006). Designed surface construction by photo-induced vapor-phase assisted surface polymerization of vinyl monomers using immobilized free radical initiators. *Chemical Communications*, 5018–5020. https://doi.org/10.1039/b612018k

Andou, Y., Yasutake, M., Nishida, H., & Endo, T. (2007). Designed surface modification by photo-induced vapor phase assisted surface polymerization of vinyl monomers. *Journal of Photopolymer Science and Technology*, *20*(4), 523–528. https://doi.org/10.2494/photopolymer.20.523

Brotherton, E. E., Johnson, E. C., Smallridge, M. J., Hammond, D. B., Leggett, G. J., & Armes, S. P. (2023). Hydrophilic aldehyde-functional polymer brushes: Synthesis, characterization, and potential bioapplications. *Macromolecules, 56*(5), 2070–2080. https://doi.org/10.1021/acs.macromol.2c02237

Chan, K., & Gleason, K. K. (2005). Initiated chemical vapor deposition of linear and cross-linked poly (2-hydroxyethyl methacrylate) for use as thin-film hydrogels. *Langmuir*, *21*(19), 8930–8939. https://doi.org/10.1021/la051004q

Chenglong, G., Junliang, Z., Huan, Y., Yuansong, W., Yuheng, L., Renxiang, Z., Ziyuan, S., & Lichen, Y. (2023) Rational construction of protein-mimetic nano-switch systems based on secondary structure transitions of synthetic polypeptides. *Journal of the American Chemical Society, 145*(20), 11206-11214. https://doi.org/10.1021/jacs.3c01156

Fu, D., Weng, L. T., Du, B., Tsui, O. K. C., & Xu, B. (2002). Solventless polymerization at the gas–solid interface to form polymeric thin films. *Advanced Materials*, *14*(5), 339–343. https://doi.org/10.1002/1521-4095(20020304)14:5<339::AID-ADMA339>3.0.CO;2-Q

Gouget-Laemmel, A. C., Zidelmal, N., Soares, R. S. B., Barroca-Aubry, N., Dragoe, D., Costa, L., Lepoittevin, B., Salmi-Mani, H., Mellah, M., Henry-de-Villeneuve, C., Ozanam, F., Schulz, E., & Roger, P. (2023). Direct quantitative characterization of polymer brushes obtained by surface-initiated ATRP on silicon. *ACS Applied Polymer Materials, 5*(1), 517–528. https://doi.org/10.1021/acsapm.2c01234

Gu, H., Xu, C., Weng, L. T., & Xu, B. (2003). Solventless polymerization: Spatial migration of a catalyst to form polymeric thin films in microchannels. *Journal of the American Chemical Society*, *125*(31), 9256–9257. https://doi.org/10.1021/ja029954a

Guan, G., Wu, M., & Han, M. Y. (2020). Stimuli-Responsive hybridized nanostructures. *Advanced Functional Materials, 30*(2), Article 1903439. https://doi.org/10.1002/adfm.201903439

Gupta, M., Kapur, V., Pinkerton, N. M., & Gleason, K. K. (2008). Initiated Chemical Vapor Deposition (iCVD) of conformal polymeric nanocoatings for the surface modification of high-aspect-ratio pores. *Chemistry of Materials*, *20*(4), 1646–1651. https://doi.org/10.1021/cm702810j

Hester, J. F., Banerjee, P., & Mayes, A. M. (1999). Preparation of protein-resistant surfaces on poly (vinylidene fluoride) membranes via surface segregation. *Macromolecules*, *32*(5), 1643–1650. https://doi.org/10.1021/ma980707u

Higaki, Y., Kobayashi, M., Hirai, T., & Takahara, A. (2018). Direct polymer brush grafting to polymer fibers and films by surface-initiated *polymerization. Polymer Journal, 50*, 101–108. https://doi.org/10.1038/s41428-017-0010-1

Jung, D. H., Park, I. J., Choi, Y. K., Lee, S. B., Park, H. S., & Rühe, J. (2002). Perfluorinated polymer monolayers on porous silica for materials with super liquid repellent properties. *Langmuir*, *18*(16), 6133–6139. https://doi.org/10.1021/la025558u

Lau, K. K. S., & Gleason, K. K. (2006). Particle surface design using an all-dry encapsulation method. *Advanced Materials*, *18*(15), 1972–1977. https://doi.org/10.1002/adma.200600896

Lau, K. K. S., Bico, J., Teo, K. B. K., Chhowalla, M., Amaratunga, G. A. J., Milne, W. I., McKinley, G. H., & Gleason, K. K. (2003). Superhydrophobic carbon nanotube forests. *Nano Letters*, *3*(12), 1701–1705. https://doi.org/10.1021/nl034704t

Liang, L., Rieke, P. C., Liu, J., Fryxell, G. E., Young, J. S., Engelhard, M. H., & Alford, K. L. (2000). Surfaces with reversible hydrophilic/hydrophobic characteristics on cross-linked poly(*N*-isopropylacrylamide) hydrogels. *Langmuir*, *16*(21), 8016–8023. https://doi.org/10.1021/la0010929

Lin, Y. T., Fromel, M., Guo, Y., Guest, R., Choi, J., Li, Y. S., Kaya, H., Pester, C. W., & Kim, S. H. (2022). Elucidating interfacial chain conformation of superhydrophilic polymer brushes by vibrational sum frequency generation spectroscopy. *Langmuir, 38*(48), 14704–14711. https://doi.org/10.1021/acs.langmuir.1c02580

Maity, N., & Dawn, A. (2020). Conducting polymer grafting: Recent and key developments. *Polymers, 12*(3), Article 709. https://doi.org/10.3390/polym12030709

Mostafavi, A. H., Mishra, A. K., Gallucci, F., Kim, J. H., Ulbricht, M., Coclite, A. M., & Hosseini, S. S. (2023). Advances in surface modification and functionalization for tailoring the characteristics of thin films and membranes via chemical vapor deposition techniques. *Journal of Applied Polymer Science, 140*(15), Article e53720. https://doi.org/10.1002/app.53720

Nagase, K., Kobayashi, J., & Okano, T. (2009). Temperature-responsive intelligent interfaces for biomolecular separation and cell sheet engineering. *Journal of the Royal Society Interface, 6*(suppl_3), S293–S309. https://doi.org/10.1098/rsif.2008.0499.

Nishida, H., Yamashita, M., Andou, Y., Jeong, J. M., & Endo, T. (2005). Gas-Phase assisted surface polymerization behavior of *β*-propiolactone on inorganic and organic substrates and consequent composite production. *Macromolecular Materials and Engineering*, *290*(8), 848–856. https://doi.org/10.1002/mame.200500142

Ogiwara, Y., Kubota, H., & Murata, Y. (1974). Relationship between photo-Induced scission of cellulose chains and graft copolymerization. *Journal of Applied Polymer Science*, *18*(11), 3455–3462. https://doi.org/10.1002/app.1974.070181124

Onome E., Solomon, A., Ephraim, A., & Ahmed, O. O. (2023) Insights on smart and stimuli-responsive hydrogel membranes for oil/water separation: A sustainable tool for oily pollutant remediation. *Materials Today Communications 35*, Article 106063. https://doi.org/10.1016/j.mtcomm.2023.106063

Thang, N. H., Chien, T. B., & Cuong, D. X. (2023). Polymer-based hydrogels applied in drug delivery: An overview. *Gels, 9*(7), Article 523. https://doi.org/10.3390/gels9070523

Wang, S., Wang, Z., Li, J., Li, L., & Hu, W. (2020). Surface-grafting polymers: from chemistry to organic electronics. *Materials Chemistry Frontiers, 4*(3), 692-714. https://doi.org/10.1039/C9QM00450E

Wang, Y., & Chang, Y. C. (2003). Patterning of polypeptide thin films by the combination of surface-initiated vapor-deposition polymerization and photolithography. *Advanced Materials*, *15*(4), 290–293. https://doi.org/10.1002/adma.200390069

Xi, H., Teng, W., Faqi, L., & Xiang, M. (2023) Surface modifications of biomaterials in different applied fields. *RSC Advances*, *13*(30), 20495-20511. https://doi.org/10.1039/D3RA02248J.

Yakushiji, T., Sakai, K., Kikuchi, A., Aoyagi, T., Sakurai, Y., & Okano, T. (1998). Graft architectural effects on thermoresponsive wettability changes of poly (*N*-isopropylacrylamide)-modified surfaces. *Langmuir*, *14*(16), 4657–4662. https://doi.org/10.1021/la980090+

Yasutake, M., Hiki, S., Andou, Y., Nishida, H., & Endo, T. (2003). Physically controlled radical polymerization of vaporized vinyl monomers on surfaces. synthesis of block copolymers of methyl methacrylate and styrene with a conventional free radical initiator. *Macromolecules*, *36*(16), 5974–5981. https://doi.org/10.1021/ma021795s

Pertanika J. Sci. & Technol. 33 (S2): 13 - 25 (2025)

SCIENCE & TECHNOLOGY

Journal homepage: http://www.pertanika.upm.edu.my/

Numerical Analysis of the Load-carrying Capacity of Built-up Columns with Damaged or Missing Lacing Bars

Toshikazu Takai[1]*, Taiyo Furuichi[2], Takao Miyoshi[3], Kaname Iwatsubo[4], Kazuya Tamada[5] and Kenta Morimoto[6]

[1]Department of Civil and Architectural Engineering, Faculty of Engineering, Kyushu Institute of Technology, Kitakyushu 804-8550, Japan
[2]Former student, Department of Civil Engineering and Architecture, School of Engineering, Kyushu Institute of Technology, Kitakyushu 804-8550, Japan
[3]Department of Civil Engineering, National Institute of Technology (KOSEN), Akashi College, Akashi 674-8501, Japan
[4]Production System Engineering Course, National Institute of Technology (KOSEN), Kumamoto College, Yatsushiro 866-8501, Japan
[5]Department of Civil Engineering and Architecture, National Institute of Technology (KOSEN), Maizuru College, Maizuru 625-8511, Japan
[6]Department of Engineering, Graduate School of Engineering, Kyushu Institute of Technology, Kitakyushu 804-8550, Japan

ABSTRACT

Built-up columns with lacing bars are commonly used in old bridges. Typically, these columns consist of shaped steel members connected by riveted lacing bars. This design held the advantage of reducing steel usage, thereby lowering costs. However, these techniques have become outdated. Nevertheless, structures constructed using these methods persist today. Over time, some of these columns have experienced component loss because of ageing, damage, or corrosion. This study uses finite element analysis to determine the load-carrying capacity of built-up columns with lacing bars subjected to compressive forces. The results indicate that the loss of some lacing bars results in a 2% reduction in load-carrying capacity, while the loss of both lacing bars and rivets leads to a 5% reduction. Though the reduction may appear marginal, the presence or absence of lacing bars and rivets becomes a significant consideration in estimating the remaining load-carrying capacity. The results of this study have implications with respect to the ongoing use and maintenance of built-up columns with missing components, which has emerged as a critical concern.

Keywords: Buckling, built-up column, finite element analysis, lacing bar, riveted connection

ARTICLE INFO

Article history:
Received: 13 February 2024
Accepted: 18 October 2024
Published: 25 February 2025

DOI: https://doi.org/10.47836/pjst.33.S2.02

E-mail addresses:
takai@civil.kyutech.ac.jp (Toshikazu Takai)
furuichi.taiyo521@mail.kyutech.jp (Taiyo Furuichi)
miyoshi@akashi.ac.jp (Takao Miyoshi)
iwatsubo@kumamoto-nct.ac.jp (Kaname Iwatsubo)
tamada@maizuru-ct.ac.jp (Kazuya Tamada)
morimoto.kenta110@mail.kyutech.jp (Kenta Morimoto)
* Corresponding author

ISSN: 0128-7680
e-ISSN: 2231-8526

INTRODUCTION

Built-up columns with lacing bars are commonly used in old bridges, as shown in Figure 1. These columns typically consist of channel-shaped steel members and lacing bars. The lacing bars are connected to the channel-shaped steel with a rivet, reducing the required steel and construction costs. Miyoshi (2021a) investigated previous Japanese specifications for highway bridges. Regulations on built-up columns were deleted from the Japanese highway bridge specifications and revised in 1980 (JRA, 1980). Similarly, regulations on riveted connections were deleted from the Japanese specifications for highway bridges and were revised in 1990 (JRA, 1990). These techniques are currently old; however, structures that utilise these techniques still exist. As shown in Figure 1, some columns lose their components because of ageing, damage, or corrosion. The load-carrying capacity of a column that has lost some components is important for maintaining and continuing to use these structures. Therefore, the load-carrying capacity of the columns must be determined.

Previous studies investigated the mechanical behaviours of a plate with a corroded surface, such as buckling load (Sadovsky & Drdacky, 2001) and ultimate shear strength (Paik et al., 2004). Beaulieu et al. (2010) experimentally studied the compressive strength of corroded steel angles. The capacity of the angle was compared with design codes. Hisazumi et al. (2018) investigated the buckling load of corroded steel channels and angle members by considering the local buckling behaviour. Thus, the mechanical behaviour of corroded steel members has been investigated in some studies. A built-up column contains several components. The interaction of the components exhibits mechanical behaviour, thereby impacting the corrosion complex. However, studies on the mechanical behaviour of corroded built-up columns are lacking.

Although the column missing lacing bars or rivets are present, the load-carrying capacity of such column is unknown. The authors have previously conducted studies

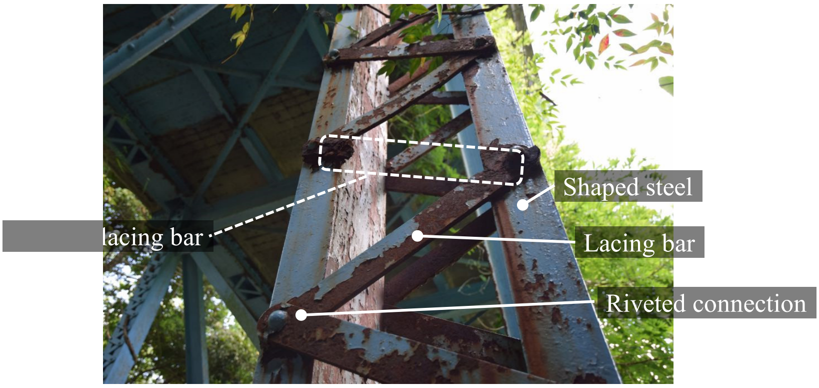

Figure 1. A built-up column. The column appears old and is missing a lacing bar

to determine the load-carrying capacity of built-up columns with lacing bars, both experimentally (Miyoshi et al., 2021b, 2021c, 2022; Nakakita et al., 2021) and numerically (Iwatsubo et al., 2020a, 2020b; Kojima & Takai, 2021; Miyoshi et al., 2022; Nakakita et al., 2022). However, the numerical evaluation was conducted by modelling the riveted connections (between the shaped steel and lacing bars) using simple models with limitations. Therefore, the detailed influence of missing rivets and lacing bars, considering the behaviour of the area around the rivet holes, on a column's load-carrying capacity was not evaluated. This study investigated the necessity of modelling riveted connections using finite element analysis. Moreover, the load-carrying capacity of columns, with lacing bars and rivets missing, was investigated.

NUMERICAL MODELLING OF THE AREA AROUND RIVETED CONNECTIONS

Methods

The load-carrying capacity analysis of the channel-shaped steel of a built-up column examined the modelling in the area around the riveted connections. The numerical analysis was conducted using Abaqus/Standard 6.13. Figure 2 depicts an outline of the numerical model. Shaped steel was integrated as a component of the built-up column. The thicknesses of the flange and web plates were 3.5 mm. A linearly reduced integration 8-node solid element was used. The length of each element was approximately 1.2 mm. The plate was divided into three elements along the thickness direction. The initial deflection and residual stress specifications illustrated in Figures 3 and 4 were applied to the model as initial imperfections. The shape of the initial deflection was sinusoidal, with an amplitude equal to

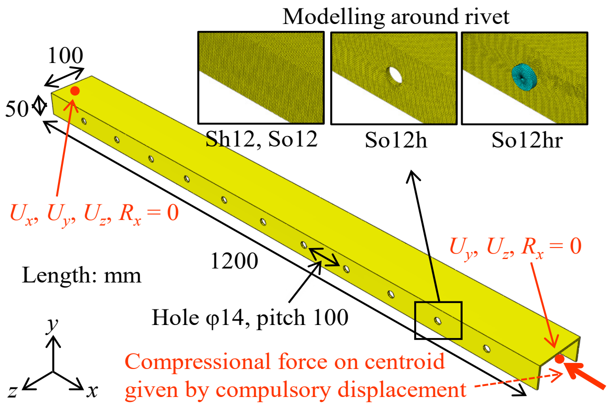

Figure 2. Outline of the numerical model. The centroid on one side of the column is fixed; the other is set to compulsory displacement to provide compressional force

the maximum fabrication tolerance of the steel members of highway bridges (JRA, 1990). The direction of initial deflection was determined using an eigenvalue buckling analysis conducted in advance. The residual stress was set considering the stress equilibrium in the cross-section (Iwatsubo et al., 2020a, 2020b). A compression load was applied to the column by the compulsory displacement of the centroid at the end of the column. The stress-strain relationship values are summarised in Table 1. These values assume the steel grade of SM490Y (JIS G 3106, 2020). The 200 000 N/mm^2 and 0.3 values were used for Young's modulus and Poisson's ratio, respectively. The material properties of the channel steel and the rivets were identical.

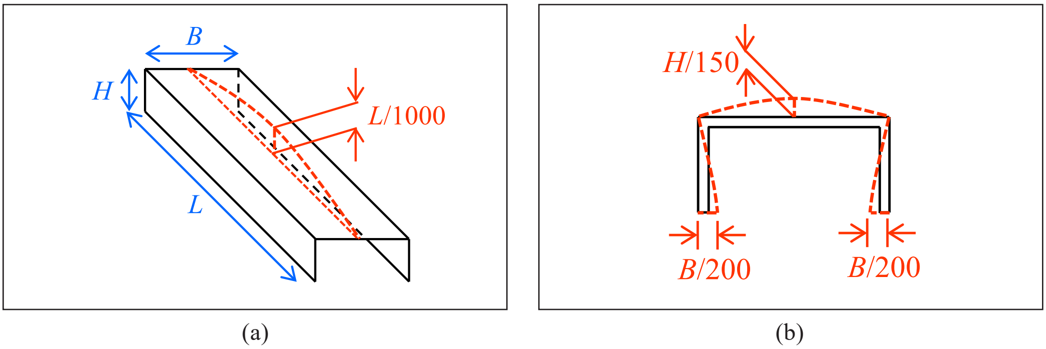

Figure 3. Initial deflection specifications. The shape of the deflection is sinusoidal, with an amplitude equal to the maximum fabrication tolerance of the steel members of highway bridges: (a) Whole length; and (b) Cross-section

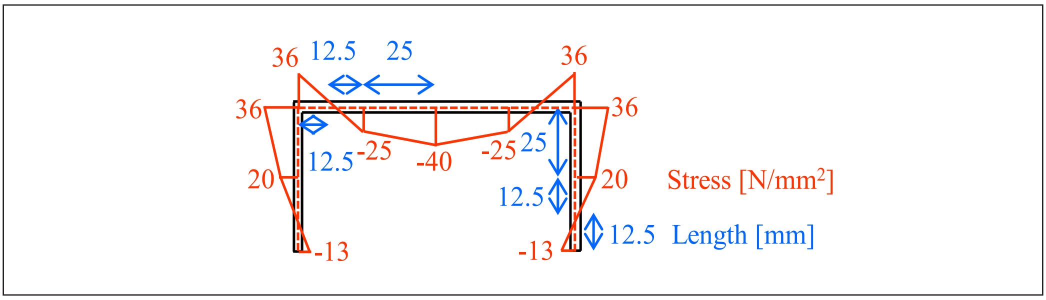

Figure 4. Residual stress specifications. The residual stress is set considering the stress equilibrium in the cross-section

Table 1
Stress-strain relationship values

	Nominal stress [N/mm^2]	Nominal strain	True stress [N/mm^2]	True strain
Yield point	355	0.0018	356	0.0018
Tensile strength	551	0.0996	606	0.0950

Investigated Cases

The analysed cases are summarised in Table 2. The shell and solid element cases were compared under identical conditions. These cases differed only in terms of element type. In comparison, the application of solid elements to the load-carrying capacity analysis of a compressional column was investigated; however, for a buckling analysis, a compressional column is typically modelled using shell elements. Solid elements are beneficial in stereographically modelling the details of riveted connections to replicate the contact between rivets and holes. The findings from this comparative investigation corroborate the application of the solid element model to the numerical analysis of load-carrying capacity involving buckling behaviour. Our study involved two distinct column lengths: (1) a 300 mm column referred to as a "stub column" and (2) a 1200 mm column designated as a "long column." The stub column exhibited a buckling load that exceeded the compressional yield load, determined by multiplying the yield point and cross-sectional area. In contrast, the long column did not surpass the compressional yield load in terms of its buckling load. A column with rivet holes and rivets was analysed for the solid element cases to determine the necessity of accurately modelling the riveted connections.

Table 2
Specifications of the investigated cases

Case name	Element type	Length [mm]	Rivet holes	Rivets
Sh3	Shell	300	Not modelled	Not modelled
So3	Solid	300	Not modelled	Not modelled
So3h	Solid	300	Modelled	Not modelled
So3hr	Solid	300	Modelled	Modelled
Sh12	Shell	1200	Not modelled	Not modelled
So12	Solid	1200	Not modelled	Not modelled
So12h	Solid	1200	Modelled	Not modelled
So12hr	Solid	1200	Modelled	Modelled

Results

Table 3 summarises the maximum load and corresponding displacement values for each case. The reduction value for each case is the percentage difference between the maximum load and that of the shell element case of the same length. The difference between the shell element cases Sh3 and Sh12 and the solid element cases So3 and So12 was less than 1%. However, the maximum load in the cases with rivet holes, So3h and So12h, was reduced by more than 15%. The reduction was significantly less for the cases with holes and rivets, that is, So3hr and So12hr. These values were approximately 3% lower than those of Sh3 or Sh12.

Figure 5 shows the obtained load-displacement curves. The vertical axis represents the dimensionless value *P/Py*, the ratio of the compressed load to the design yield load. The design yield load is obtained by multiplying the yield point by the cross-sectional area without rivet holes. The horizontal axis represents the dimensionless value *U/Uy*, the ratio of the displacement to the yield displacement. The yield displacement was obtained by multiplying the yield strain by the column length. The displacement was measured at the centroid-applied compulsory displacement at the end of the column. First, the load increased linearly in each case. The load increased linearly for the 300 mm length case, then gradually reached the maximum load. In contrast, for the 1200 mm cases, the load increased linearly and suddenly decreased.

Figure 6 shows the von Mises stress distribution at the maximum load. The distributions of shell element cases Sh3 and Sh12 were the same as those of solid element cases So3 and So12, respectively. For cases such as So3h and So12h, where rivet holes were used, stress concentration occurred around the rivet holes. The stress was lower than that in the cases So3 and So12 (without holes). In contrast, for cases So3hr and So12hr (holes with rivets), the stress distribution was approximately equal to So3 and So12, respectively, despite the stress in the rivets being significantly smaller.

Table 3
Maximum load and displacement results

Case name	P_{max} [kN]	Reduction* [%]	U_{Pmax} [mm]
Sh3	235	0.0	0.6
So3	234	-0.4	0.6
So3h	179	-23.8	0.7
So3hr	227	-3.4	0.6
Sh12	148	0.0	1.4
So12	147	-0.7	1.4
So12h	122	-17.6	1.2
So12hr	144	-2.7	1.3

*Reduction is the percentage difference between the maximum load and the shell element case of the same length

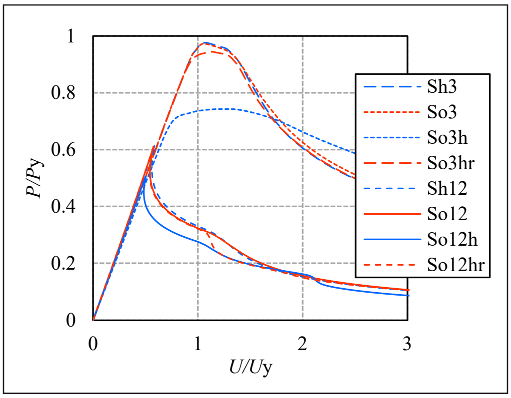

Figure 5. Load-displacement curves. The curves of the cases Sh3, So3, and So3hr are almost the same. While the cases Sh12, So12, and So12hr have almost the same curves. However, the maximum loads of the cases So3h and So12h are lower than those of the others

Discussion

Comparing Sh3 and So3, or Sh12 and So12, the obtained maximum load and load-displacement curves in Figure 5 were approximately equal. Similarly, the overall stress distributions were approximately equal, as shown in Figure 6. In previous studies, the numerical analysis of compressed columns, including buckling behaviour, has typically

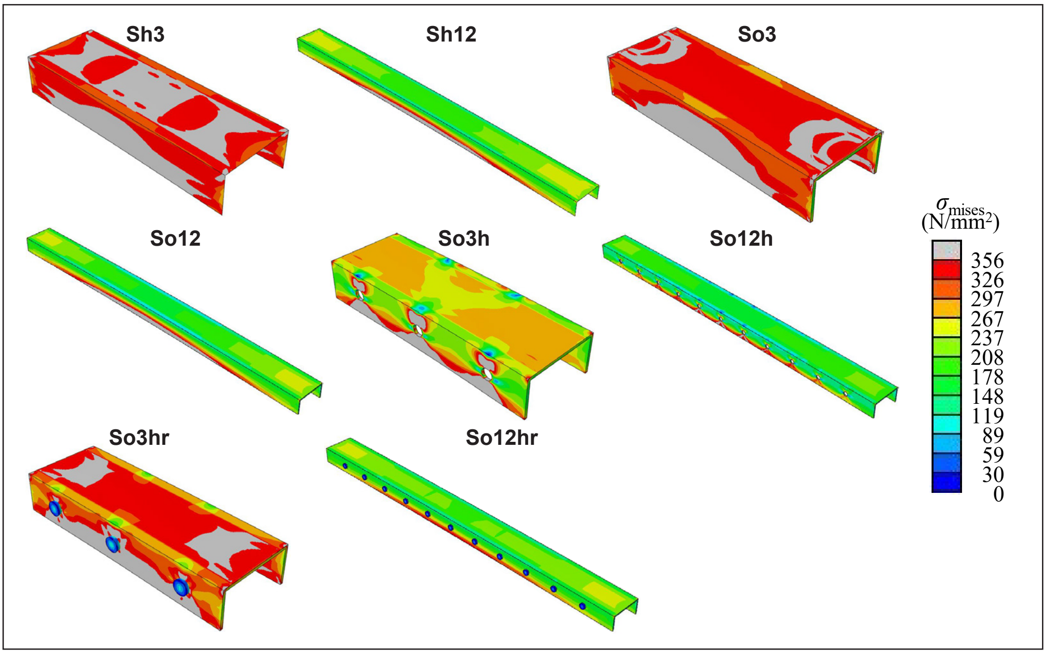

Figure 6. von Mises stress distribution at maximum load. The distributions of the cases Sh3, So3, and So3hr are almost the same. While the cases Sh12, So12, and So12hr have almost the same distributions. Stress concentration occurs around the rivet holes in cases So3h and So12h (with holes). In these cases, the stress is lower than that in So3 and So12 (without holes)

been conducted using shell elements. However, this result indicates that numerical analysis using solid elements yields results equal to shell elements. Hence, solid elements can be adapted to finite element analysis to evaluate a compressed column. Conveniently, applying solid elements enables us to replicate the contact between rivets and holes and evaluate the detailed behaviour of the riveted connection. Based on this result, a further evaluation of the detailed behaviour of the area around the riveted holes was conducted using solid element models.

As shown in Figure 5, the maximum loads of cases So3h and So12h (with rivet holes modelled) were lower than those of So3 and So12 (without holes modelled), respectively, because of the reduction in the net cross-sectional area owing to the rivet holes. The occasion of stress concentration by the holes, as shown in Figure 6, reduced the maximum load. However, by filling the hole with a rivet, that is, in cases So3hr and So12hr, the reduction in the maximum load was minimised because the contact between the rivet axis and the hole transmitted compressional forces. The stress concentration around the rivet holes decreased from So3h to So12h. The maximum loads of So3hr and So12hr were approximately equal or marginally less than those of So3 and So12, respectively. This result suggests that despite the maximum load being equal for both cases, modelling rivets and rivet holes is necessary to evaluate the detailed behaviour, including the area around the rivet connection. Because the load-carrying capacity of the columns with missing lacing bars and rivets was unknown, the parametric study in the next section was performed.

COMPRESSIONAL BEHAVIOUR OF BUILT-UP COLUMN WITH MISSING LACING BARS

Methods

The built-up column was modelled based on previous studies (Iwatsubo et al., 2020a, 2020b). The column comprised two channel-shaped steel members and 24 lacing bars. The lacing bars were tightened using rivets. Figure 7 shows an outline of the numerical model. The column length was 900 mm. The channel steel had flange plates 50 mm wide and a web plate 100 mm wide. The thickness of the plate was 9 mm. The dimensions of the lacing bars were 170×20×4 mm. The diameter of the rivet holes was 14 mm. The hole pitch was 115.5 mm. The friction coefficient was 0.1. The model included initial imperfections: the initial deflection in Figure 8 and the residual stress in Figure 4. The direction of the initial deflection was determined using eigenvalue buckling analysis. The lengths of the

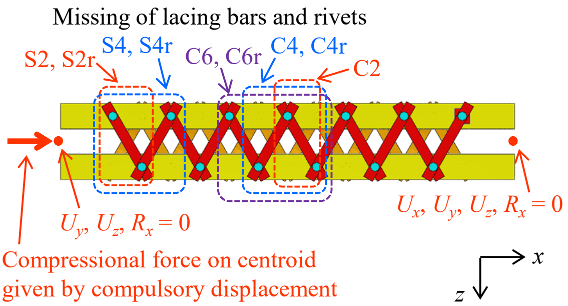

Figure 7. Outline of numerical model. The S-series cases are missing lacing bars near the sides of the column, whereas those of the C-series are missing lacing bars at the centre of the column

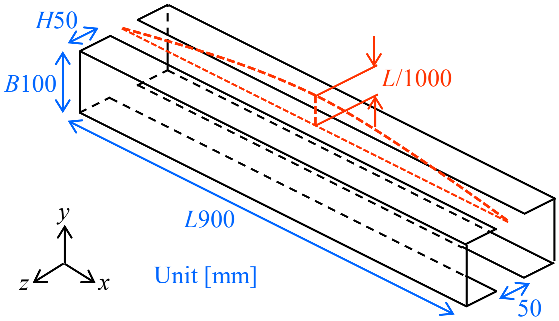

Figure 8. Initial deflection specifications. The deflection shape is sinusoidal, with an amplitude equal to the maximum fabrication tolerance of the steel members of highway bridges

solid elements were approximately 1.5 mm. The material properties are the same as those described in the previous section.

Investigated Cases

Table 4 summarises the analysed cases. N0 represents the normal case without any loss of lacing bars or rivets. The S-series cases lost lacing bars near the side ends of the column. The C-series cases lost lacing bars at the centre of the column. The cases with names including "r" lost not only lacing bars but also rivets that fastened the lost lacing bars. In both cases, the influence of the position of the lacing bars was compared. The lost lacing bars ranged from 2–4 for the C-series cases and 2–6 for the S-series cases. The effects of the number of lacing bars lost were compared. It was assumed that the rivet was present for the cases in which rivets existed, even when the lacing bars were missing. It was assumed that the lacing bars and rivets were missing for the cases in which the rivets were missing, owing to serious corrosion.

Table 4
Investigated cases

Case name	Position of lost lacing bars	Number of lost lacing bars	Loss of rivets
N0	n/a	0	Exist
S2	Side	2	Exist
S2r	Side	2	Lost
S4	Side	4	Exist
S4r	Side	4	Lost
C2	Centre	2	Exist
C4	Centre	4	Exist
C4r	Centre	4	Lost
C6	Centre	6	Exist
C6r	Centre	6	Lost

Results

Figure 9 shows the obtained load-displacement curves. The load increased linearly by 0.8Py. The load-displacement curves were approximately identical, even for the case with missing lacing bars and rivets, except around the peak of the curves. The maximum load for each case and the corresponding reduction in loads from the normal case N0 are listed in Table 5. Figure 10 compares the maximum load and reduction, as listed in Table 5. The loss of 2–6 lacing bars reduced the maximum load by less than 2%. By contrast, the loss of the lacing bars and rivets reduced the maximum load by 5%.

Figure 11 shows the von Mises stress distribution at the maximum load. The grey range represents the yielded area. As shown in cases S4r and C6, the stress on the flange around

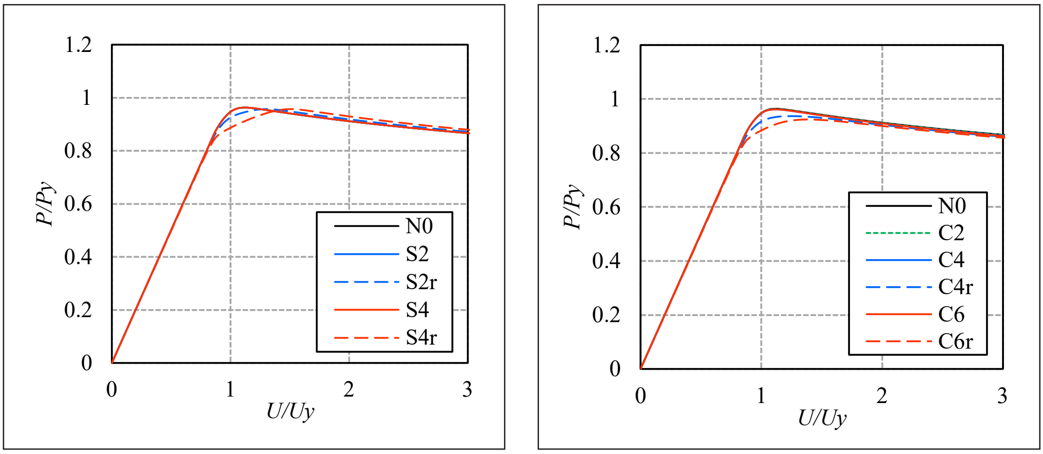

(a)

(b)

Figure 9. Load and displacement curves for the test cases. The curves of all the cases are almost the same, even when lacing bars and rivets are missing, except around the peaks: (a) Side loss cases: and (b) Centre loss cases

Table 5
Maximum load and the reduction

Case name	Maximum load [kN]	Reduction* [%]
N0	1138	0
S2	1123	-1.3
S2r	1117	-1.8
S4	1123	-1.3
S4r	1117	-1.8
C2	1122	-1.4
C4	1121	-1.5
C4r	1093	-4.0
C6	1121	-1.5
C6r	1078	-5.3

*Reduction is the percentage difference between the maximum load and the normal case N0

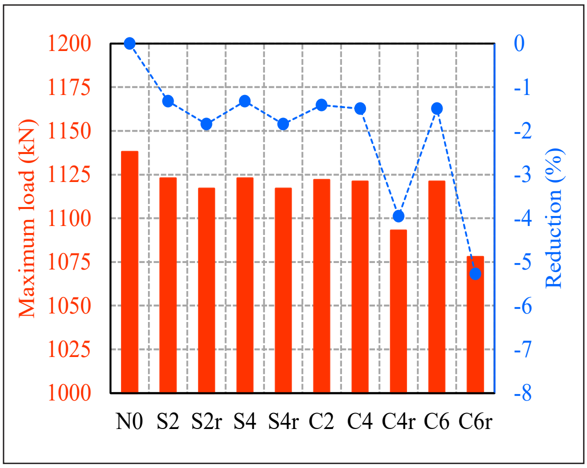

Figure 10. Maximum load for each test case. The missing of 2–6 lacing bars decreases the maximum load by less than 2%, whereas that of the lacing bars and rivets decreases the maximum load by 5%

the lost lacing bar was slightly reduced. However, for C6r, which had missing lacing bars and rivets, the stress on the flange around the lost rivet holes was significantly reduced.

Discussion

As shown in Figure 9, the loss of lacing bars or rivets did not affect the compression behaviour in the elastic range. This result suggests that the loss of lacing bars and rivets in

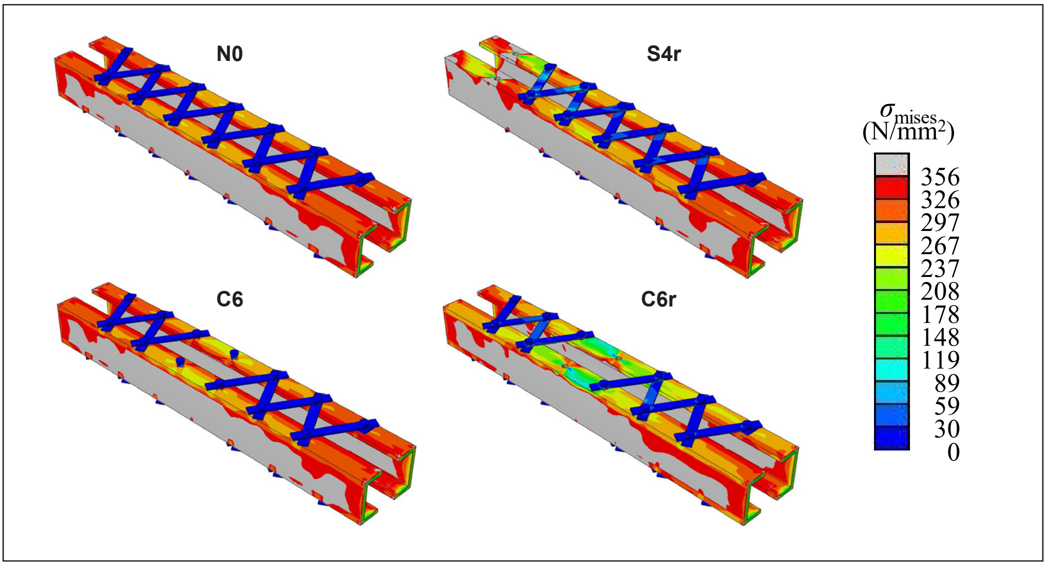

Figure 11. von Mises stress distribution at maximum load. In the cases S4r and C6, the stress on the flange around the lost lacing bar is slightly decreased. However, for C6r, which has missing lacing bars and rivets, the stress on the flange around the lost rivet holes is significantly decreased

the range investigated in this study does not affect the mechanical behaviour of the column in the service limit state. The effect of the loss of lacing bars and rivets appeared around the peak of the load beyond the elastic range, as shown in Figure 9. Therefore, the loss of the lacing bars and rivets affected the load-carrying capacity of the column. As shown in Figure 10, the loss of rivets reduced the maximum load by 5%, and the loss of only lacing bars limited the reduction of the maximum load to 2%. This is because the loss of the rivets reduced the net cross-sectional area and the compressional load transfer due to the contact between the rivet axis and hole. Although the loss of a rivet causes stress concentration around the empty rivet holes and reduces the load-carrying capacity, the bearing prevents stress concentration and reduces capacity. Hence, the loss of the rivets is an important concern when estimating the residual load-carrying capacity of built-up columns. In this study, thickness reduction due to corrosion of steel shapes was not evaluated. Because the reduction in plate thickness reduces the load-carrying capacity, the load-carrying capacity in that case should be evaluated. Because the combination of the reduction in thickness and the lacing bars causes a significant reduction in load-carrying capacity, it is necessary to evaluate that in the case where the plate thickness is reduced.

CONCLUSION

This study investigated the load-carrying capacity of built-up columns in scenarios where lacing bars and rivets were absent. Employing finite element analysis, we also examined the critical aspect of modelling riveted connections. The ensuing results and conclusions can be summarised as follows:

The assessment of the compressional behaviour of built-up columns, achieved through finite element analysis focusing on solid elements, represents a significant departure from prior studies that predominantly relied on shell elements. The results, encompassing maximum load values, load-displacement curves, and stress distributions, demonstrated an impressive congruence between models employing solid and shell elements. This underscores the adaptability of solid elements for finite element analysis, particularly in the context of column compression, and their efficacy in facilitating intricate modelling of riveted connections.

The presence of rivet holes has an adverse effect on the load-carrying capacity of columns in compression. This is primarily attributed to the reduction in the net cross-sectional area, leading to heightened stress concentrations around the perforations. Conversely, introducing rivets to fill these holes leads to almost completely recovering the maximum load. This revival is attributed to the effective transmission of compressional forces through contact between the rivet axis and the hole. Consequently, it becomes evident that modelling the rivet and the hole is necessary for determining the behaviour of the area around the rivet connection.

The loss of 2–6 lacing bars resulted in a minimal reduction of the maximum load, typically around 2% or less. However, the absence of lacing bars combined with the presence of filled rivets caused a more substantial reduction in the maximum load, peaking at 5%. This phenomenon can be ascribed to the absence of rivets, which not only diminishes the net cross-sectional area but also disrupts the transfer of compressive loads through the loss of contact between the rivet axis and the hole, thus promoting stress concentration around the hole. Consequently, the presence or absence of rivets is a pivotal consideration in estimating the residual load-carrying capacity of built-up columns.

ACKNOWLEDGEMENT

This work was supported by JSPS KAKENHI Grant Number JP19K04587.

REFERENCES

Beaulieu, L. V., Legeron, F., & Langlois, S. (2010). Compression strength of corroded steel angle members. *Journal of Constructional Steel Research*, *66*, 1366–1373. https://doi.org/10.1016/j.jcsr.2010.05.006

Hisazumi, K., Kanno, R., & Tominaga, T. (2018). Local buckling behavior and strength evaluation of corroded steel shapes. *Steel Construction Engineering*, *25*(99), 67–76. https://doi.org/10.11273/jssc.25.99_67

Iwatsubo, K., Oda, N., Miyoshi, T., Takai, T., & Tamada, K. (2020a, September 7-9). *The design and the ultimate strength behavior of built-up columns subjecting the compressive load*. [Paper presentation]. Proceedings of Japan Society of Civil Engineers Annual Meeting, Tokyo, Japan

Iwatsubo, K., Oda, N., Miyoshi, T., Takai, T. & Tamada, K. (2020b). The strength behavior of the built-up columns used the channel members. *Proceedings of Constructional Steel, 28,* 102–108.

JIS G 3106 (2020). *Rolled steels for welded structure*. Japanese Industrial Standards. chrome-extension://efaidnbmnnnibpcajpcglclefindmkaj/https://webdesk.jsa.or.jp/preview/pre_jis_g_03106_000_000_2020_e_ed10_ch.pdf

JRA (1980). *Specifications for Highway Bridges*. Japan Road Association.

JRA (1990). *Specifications for Highway Bridges*. Japan Road Association.

Kojima, Y., Takai, T. (2021). Fundamental investigation on buckling eigen value of built-up column considering initial imperfection. *Japan Society of Civil Engineers, I-026*, 51–52.

Miyoshi, T. (2021a). Investigation on strength provisions of built-up column in design standards for Japanese highway bridges. *Memoirs of National Institute of Technology, 63*, 1–8.

Miyoshi, T., Iwatsubo, K., Takai, T. & Tamada, K. (2021b, September 6-10). *Material properties of a steel truss bridge built-up member passing 115 years since the completion*. [Paper presentation]. Proceedings of Japan Society of Civil Engineers Annual Meeting, Tokyo, Japan

Miyoshi, T., Iwatsubo, K., Takai, T. & Tamada, K. (2021c). Material properties of a steel bridge built-up member passing 115 years since the completion. *Proceedings of Constructional Steel*. *29*, 48–57.

Miyoshi, T., Nakakita, T., Iwatsubo, K., Takai, T. & Tamada, K. (2022). Compression strength of aged built-up column with vanished lacing bars. In A. Zingoni (Ed.) *Proceedings of the 8th International Conference on Structural Engineering, Mechanics and Computation* (pp. 950–955). CRC Press.

Nakakita, T., Miyoshi, T., Iwatsubo, K., Takai, T., Satake, R. & Tamada, K. (2021, September 6-10). *Residual stress distribution of a steel truss bridge built-up member passing 115 years since the completion*. [Paper presentation]. Proceedings of Japan Society of Civil Engineers Annual Meeting, Tokyo, Japan.

Nakakita, T., Miyoshi, T., Iwatsubo, K., Takai, T., & Tamada K. (2022). Investigation on residual stress of an aged channel-shaped steel and compression strength of a built-up column with disappeared lacing bars. *Journal of Structural Engineering A*, *68A,* 112–122. https://doi.org/10.11532/structcivil.68A.112

Paik, J. K., Lee, J. M., & Ko, M. J. (2004). Ultimate shear strength of plate elements with pit corrosion wastage. *Thin-Walled Structures*, *42*(8), 1161–1176. https://doi.org/10.1016/j.tws.2004.03.024

Sadovsky, Z., & Drdacky, M. (2001). Buckling of plate strip subjected to localised corrosion—A stochastic model. *Thin-Walled Structures*, *39*(3), 247–259. https://doi.org/10.1016/S0263-8231(00)00060-4

Pertanika J. Sci. & Technol. 33 (S2): 27 - 51 (2025)

SCIENCE & TECHNOLOGY

Journal homepage: http://www.pertanika.upm.edu.my/

Study on Sharing Electricity using Photovoltaic Panels and Storage Batteries in Housing Complexes

Hitomi Nakagama[1] and Wanghee Cho[2]*

[1]Graduate school, Department of Civil and Architectural Engineering, Kyushu Institute of Technology, 1-1 Sensuicho, Tobataku, Kitakyushu, 804-8550, Japan
[2]Department of Civil and Architectural Engineering, Kyushu Institute of Technology, 1-1 Sensuicho, Tobataku, Kitakyushu, 804-8550, Japan

ABSTRACT

After the Great East Japan Earthquake, the household sector of public welfare is promoting the introduction of distributed energy systems by diversifying energy sources and applying local energy use as one of the energy supply measures in case of a disaster. This study introduced an energy-sharing system in the housing complexes to examine whether each house with different family composition and life patterns (i.e., different energy use patterns) could use energy more efficiently. The target energy in the housing complexes was set to electricity, which was generated by photovoltaic panels and stored in storage batteries. The strategy for stable electricity supply and profit generation was as follows: (1) electricity generated by photovoltaic panels is consumed first in the housing complexes; (2) the remaining electricity is stored in a large-capacity storage battery for the operation of the cooling and heating system; (3) afterward, electricity is sold directly to nearby housing complexes at a lower price than the supply price of electricity companies and at a higher price than when sold to electricity companies. The calculation results show that the profit from the sale of surplus electricity and the reduction rate of CO_2 emissions were evaluated. The annual electricity purchase was 87 MWh, which decreased by 52% due to the introduction of the electricity-sharing system. Annual electricity sales were 433 MWh. The annual profit from selling surplus electricity directly to nearby houses was 1.14 times higher than selling to electricity companies. The CO_2 emission reduction rate was 56.2%.

Keywords: Economic evaluation, electricity, electricity sharing system, environmental evaluation, photovoltaic

INTRODUCTION

In Japan, one-third of total CO_2 emissions come from construction-related fields. In addition, the largest share of CO_2 emissions

ARTICLE INFO

Article history:
Received: 13 February 2023
Accepted: 18 October 2024
Published: 25 February 2025

DOI: https://doi.org/10.47836/pjst.33.S2.03

E-mail addresses:
nakagama.hitomi983@mail.kyutech.jp (Hitomi Nakagama)
chowh@civil.kyutech.ac.jp (Wanghee Cho)
*Corresponding author

ISSN: 0128-7680
e-ISSN: 2231-8526

in the construction-related sector is due to the energy used in operating the house, which accounts for approximately 40% (Ministry of Land, Infrastructure Japan, 2012). Figure 1 shows a breakdown of house energy sources (Ministry of Economy, Trade and Industry Japan, 2020).

Electricity accounts for more than half (51%) of the energy sources used in houses. It is necessary to consider how to effectively use and reduce electricity, as reducing it in the housing sector can lead to reducing CO_2 emissions in construction-related sectors.

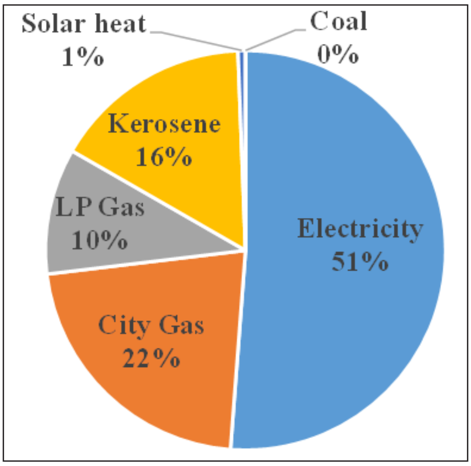

Figure 1. Breakdown of energy sources used in houses in Japan. Electricity accounts for more than half of the energy sources used

Meanwhile, in Korea, Concerns about nuclear accidents are growing due to the wake of the Great East Japan Earthquake in 2011 and a number of recent earthquakes around nuclear power plants. The announcement of the 8th Basic Plan for Electricity Supply and Demand in 2018 accelerates the phase-out of nuclear power and the transition to renewable energy (Nam, 2020). According to statistics from Korea Power Exchange, about 13% of the capacity of domestic electricity generation facilities is renewable energy-related facilities, including photovoltaic panels, of which photovoltaic power generation accounts for about 67% (Korea Power Exchange, 2019).

Investigation into smart city development began in the early 2000s, and the number of projects steadily increases every year. In 2018, the government set smart city development as one of the national development strategies; in 2018, 78 development projects were in progress (Lee, 2019). The key to energy in a smart city is renewable energy and transitioning to a low-carbon society. Renewable energy is produced, stored, distributed, and consumed in the smart grid (Lim et al., 2019). Most of the renewable energy used in smart cities is solar power generation. It is necessary to review technologies and strategies for efficient storage and distribution as well as the production of electricity through photovoltaic generation.

Daily Electrical Energy Balance in a House

Laws on energy conservation have recently been reorganized to strengthen insulation and airtightness performance as part of efforts to reduce CO_2 emissions in construction-related fields. In addition, the use of natural energy is being actively prospected. In particular, research in the housing sector is being conducted on developing energy-saving housing. The number of photovoltaic power generation facilities installed in houses has increased substantially, and according to data from the Japan Photovoltaic Energy Association, the installation rate of photovoltaic power generation facilities in houses rose to 9% as of 2019, with an increase of 0.7% from 8.3% in the previous year 2018 (Solar Power Association Japan, 2020). The number of installations is expected to continue to increase.

This study examines the livelihood of efficient electric energy by considering the balance between electricity consumption and electricity generation in houses with photovoltaic panels. Figure 2 shows a conceptual diagram of the change in a house's daily electricity consumption (Iwata et al., 2012). Figure 3 is a conceptual diagram showing electric energy generation in a house equipped with photovoltaic panels. As shown in Figure 2, energy consumption in the house is concentrated in the morning hours, when one prepares to go to work or school, and in the evening to night hours, when family members return home. Conversely, as shown in Figure 3, photovoltaic power generation gradually increases from sunrise in proportion to the horizontal total solar radiation and is the largest at noon. Afterward, it reduces again until sunset. In other words, a gap exists between when electricity consumption is large and when photovoltaic power generation is large; therefore, the per-hour supply and demand of electricity are not balanced. It is thus necessary to balance the supply and demand of electricity to efficiently use electricity generated by photovoltaic panels without waste and avoid unnecessary thermal power generation. To this end, a method of storing electricity generated during the day in a storage battery and using it in a time zone when electricity demand is high may be considered.

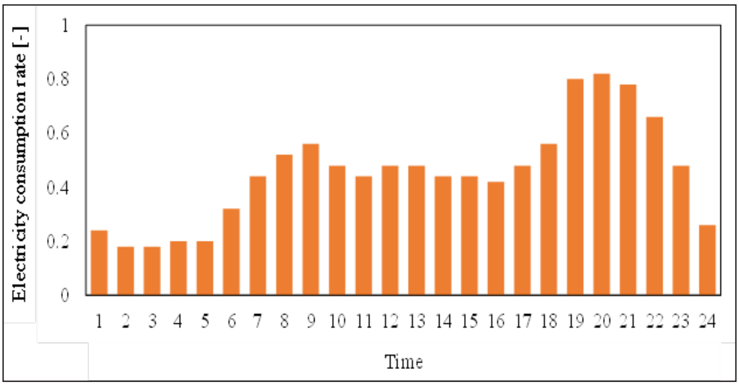

Figure 2. Conceptual diagram of the change in a house's daily electricity consumption. Energy consumption in the house is concentrated in the morning hours and in the evening to night hours

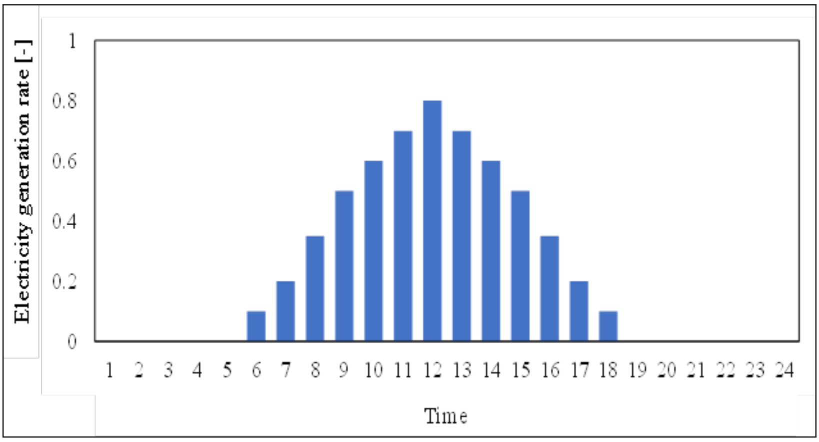

Figure 3. Conceptual diagram of the change in daily electricity generation. photovoltaic power generation is the largest at noon

Advantages of Electricity Sharing in a Housing Complex

In the wake of the Great East Japan Earthquake in 2011, the introduction of the distributed energy system has been considered and area-energy-using promoted as part of energy management measures in the residential sector (Akisawa & Takeshita, 2016; Kutsuki et al., 2008; Yuasa et al., 2007, 2020). This study introduces a photovoltaic power generation system in housing complexes as a distributed energy system. It investigates whether power generation and electricity consumption are possible considering the housing complexes' balance of supply and demand.

In the case of photovoltaic power generation on a house basis, when the amount of electricity consumption required is greater than that of electricity, the shortfall must be purchased from electricity companies. Conversely, when housing complexes are targeted, some houses have high electricity demand and others low due to differences in living patterns, even at the same time. Managing electrical energy for electricity demand throughout the housing complex can achieve the leveling of electricity demand by offsetting shortages and surpluses. Therefore, electricity can be used stably without additional electricity purchases from power companies.

Although photovoltaic panels are usually installed on roofs in individual houses, in the housing complexes, they can be installed not only on roofs but also in public areas such as passages, parking lots, and community centers, increasing the amount of electricity generation. In addition, it is unnecessary to install storage batteries with large capacity in individual houses as they are installed as common facilities.

Another benefit is that renewable energy, which is difficult to utilize in individual buildings due to the low economic feasibility of the return on investment, can be effectively used as an energy source, thereby reducing environmental load. Compared to the past, it is difficult to profit from the sale of surplus electricity due to the fall in the selling price of electricity sold to electricity companies (Ministry of Economy Trade and Industry Japan, 2021). In this study, surplus electricity is sold directly to nearby houses at a higher price than when selling electricity to electricity companies to make a higher profit from surplus electricity sales. In addition, the purchaser of surplus electricity is set up to purchase electricity at a lower price than when buying it from electricity companies. It is beneficial to both the seller and purchaser of surplus power.

METHODS

Target Housing Complexes and Analysis Tool

This study conducted numerical analysis on housing complexes in Busan, Korea, as shown in Figure 4. The complex consists of 56 houses of 13 types, including a community center.

The study investigated whether high and low electricity consumption could be offset by sharing electricity in the housing complexes. Electricity consumption and internal heat generation vary depending on family composition and lifestyle patterns. In this regard, all target households in the housing complexes were set up as a family of four. Each family member was designed by types A, B, and C. Type A consisted of a working husband, a full-time housewife, and two elementary school children. Type B consisted of a working husband, a full-time housewife, and two high school children. Type C consisted of a working husband, a full-time housewife, and two children of a worker. Tables 1–6 show occupant and internal heating schedules for types A, B, and C. In addition, Tables 7–12 are the cooling and heating schedules for each room of three types.

A numerical analysis using TRNSYS was conducted on the cooling and heating loads of each house in the housing complexes, electricity consumption, photovoltaic power generation, storage and discharge of storage batteries, purchase and sale of electricity, underground heat exchange, underground heat pump, hot-water heat pump, thermal energy storage tank, and heat exchanger. TRNSY is analysis software with an expandable and compatible module structure, allowing users to build systems and perform simulations according to their purposes (The University Wisconsin Madison, n.d.). Figure 5 shows the setting screen on TRNSYS. A calculates the photovoltaic power generation according to the photovoltaic panel's type, tilt angle, orientation, and total horizontal solar radiation. In contrast, B and C analyze heat pumps, thermal energy storage tanks, and heat exchangers for cooling, heating, and hot water supply. The heat source for cooling and heating and hot-water supply is set as the underground heat of E. The storage and discharge of electricity, surplus electricity, electricity sales, and electricity purchases were calculated at D by considering electricity consumption in each house, photovoltaic power generation at A, and electricity consumption for cooling and heating hot-water supply at B and C. The previous analysis estimated the electricity consumption of E, B, and C, and this article reports the results of A and D using the previous analysis results.

Figure 4. Target housing complex and arrangement of photovoltaic panels

Economic evaluations were performed on electricity purchases from electricity companies and surplus electricity sales, and environmental evaluations were conducted on the reduction of electricity purchases from electricity companies due to photovoltaic power generation and the resulting reduction in the amount of fossil fuels required for electricity generation.

Table 13 shows the heat transfer coefficient (U-value) of external walls, internal walls, floors, interlayer slabs, roofs, doors, and windows. The target housing complexes' insulation performance level is too high for energy conservation.

Table 1
Internal heat generation schedule of Type A (weekdays)

Zone	Heat gain	1:00	2:00	3:00	4:00	5:00	6:00	7:00	8:00	9:00	10:00	11:00	12:00	13:00	14:00	15:00	16:00	17:00	18:00	19:00	20:00	21:00	22:00	23:00	0:00
Living Room	Human body [W]	0	0	0	0	0	0	0	0	0	100	100	100	0	0	100	100	0	150	0	175	250	250	200	0
	Lighting [W]	4	4	4	4	4	4	40	40	40	40	4	4	4	4	4	4	4	40	40	40	40	40	40	4
	TV [W]	16	16	16	16	16	16	162	162	162	162	162	162	162	16	16	16	16	162	162	162	162	162	162	16
Dining Kitchen	Human body [W]	0	0	0	0	0	0	100	350	0	0	0	0	100	0	0	0	0	100	350	0	0	0	0	0
	Lighting [W]	4	4	4	4	4	4	40	40	40	40	4	4	4	4	4	4	4	40	40	40	40	40	40	4
	IH [W]	12	12	12	12	12	12	400	12	12	12	12	12	12	12	12	12	12	400	12	12	12	12	12	12
	Refrigerator [W]	11	11	11	11	11	11	11	11	11	11	11	11	11	11	11	11	11	11	11	11	11	11	11	11
	Rice cooker [W]	15	15	15	15	15	150	15	15	15	15	15	15	15	15	15	15	15	15	15	15	15	15	15	15
Bedroom 1	Human body [W]	200	200	200	200	200	200	100	0	0	0	0	0	0	0	0	0	0	0	0	100	0	0	0	200
	Lighting [W]	4	4	4	4	4	4	40	4	4	4	4	4	4	4	4	4	4	4	4	40	4	4	4	40
	Personal computer [W]	3	3	3	3	3	3	3	3	3	3	3	3	3	3	3	3	3	3	3	30	3	3	3	3
Bedroom 2	Human body [W]	75	75	75	75	75	75	75	0	0	0	0	0	0	0	0	0	0	0	0	0	0	0	75	75
	Lighting [W]	4	4	4	4	4	4	40	4	4	4	4	4	4	4	4	4	4	4	4	4	4	4	4	4
Bedroom 3	Human body [W]	75	75	75	75	75	75	75	0	0	0	0	0	0	0	0	0	0	0	0	0	0	0	75	75
	Lighting [W]	4	4	4	4	4	4	40	4	4	4	4	4	4	4	4	4	4	4	4	4	4	4	4	4
Others	Washing machine [W]	14	14	14	14	14	14	14	14	82	14	14	14	14	14	14	14	14	14	14	14	14	14	14	14
	Hair dryer [W]	0	0	0	0	0	0	0	0	82	0	0	0	0	0	0	0	0	0	0	100	100	0	0	0
	Vacuum cleaner [W]	0	0	0	0	0	0	0	0	83	0	0	0	0	0	0	0	0	0	0	0	0	0	0	0

Table 2
Internal heat generation schedule of Type A (weekend)

Zone	Heat gain	1:00	2:00	3:00	4:00	5:00	6:00	7:00	8:00	9:00	10:00	11:00	12:00	13:00	14:00	15:00	16:00	17:00	18:00	19:00	20:00	21:00	22:00	23:00	0:00
Living Room	Human body [W]	0	0	0	0	0	0	0	0	0	250	250	250	250	0	0	100	100	100	0	275	250	350	200	0
	Lighting [W]	4	4	4	4	4	4	4	40	40	40	4	4	4	4	4	4	40	40	40	40	40	40	40	4
	TV [W]	16	16	16	16	16	16	16	162	162	162	162	162	162	162	162	162	162	162	162	162	162	162	162	16
Dining Kitchen	Human body [W]	0	0	0	0	0	0	0	100	350	0	0	0	100	350	0	0	0	100	350	0	0	0	0	0
	Lighting [W]	4	4	4	4	4	4	4	40	40	40	4	4	4	4	4	4	40	40	40	40	40	40	40	4
	IH [W]	12	12	12	12	12	12	12	400	12	12	12	12	12	12	12	12	12	400	12	12	12	12	12	12
	Refrigerator [W]	11	11	11	11	11	11	11	11	11	11	11	11	11	11	11	11	11	11	11	11	11	11	11	11
	Rice cooker [W]	15	15	15	15	15	15	150	15	15	15	15	15	15	15	15	15	15	15	15	15	15	15	15	15
Bedroom 1	Human body [W]	200	200	200	200	200	200	200	100	0	100	100	100	0	0	100	100	100	0	0	0	0	0	0	200
	Lighting [W]	4	4	4	4	4	4	4	4	4	4	4	4	4	4	4	4	40	4	4	4	4	4	4	40
	Personal computer [W]	3	3	3	3	3	3	3	3	3	30	30	30	3	3	3	3	3	3	3	3	3	3	3	3
Bedroom 2	Human body [W]	75	75	75	75	75	75	75	75	0	0	0	0	0	0	75	75	75	75	0	0	0	0	75	75
	Lighting [W]	4	4	4	4	4	4	4	4	4	4	4	4	4	4	4	4	40	40	4	4	4	4	4	4
Bedroom 3	Human body [W]	75	75	75	75	75	75	75	75	0	0	0	0	0	0	75	75	75	75	0	0	0	0	75	75
	Lighting [W]	4	4	4	4	4	4	4	4	4	4	4	4	4	4	4	4	40	40	4	4	4	4	4	4
Others	Washing machine [W]	14	14	14	14	14	14	14	14	14	82	14	14	14	14	14	14	14	14	14	14	14	14	14	14
	Hair dryer [W]	0	0	0	0	0	0	0	0	0	0	0	0	0	0	0	0	0	0	0	100	100	0	0	0
	Vacuum cleaner [W]	0	0	0	0	0	0	0	0	0	0	0	0	0	0	83	0	0	0	0	0	0	0	0	0

Table 3
Internal heat generation schedule of Type B (weekdays)

Zone	Heat gain	1:00	2:00	3:00	4:00	5:00	6:00	7:00	8:00	9:00	10:00	11:00	12:00	13:00	14:00	15:00	16:00	17:00	18:00	19:00	20:00	21:00	22:00	23:00	0:00
Living Room	Human body [W]	0	0	0	0	0	0	0	0	0	100	100	100	0	0	100	100	0	0	0	300	300	200	200	0
	Lighting [W]	4	4	4	4	4	4	40	40	40	40	4	4	4	4	4	4	4	40	40	40	40	40	40	4
	TV [W]	16	16	16	16	16	16	162	162	162	162	162	162	162	16	16	16	16	162	162	162	162	162	162	16
Dining Kitchen	Human body [W]	0	0	0	0	0	0	100	400	0	0	0	0	100	0	0	0	0	100	400	0	0	0	0	0
	Lighting [W]	4	4	4	4	4	4	40	40	40	40	4	4	4	4	4	4	4	40	40	40	40	40	40	4
	IH [W]	12	12	12	12	12	12	400	12	12	12	12	12	12	12	12	12	12	400	12	12	12	12	12	12
	Refrigerator [W]	11	11	11	11	11	11	11	11	11	11	11	11	11	11	11	11	11	11	11	11	11	11	11	11
	Rice cooker [W]	15	15	15	15	15	150	15	15	15	15	15	15	15	15	15	15	15	15	15	15	15	15	15	15
Bedroom 1	Human body [W]	200	200	200	200	200	200	100	0	0	0	0	0	0	0	0	0	0	0	0	0	0	0	0	200
	Lighting [W]	4	4	4	4	4	4	40	4	4	4	4	4	4	4	4	4	4	4	4	4	4	4	4	40
	Personal computer [W]	3	3	3	3	3	3	3	3	3	3	3	3	3	3	3	3	3	3	3	3	3	3	3	30
Bedroom 2	Human body [W]	100	100	100	100	100	100	100	0	0	0	0	0	0	0	0	0	0	0	0	0	0	100	100	100
	Lighting [W]	4	4	4	4	4	4	40	4	4	4	4	4	4	4	4	4	4	4	4	4	4	40	40	40
	Personal computer [W]	3	3	3	3	3	3	3	3	3	3	3	3	3	3	3	3	3	3	3	3	3	30	30	3
Bedroom 3	Human body [W]	100	100	100	100	100	100	100	0	0	0	0	0	0	0	0	0	0	0	0	0	0	100	100	100
	Lighting [W]	4	4	4	4	4	4	40	4	4	4	4	4	4	4	4	4	4	4	4	4	4	40	40	40
	Personal computer [W]	3	3	3	3	3	3	3	3	3	3	3	3	3	3	3	3	3	3	3	3	3	30	30	3
Others	Washing machine [W]	14	14	14	14	14	14	14	14	82	14	14	14	14	14	14	14	14	14	14	14	14	14	14	14
	Hair dryer [W]	0	0	0	0	0	0	0	0	0	0	0	0	0	0	0	0	0	0	0	100	100	0	0	0
	Vacuum cleaner [W]	0	0	0	0	0	0	0	0	83	0	0	0	0	0	0	0	0	0	0	0	0	0	0	0

Table 4
Internal heat generation schedule of Type B (weekend)

Zone	Heat gain	1:00	2:00	3:00	4:00	5:00	6:00	7:00	8:00	9:00	10:00	11:00	12:00	13:00	14:00	15:00	16:00	17:00	18:00	19:00	20:00	21:00	22:00	23:00	0:00
Living Room	Human body [W]	0	0	0	0	0	0	0	0	0	300	300	300	300	0	100	200	200	100	0	300	300	400	400	0
	Lighting [W]	4	4	4	4	4	4	4	40	40	40	4	4	4	4	4	4	40	40	40	40	40	40	40	4
	TV [W]	16	16	16	16	16	16	16	162	162	162	162	162	162	162	162	162	162	162	162	162	162	162	162	16
Dining Kitchen	Human body [W]	0	0	0	0	0	0	0	100	400	0	0	0	100	400	0	0	0	100	400	0	0	0	0	0
	Lighting [W]	4	4	4	4	4	4	4	40	40	40	4	4	4	4	4	4	40	40	40	40	40	40	40	4
	IH [W]	12	12	12	12	12	12	12	400	12	12	12	12	12	12	12	12	12	400	12	12	12	12	12	12
	Refrigerator [W]	11	11	11	11	11	11	11	11	11	11	11	11	11	11	11	11	11	11	11	11	11	11	11	11
	Rice cooker [W]	15	15	15	15	15	15	150	15	15	15	15	15	15	15	15	15	15	15	15	15	15	15	15	15
Bedroom 1	Human body [W]	200	200	200	200	200	200	200	100	0	100	100	100	0	0	0	0	0	0	0	0	0	0	0	200
	Lighting [W]	4	4	4	4	4	4	4	4	4	4	4	4	4	4	4	4	4	4	4	4	4	4	4	40
	Personal computer [W]	3	3	3	3	3	3	3	3	3	30	30	30	3	3	3	3	3	3	3	3	3	3	3	3
Bedroom 2	Human body [W]	100	100	100	100	100	100	100	100	0	0	0	0	0	0	100	100	100	100	0	0	0	0	0	100
	Lighting [W]	40	4	4	4	4	4	4	4	4	4	4	4	4	4	4	4	40	40	4	4	4	4	4	40
	Personal computer [W]	3	3	3	3	3	3	3	3	3	3	3	3	3	3	3	30	30	30	3	3	3	3	3	3
Bedroom 3	Human body [W]	100	100	100	100	100	100	100	100	0	0	0	0	0	0	100	100	100	100	0	0	0	0	0	100
	Lighting [W]	40	4	4	4	4	4	4	4	4	4	4	4	4	4	4	4	40	40	4	4	4	4	4	40
	Personal computer [W]	3	3	3	3	3	3	3	3	3	3	3	3	3	3	3	30	30	30	3	3	3	3	3	3
Others	Washing machine [W]	14	14	14	14	14	14	14	14	14	82	14	14	14	14	14	14	14	14	14	14	14	14	14	14
	Hair dryer [W]	0	0	0	0	0	0	0	0	0	0	0	0	0	0	0	0	0	0	0	100	100	0	0	0
	Vacuum cleaner [W]	0	0	0	0	0	0	0	0	0	0	0	0	0	0	83	0	0	0	0	0	0	0	0	0

Table 5
Internal heat generation schedule of Type C (weekdays)

Heat gain	1:00	2:00	3:00	4:00	5:00	6:00	7:00	8:00	9:00	10:00	11:00	12:00	13:00	14:00	15:00	16:00	17:00	18:00	19:00	20:00	21:00	22:00	23:00	0:00
Human body [W]	0	0	0	0	0	0	0	0	0	100	100	100	0	0	100	100	0	0	0	100	100	200	200	0
Lighting [W]	4	4	4	4	4	4	40	40	40	40	4	4	4	4	4	4	4	40	40	40	40	40	40	4
TV [W]	16	16	16	16	16	16	162	162	162	162	162	162	162	16	16	16	16	162	162	162	162	162	162	16
Human body [W]	0	0	0	0	0	0	100	400	0	0	0	0	100	0	0	0	0	100	200	0	200	0	0	0
Lighting [W]	4	4	4	4	4	4	40	40	40	40	4	4	4	4	4	4	4	40	40	40	40	40	40	4
IH [W]	12	12	12	12	12	12	400	12	12	12	12	12	12	12	12	12	12	400	12	12	12	12	12	12
Refrigerator [W]	11	11	11	11	11	11	11	11	11	11	11	11	11	11	11	11	11	11	11	11	11	11	11	11
Rice cooker [W]	15	15	15	15	15	150	15	15	15	15	15	15	15	15	15	15	15	150	15	15	15	15	15	15
Human body [W]	200	200	200	200	200	200	100	0	0	0	0	0	0	0	0	0	0	0	0	0	100	100	0	200
Lighting [W]	4	4	4	4	4	4	40	4	4	4	4	4	4	4	4	4	4	4	4	4	40	40	4	40
Personal computer [W]	3	3	3	3	3	3	3	3	3	3	3	3	3	3	3	3	3	3	3	3	30	30	3	3
Human body [W]	100	100	100	100	100	100	100	0	0	0	0	0	0	0	0	0	0	0	0	0	0	0	100	100
Lighting [W]	4	4	4	4	4	4	40	4	4	4	4	4	4	4	4	4	4	4	4	4	4	4	40	40
Human body [W]	100	100	100	100	100	100	100	0	0	0	0	0	0	0	0	0	0	0	0	0	0	0	100	100
Lighting [W]	4	4	4	4	4	4	40	4	4	4	4	4	4	4	4	4	4	4	4	4	4	4	40	40
Washing machine [W]	14	14	14	14	14	14	14	14	82	14	14	14	14	14	14	14	14	14	14	14	14	14	14	14
Hair dryer [W]	0	0	0	0	0	0	0	0	0	0	0	0	0	0	0	0	0	0	0	100	0	100	0	0
Vacuum cleaner [W]	0	0	0	0	0	0	0	0	83	0	0	0	0	0	0	0	0	0	0	0	0	0	0	0

Table 6
Internal heat generation schedule of Type C (weekend)

Zone	Heat gain	1:00	2:00	3:00	4:00	5:00	6:00	7:00	8:00	9:00	10:00	11:00	12:00	13:00	14:00	15:00	16:00	17:00	18:00	19:00	20:00	21:00	22:00	23:00	0:00
Living Room	Human body [W]	0	0	0	0	0	0	0	0	0	100	100	100	100	0	0	100	100	100	0	300	300	200	200	0
	Lighting [W]	4	4	4	4	4	4	4	40	40	40	4	4	4	4	4	4	40	40	40	40	40	40	40	4
	TV [W]	16	16	16	16	16	16	16	162	162	162	162	162	162	162	162	162	162	162	162	162	162	162	162	16
Dining Kitchen	Human body [W]	0	0	0	0	0	0	0	100	400	0	0	0	100	200	0	0	0	100	400	0	0	0	0	0
	Lighting [W]	4	4	4	4	4	4	4	40	40	40	4	4	4	4	4	4	40	40	40	40	40	40	40	4
	IH [W]	12	12	12	12	12	12	12	400	12	12	12	12	12	12	12	12	12	400	12	12	12	12	12	12
	Refrigerator [W]	11	11	11	11	11	11	11	11	11	11	11	11	11	11	11	11	11	11	11	11	11	11	11	11
	Rice cooker [W]	15	15	15	15	15	15	150	15	15	15	15	15	15	15	15	15	15	150	15	15	15	15	15	15
Bedroom 1	Human body [W]	200	200	200	200	200	200	200	100	0	100	100	100	0	0	100	100	100	0	0	0	0	0	0	200
	Lighting [W]	4	4	4	4	4	4	4	4	4	4	4	4	4	4	4	4	40	4	4	4	4	4	4	40
	Personal computer [W]	3	3	3	3	3	3	3	3	3	30	30	30	3	3	3	3	3	3	3	3	3	3	3	3
Bedroom 2	Human body [W]	100	100	100	100	100	100	100	100	0	0	0	0	0	0	0	0	100	100	0	0	0	100	100	100
	Lighting [W]	40	4	4	4	4	4	4	4	4	4	4	4	4	4	4	4	40	40	4	4	4	40	40	40
Bedroom 3	Human body [W]	100	100	100	100	100	100	100	100	0	0	0	0	0	0	0	0	100	100	0	0	0	100	100	100
	Lighting [W]	40	4	4	4	4	4	4	4	4	4	4	4	4	4	4	4	40	40	4	4	4	40	40	40
Others	Washing machine [W]	14	14	14	14	14	14	14	14	14	14	82	14	14	14	14	14	14	14	14	14	14	14	14	14
	Hair dryer [W]	0	0	0	0	0	0	0	0	0	0	0	0	0	0	0	0	0	0	0	100	100	0	0	0
	Vacuum cleaner [W]	0	0	0	0	0	0	0	0	0	0	0	0	0	0	83	0	0	0	0	0	0	0	0	0

Table 7
Heating and cooling schedule of Type A (weekdays)

Zone	1:00	2:00	3:00	4:00	5:00	6:00	7:00	8:00	9:00	10:00	11:00	12:00	13:00	14:00	15:00	16:00	17:00	18:00	19:00	20:00	21:00	22:00	23:00	0:00
Living Room										■	■	■	■	■	■	■	■	■	■	■	■	■	■	
Dining Kitchen							■	■	■	■	■	■	■	■	■	■	■	■	■					
Bedroom 1	■	■	■	■	■	■	■													■	■	■	■	■
Bedroom 2	■	■	■	■	■	■	■																■	■
Bedroom 3	■	■	■	■	■	■	■																■	■

Table 8
Heating and cooling schedule of Type A (weekend)

Zone	1:00	2:00	3:00	4:00	5:00	6:00	7:00	8:00	9:00	10:00	11:00	12:00	13:00	14:00	15:00	16:00	17:00	18:00	19:00	20:00	21:00	22:00	23:00	0:00
Living Room										■	■	■	■	■	■	■	■	■	■	■	■	■	■	
Dining Kitchen								■	■	■	■	■	■	■	■	■	■	■	■					
Bedroom 1	■	■	■	■	■	■	■	■	■	■	■	■	■	■	■	■	■							■
Bedroom 2	■	■	■	■	■	■	■	■								■	■	■					■	■
Bedroom 3	■	■	■	■	■	■	■	■								■	■	■					■	■

Table 9
Heating and cooling schedule of Type B (weekdays)

Zone	**1:00**	**2:00**	**3:00**	**4:00**	**5:00**	**6:00**	**7:00**	**8:00**	**9:00**	**10:00**	**11:00**	**12:00**	**13:00**	**14:00**	**15:00**	**16:00**	**17:00**	**18:00**	**19:00**	**20:00**	**21:00**	**22:00**	**23:00**	**0:00**
Living Room										■	■	■	■	■	■	■	■	■	■	■	■	■	■	
Dining Kitchen							■	■	■	■	■	■	■	■	■	■	■	■	■					
Bedroom 1	■	■	■	■	■	■	■																	■
Bedroom 2	■	■	■	■	■	■	■															■	■	■
Bedroom 3	■	■	■	■	■	■	■															■	■	■

Table 10
Heating and cooling schedule of Type B (weekend)

Zone	**1:00**	**2:00**	**3:00**	**4:00**	**5:00**	**6:00**	**7:00**	**8:00**	**9:00**	**10:00**	**11:00**	**12:00**	**13:00**	**14:00**	**15:00**	**16:00**	**17:00**	**18:00**	**19:00**	**20:00**	**21:00**	**22:00**	**23:00**	**0:00**
Living Room										■	■	■	■	■	■	■	■	■	■	■	■	■	■	
Dining Kitchen							■	■	■	■	■													
Bedroom 1	■	■	■	■	■	■	■	■	■	■	■													■
Bedroom 2	■	■	■	■	■	■	■								■	■	■	■						■
Bedroom 3	■	■	■	■	■	■	■								■	■	■	■						■

Table 11
Heating and cooling schedule of Type C (weekdays)

Zone	**1:00**	**2:00**	**3:00**	**4:00**	**5:00**	**6:00**	**7:00**	**8:00**	**9:00**	**10:00**	**11:00**	**12:00**	**13:00**	**14:00**	**15:00**	**16:00**	**17:00**	**18:00**	**19:00**	**20:00**	**21:00**	**22:00**	**23:00**	**0:00**
Living Room										■	■	■	■	■	■	■	■	■	■	■	■	■	■	
Dining Kitchen							■	■	■	■	■	■	■	■	■	■	■	■	■	■	■			
Bedroom 1	■	■	■	■	■	■	■														■	■	■	■
Bedroom 2	■	■	■	■	■	■	■																■	■
Bedroom 3	■	■	■	■	■	■	■																■	■

Table 12
Heating and cooling schedule of Type C (weekend)

Zone	**1:00**	**2:00**	**3:00**	**4:00**	**5:00**	**6:00**	**7:00**	**8:00**	**9:00**	**10:00**	**11:00**	**12:00**	**13:00**	**14:00**	**15:00**	**16:00**	**17:00**	**18:00**	**19:00**	**20:00**	**21:00**	**22:00**	**23:00**	**0:00**
Living Room										■	■	■	■	■	■	■	■	■	■	■	■	■	■	
Dining Kitchen								■	■	■	■	■	■	■	■	■	■	■	■					
Bedroom 1	■	■	■	■	■	■	■	■	■	■	■	■	■	■	■	■	■							■
Bedroom 2	■	■	■	■	■	■	■	■									■	■				■	■	■
Bedroom 3	■	■	■	■	■	■	■	■									■	■				■	■	■

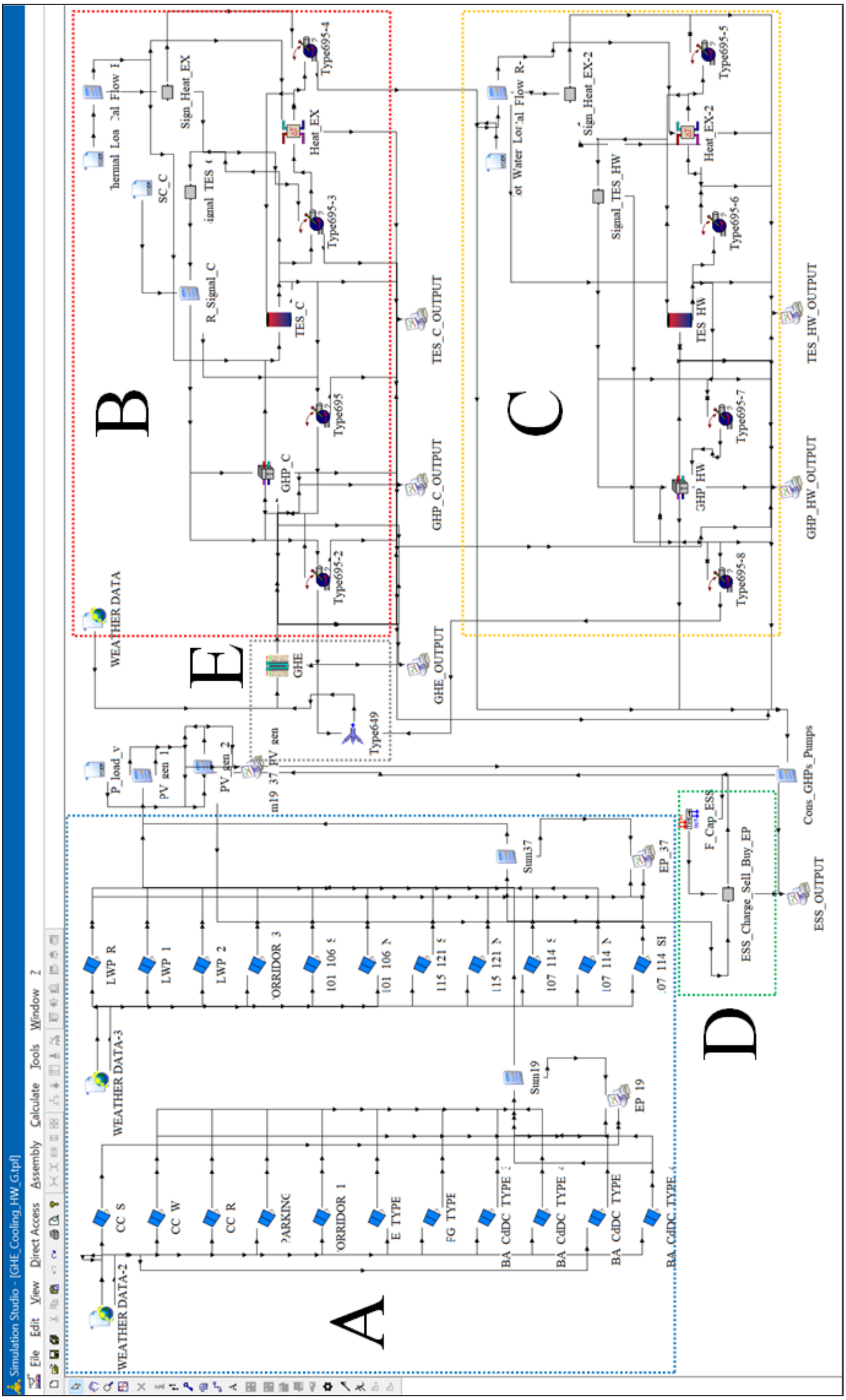

Figure 5. Setting screen of the file that was analyzed by TRNSYS

Table 13
Heat transfer coefficient of each construction type

Construction type	**External wall**	**Internal wall**	**Floor**	**Interlayer slabs**
U-value (W/(m2·K))	0.147	2.044	0.138	0.806
Construction type	Roof	Metal door	Wood door	Window (triple glass)
U-value (W/(m2·K))	0.103	0.151	0.935	0.580

Electricity Sharing System

As shown in Figure 4, photovoltaic panels were installed not only on the roofs of the houses but also in parking lots, community centers, and passages in the target housing complexes. Tables 14 and 15 show the specifications of photovoltaic panels installed in the housing complexes and the rated capacity, azimuth, and tilt angles of photovoltaic panels by installation location. Additionally, the interconversion rate between DC and AC electricity when charging the generated electricity and discharging the storage battery was set to 0.98.

Table 14
Specifications of photovoltaic panels

Reference cell temperature [℃]	**25**
Reference solar radiation [W/㎡]	1000
Temperature coefficient of short circuit current [A/K]	0.00043
Temperature coefficient of release voltage [V/K]	-0.00277
Number of cells connected in series within a module [pieces]	78
Nominal operating cell temperature [℃]	45

Table 15
Related capacity of photovoltaic module, azimuth, and tilt angles of photovoltaic panels

Installation location	**Rated capacity of photovoltaic module [W]**	**Azimuth [°]**	**Tilt angle [°]**
Parking lot	450	-28.00	15.00
Community Center	360	-28.00	90.00
House	430	-35.00	22.52
Passage 1	450	-2.50	48.30
Passage 2	430	-2.50	48.30

Table 16 shows the specifications of storage batteries. Power Conditioning System (PCS) capacity is the performance that can charge and discharge electricity from a storage battery per hour.

Table 16
Specifications of storage batteries

Electricity storage capacity [kWh]	**400**
Minimum charging rate	0.2
Maximum charging rate	0.8
PCS capacity[kW]	200
Charge/discharge rate	0.98

Considering electricity consumption, photovoltaic power generation, remaining capacity of storage batteries, electricity storage rate, and discharge rate, it had to be determined whether to sell, purchase, or store electricity. Thus, a new component was added to TRNSYS to perform this determination on the calculation. The added component is D in Figure 4. Figure 6 shows the logic of determining the judgment in the newly added component.

Economic Evaluation

Depending on the presence or absence of photovoltaic power generation and the target for the sale of surplus electricity, costs and profits are calculated for the following three conditions. First, all the electricity required in housing complexes is purchased from the electricity company. Photovoltaic power generation is not considered in this condition. When the photovoltaic power generation is greater than the electricity consumption, profits are calculated for two conditions: selling surplus electricity to nearby houses or electricity companies. In the opposite case, the cost of purchasing insufficient electricity from an electricity company is calculated. The price for selling photovoltaic power to an electricity company was 171 KRW/kWh, and that for selling to nearby houses was 187 KRW/kW. In addition, the price of purchasing electricity from an electricity company was 234.3 KRW/kWh (https://cyber.kepco.co.kr/ckepco/front/jsp/CY/J/A/CYJAPP000NFL.jsp). When calculating the electricity transmission loss, the resistance on one line of the high voltage was 0.103 Ω/km; the transmission voltage was 6600 V, and the transmission distance was assumed to be 0.13 km when transmitting from the housing complexes to nearby houses and 10 km when transmitting to the electricity company. The electricity loss in the pole transformer was assumed to be 3%.

Environmental Evaluation

CO_2 emissions when using thermal power-generated electricity for all the electricity consumed in the housing complexes and when using thermal power-generated electricity only for electricity insufficient for photovoltaic power generation, that is, the amount of electricity purchased, were compared. As much as the electricity obtained by photovoltaic

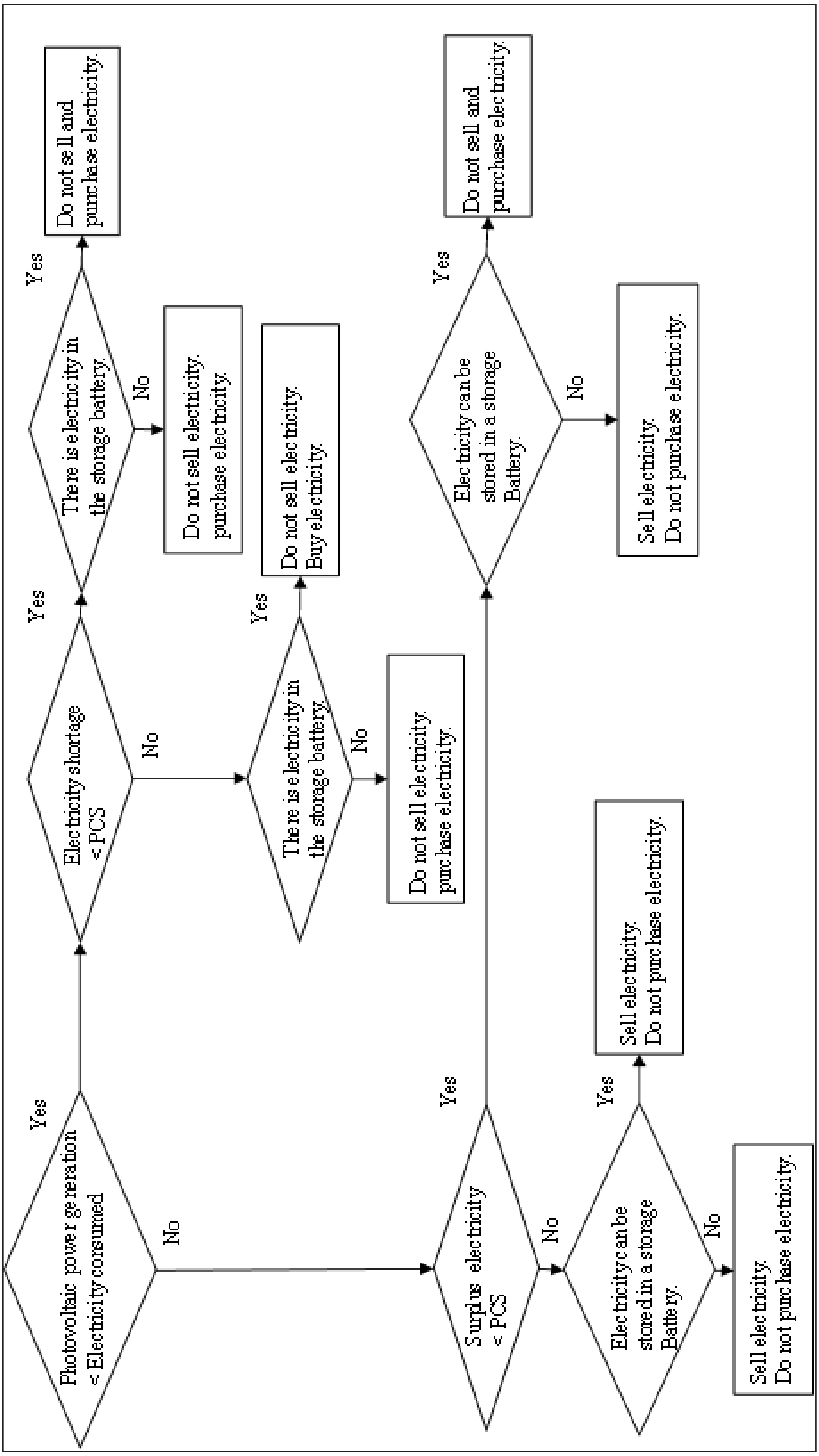

Figure 6. Flowchart for the determination of electricity sharing, selling, or buying

power generation, fossil fuels for thermal power generation are reduced, and CO_2 emissions generated during the combustion of fossil fuels are also reduced. Therefore, the reduction ratio of CO_2 emissions according to each type of fossil fuel matches the ratio of purchased electricity according to the presence or absence of solar power generation. Three types of fuel are mainly used in the case of thermal power generation: liquefied natural gas (LNG), coal, and oil. Thus, CO_2 emission was compared for power generation using these three types of fossil fuels. The unit calorific value of coal was 25.7 MJ/kg, the unit calorific value of LNG was 54.6 MJ/kg, and the unit calorific value of heavy oil A was 39.1 MJ/kg. The unit CO2 emissions of coal, heavy oil A and LNG were set at 2.419 kgCO2/kg, 3.151 kgCO2/kg and 2.698 kgCO2/kg, respectively. In addition, the energy conversion efficiency of thermal power generation was assumed to be 43%.

RESULTS AND DISCUSSION

Electricity Generation, Surplus Electricity Sale

Figure 7 shows the monthly electricity generation by photovoltaic panels. Figure 8 shows the monthly surplus electricity obtained by subtracting electricity consumption from photovoltaic generation. According to the calculation results, the annual photovoltaic power generation in the housing complexes was 556 MWh—3.1 times the annual electricity consumption of 180 MWh. In addition, as shown in Figure 8, electricity generation exceeded power consumption in all months; thus, the electricity generation performance of the target housing complexes was sufficient. The annual electricity purchase of the target housing complexes was 87 MWh—a 52% reduction in annual electricity purchases by introducing an electricity sharing system compared to when electricity companies purchased all electricity consumed annually without photovoltaic power generation. In

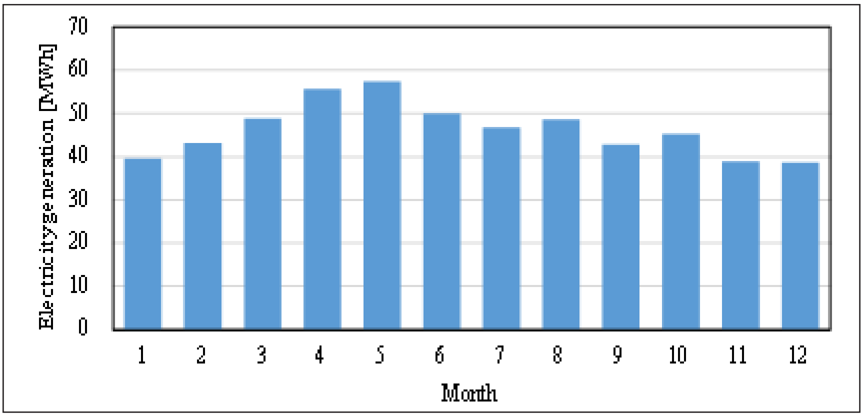

Figure 7. Monthly electricity generation by photovoltaic panels. the annual photovoltaic power generation in housing complexes was 556 MWh

addition, the annual electricity sale was 433 MWh, meaning that 77.8% of the electricity generated annually was sold; 14.1% (25.4 MWh) of the annual electricity consumption of 180 MWh was discharged from the storage battery.

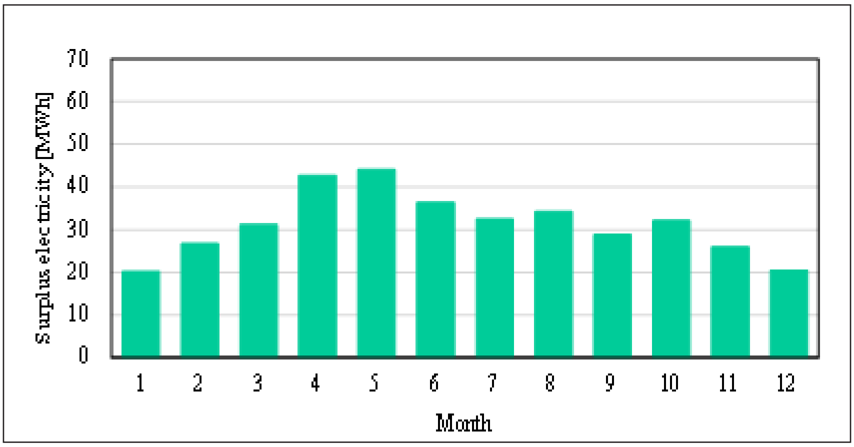

Figure 8. Monthly surplus electricity obtained by subtracting electricity consumption from photovoltaic generation. Electricity generation exceeded power consumption in all months

Economic Evaluation

Figure 9 shows the annual electricity charges per household for 56 households in the housing complexes, divided into cases in which all electricity consumption was purchased, surplus electricity was sold to nearby houses, and surplus electricity was sold to electricity

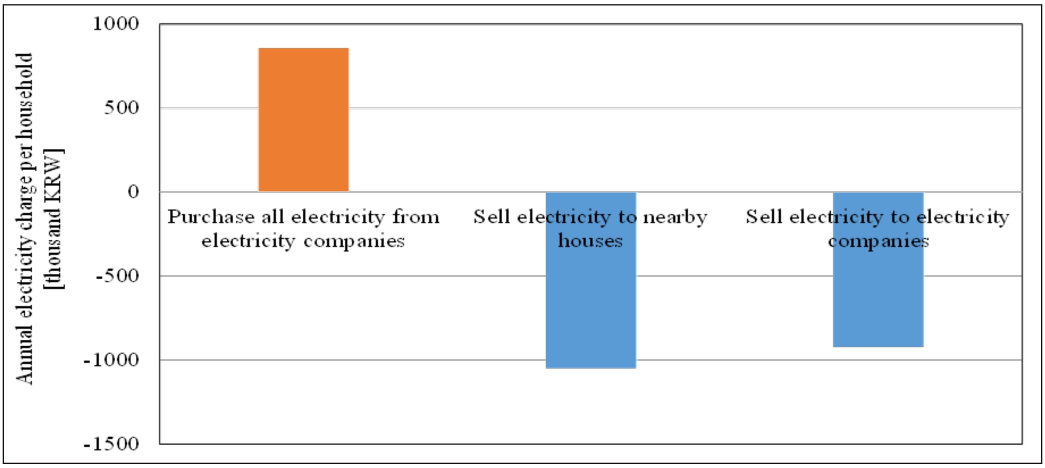

Figure 9. Annual electricity charges per household for 56 households in a housing complex. Selling surplus electricity directly to nearby houses can be expected to yield about 1.14 times the profit compared to selling to electricity companies

companies. Electricity charges per household were not applied to progressive rates according to electricity consumption. If all the power consumed was purchased from an electricity company, the annual electricity charge per household was 856.8 thousand KRW. In contrast, if surplus electricity was sold to a nearby house or power company, the profit was 1049.2 thousand KRW or 921.0 thousand KRW, respectively. Therefore, selling surplus electricity directly to nearby houses can yield about 1.14 times the profit compared to selling to electricity companies.

Figure 10 shows the electricity transmitted when surplus electricity was sold to nearby houses and sold to an electricity company. This difference is because transmission loss is considered according to transmission distance. Based on the electricity transmitted from the target housing complexes, the proportion of the electricity received by nearby houses was 94.08%; for electricity companies, it was 93.27%. However, the efficiency of electricity reception when transmitting electricity to a nearby house is only about 0.81% different from that when transmitting electricity to an electricity company and retransmitting it to consumers. Accordingly, the effect of transmission distance on transmission loss is significantly small.

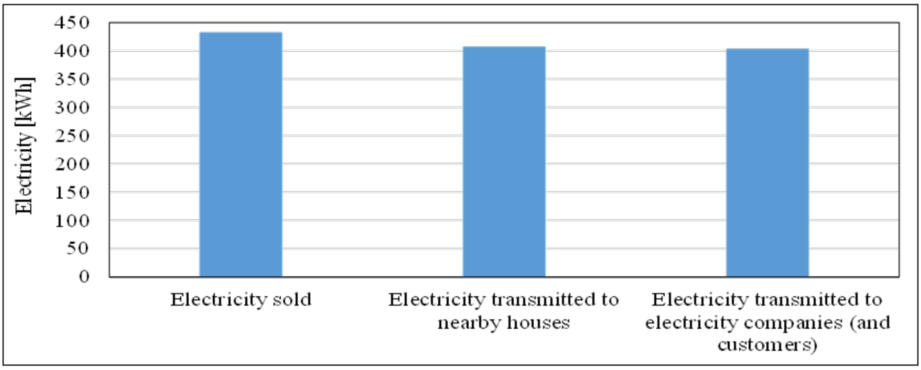

Figure 10. Actual electricity was transmitted when surplus electricity was sold to nearby houses and sold to an electricity company. The effect of transmission distance on transmission loss is significantly small

Environmental Evaluation

Figure 11 shows the requirements of coal, LNG, and heavy oil A when using only electricity generated by thermal power and electricity generated by photovoltaic power first, then making up for the shortfall by thermal power generation. Figure 12 shows CO_2 emissions when generated using these fossil fuels. Using electricity generated by photovoltaic power first and making up for the shortage with thermal power generation can reduce the amount of fossil fuel and CO_2 emissions by 56.2% compared to using only electricity generated by thermal power, regardless of the type of fossil fuel of coal, LNG, and heavy oil A.

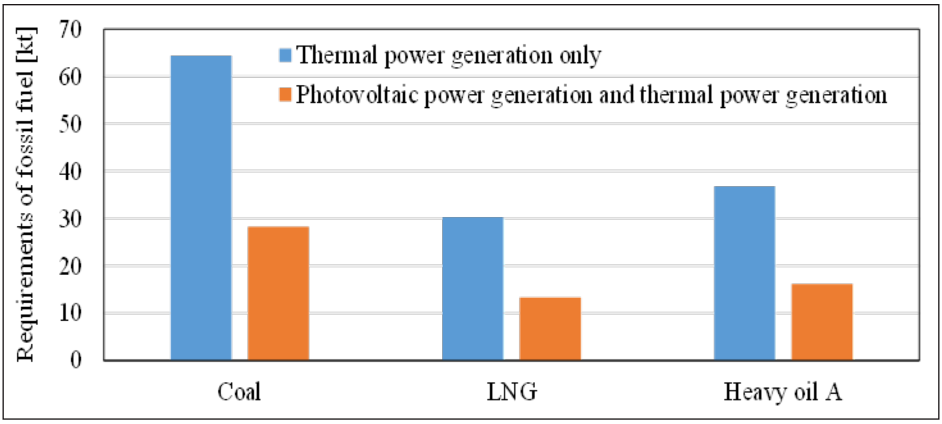

Figure 11. Requirements of coal, LNG, and heavy oil A needed for electricity generation

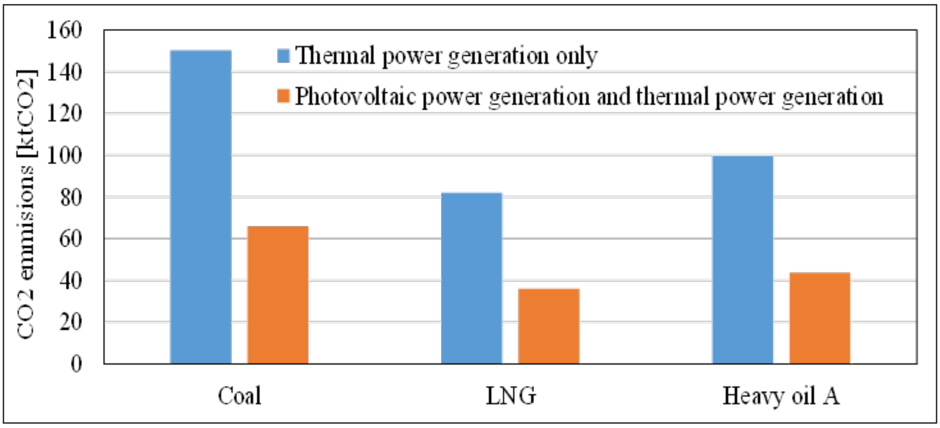

Figure 12. CO_2 emissions when generated using coal, LNG, and heavy oil A. The proposed energy-sharing system can reduce CO_2 emissions by about 56.2%

CONCLUSION

In this study, photovoltaic panels and large-capacity storage batteries were installed as distributed energy systems in the housing complexes. TRNSYS simulation evaluated whether the proposed electricity sharing system could enable a stable use of electricity by offsetting its surplus and shortage due to differences in family composition and lifestyle patterns. In addition, this study economic and environmental evaluations of the proposed electricity sharing system and drew the following conclusion:

1. A method of storing electricity generated during the day in the storage battery is useful as a time gap exists between the daytime when photovoltaic power generation is available and the morning and evening hours when electricity consumption is concentrated.

2. Photovoltaic panels were installed in parking lots, corridors, community centers, and roofs of entire housing complexes—not single houses—to offset the surplus and shortage of electricity due to differences in family composition and lifestyle patterns. The electricity generated was stored in a large-capacity storage battery.
3. Housing complexes primarily consume electricity generated by photovoltaic panels. Then, to make profits, surplus electricity was supplied to nearby houses at a lower price than the electricity company's supply price and at a higher price than when selling electricity to the electricity company.
4. TRNSYS was added with a new component to determine whether to sell, purchase or store electricity. This component considers electricity consumption, photovoltaic power generation, the remaining capacity of storage batteries, the electricity storage rate, and the discharge rate.
5. The annual photovoltaic power generation in the target housing complexes was 3.1 times the annual electricity consumption, and monthly photovoltaic power generation also exceeded the electricity consumption in all months.
6. As an economic benefit, 1049.2 KRW was generated annually when surplus electricity from photovoltaic power generation was sold to nearby houses.
7. Using electricity generated by photovoltaic power first and making up for the shortage with thermal power generation can reduce fossil fuel and CO_2 emissions by 56.2%.

The above analysis confirmed that the proposed electricity-sharing system could supply stable electricity and have excellent economic and environmental performance. As a future task, it will be necessary to examine not only a method of storing surplus electricity in a storage battery but also one of predicting future thermal load, as well as storing cold or warm heat in a thermal energy storage tank in advance using surplus electricity.

ACKNOWLEDGEMENT

The authors are grateful to the Korea Institute of Energy Research for providing technical data on buildings and machinery.

REFERENCES

Akisawa, A., & Takeshita, N. (2016). Optimal technical configuration of distributed energy system for apartment complexes considering energy supply maintenance during emergencies. *Journal of the Society of Energy and Resources*, *37*(1), 1-8. https://doi.org/10.24778/jjser.37.1_1

Iwata, T., Tanaka, K., Kato, D., Kimura, M., Matsuhashi, R., & Yamada, K. (2012). Study on estimation of hourly electricity consumption in residential sector in 2011 summer. *Environmental Information Science Academic Research Papers, 26*, 255-260.

Korea Power Exchange (2019) *Information on the electricity market*. Korea Power Exchange. https://new.kpx.or.kr/board.es?mid=a10109010200&bid=0077&act=view&list_no=57652

Kutsuki, R., Murakami, S. Sadowara, S., Ichikawa, T. Aosasa, K., Hasegawa, I., Yanai, T., Anna, F., & Mitsui, K. (2008). Research on improving the sustainability of city blocks through the widespread use of distributed energy systems. *Architectural Institute of Japan Technical Report, 14*(28), 497-502.

Lee, S. (2019). *Domestic and international smart city promotion trends and business feasibility analysis*. Monthly Electrical Journal. http://www.keaj.kr/news/articleView.html?idxno=2511

Lim, Y., Edelenbos, J., & Gianoli, A. (2019). Smart energy transition: An evaluation of cities in South Korea. *Informatics, 6*(4), Article 50. https://doi.org/10.3390/informatics6040050.

Ministry of Economy Trade and Industry Japan. (2021). *The purchase price is decided on, levy unit price, etc. for FY2021 under the FIT system*. Ministry of Economy Trade and Industry, Japan. https://www.meti.go.jp/press/2020/03/20210324004/20210324004.html

Ministry of Economy, Trade and Industry Japan. (2020). *Energy white paper 2020*. Ministry of Economy, Trade and Industry Japan. https://www.enecho.meti.go.jp/about/whitepaper/2020pdf/whitepaper2020pdf_2_1.pdf

Ministry of Land, Infrastructure Japan. (2012). *Regarding carbon.dioxide emissions and reductions related to houses and buildings*. Ministry of Land, Infrastructure Japan. https://www.env.go.jp/council/06earth/y0614-03/mat02.pdf

Nam., H. (2020). Impact of nuclear phase-out policy and energy balance in 2029 based on the 8th Basic Plan for long-term electricity supply and demand in South Korea. *Renewable and Sustainable Energy Reviews*, *122,* Article 109723. https://doi.org/10.1016/j.rser.2020.109723

Solar Power Association Japan (2020). *Calculation committee materials*. Solar Power Association Japan. https://www.meti.go.jp/shingikai/santeii/pdf/062_01_00.pdf

The University Wisconsin Madison (n. d.) *A transient systems simulation program*. The University Wisconsin Madison. https://sel.me.wisc.edu/trnsys/

Yuasa, K., Liu, Z., & Fujii, S. (2007). Research on the possibility of introducing distributed energy systems to apartment buildings. *Proceedings of the Architectural Institute of Japan, Environmental Studies, 72*(621), 51-56.

Yuasa, K., Yu, S., & Wei, W. (2020). Energy interchange using fuel cell cogeneration in complex housing complexes. *Architectural Institute of Japan Environmental Research Proceedings, 85*(772), 485-493.

Pertanika J. Sci. & Technol. 33 (S2): 53 - 71 (2025)

SCIENCE & TECHNOLOGY

Journal homepage: http://www.pertanika.upm.edu.my/

The Proposal for Ceiling-Hanging Panels and its Impact on Cooling Efficiency

Kae Takeda[1], Ryo Fujimoto[2], Shizuo Iwamoto[2] and Wanghee Cho[3]*

[1]*Graduate school, Department of Civil and Architectural Engineering, Kyushu Institute of Technology, 1-1 Sensuicho, Tobataku, Kitakyushu, 804-8550, Japan*
[2]*Department of Architecture and Building Engineering, Faculty of Architecture and Building Engineering, Kanagawa University, 3-27-1 Rokkakubashi, Kanagawaku, Yokohama 221-8686, Japan*
[3]*Department of Civil and Architectural Engineering, Kyushu Institute of Technology, 1-1 Sensuicho, Tobataku, Kitakyushu, 804-8550, Japan*

ABSTRACT

The study focused on air-conditioning status when different air-conditioning loads occur in a single space to achieve cooling that is not separated by walls in an office building. In this case, whether all or only some of the air-conditioning units are operated, the problem is that the air-conditioning system blows air into zones that do not require cooling. To resolve this inefficiency, the study focused on the circulating air flow generated by the interchange of supply air and return air from the air-conditioning system. As a solution to trap air flow from an air-conditioning unit into a zone that requires cooling, a method for vertically installing panels on the ceiling is proposed. The analysis was performed by Computational Fluid Dynamics analysis while changing the length of the ceiling-hanging panel length conditions (350 mm, 700 mm, and 1100 mm); the blowing angle from the air-conditioning unit (15°, 30°, and 45°); and the blowing direction from the air-conditioning unit (4 directions and 2 directions). The ceiling-hanging panels and partitions are installed between the target zone where the air-conditioning unit is operated and the non-target zone where the air-conditioning unit is not operated. Cooling efficiencies were 84.0% when both panels and partitions were installed and 82.8% when both were not installed. However, when only the ceiling-hanging panels were installed, the cooling efficiency was 89.9%. The cooling efficiency was improved by about 5.9% by simply installing the ceiling-hanging panels.

Keywords: Ceiling-hanging panel, circulating airflow, cooling efficiency, partition

ARTICLE INFO

Article history:
Received: 13 February 2023
Accepted: 18 October 2024
Published: 25 February 2025

DOI: https://doi.org/10.47836/pjst.33.S2.04

E-mail addresses:
takeda.kae365@mail.kyutech.jp (Kae Takeda)
ryo-fujimoto@kanagawa-u.ac.jp (Ryo Fujimoto)
iwamos01@jindai.jp (Shizuo Iwamoto)
chowh@civil.kyutech.ac.jp (Wanghee Cho)
*Corresponding author

INTRODUCTION

In medium-sized and large office buildings, different air-conditioning loads may occur

ISSN: 0128-7680
e-ISSN: 2231-8526

in a single space due to (1) a constantly used office zone and an occasionally used meeting zone being located in the same space that is separated by a wall; (2) the general office department and sales department, which have significantly different occupancy rates, being located in the same area; and (3) a lack of in-office attendance given the high rate of employees working from home as a result of Corona Virus Infectious Disease-19 as well as the development of the Internet of Things. For the first case, Figure 1 shows the scenario wherein the respective air-conditioning units in the occupied office zone and unoccupied meeting zone are operated. Figure 2 shows when only the occupied office zone air-conditioning unit is operated.

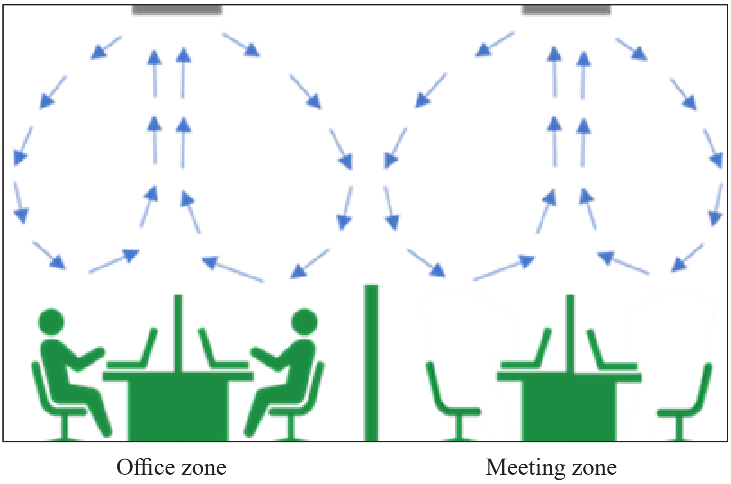

Figure 1. Conditions for operating both air-conditioning units. In this case, power consumption increases

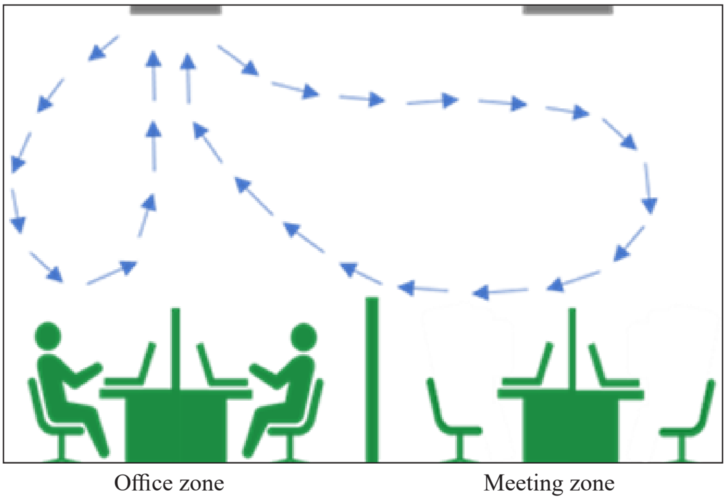

Figure 2. Conditions for operating only the office zone air-conditioning unit. In this case, a faster blowing speed or a lower air temperature is achieved

If the respective air-conditioning units are operated in both spaces, as seen in Figure 1, a comfortable air temperature can be maintained throughout the entire area. However, power consumption increases since the air-conditioning unit is operated in the unoccupied meeting zone, which does not require cooling. Conversely, Figure 2 shows the scenario wherein the air-conditioning is only operated in the occupied office zone. Given that only one air-conditioning unit processes the load of the entire space, either a faster blowing speed or a lower air temperature is achieved. As a result, either very strong airflow or the temperature in the unit is too cold, which may cause thermal discomfort to zone occupants. However, an air-conditioning load far from the unit may sometimes not be processed.

Nishimura et al. (2006) analyzed the indoor thermal environment in summer by changing the occupancy rate and the number of operating air-conditioning units by Computational Fluid Dynamics (CFD) analysis. The results showed that the entire room is too cooled if all air-conditioning units are operated despite a low occupancy rate. Meanwhile, if only some air-conditioning units are operated according to the occupancy rate, a large amount of cold air leaks into the zones wherein air-conditioning units are not operated, increasing the burden on the units. Therefore, an efficient air-conditioning method focused on the thermal comfort of occupants and energy conservation is needed when the occupancy rate is low or only a part of the space is used.

A personal air-conditioning system that can control the thermal environment in desk areas according to individual preferences has been proposed (De Dear & Brager, 1998; Sudo et al., 2004). Furthermore, this system can be installed on furnishings such as chairs and desks. Also, even if the occupancy rate is low, the personal units can be cooled only in areas where required. However, a personal air-conditioning method requires a separate facility design from the construction stage and is unsuitable for existing buildings as well as tenant buildings that regularly change layout. Although an existing method of installing a ceiling fan near the air-conditioning unit blowout to create airflow improves the thermal comfort of occupants and reduces the air-conditioning energy used (Lipczynska et al., 2018; Mizuide et al., 2007), the main purpose of this method is to create a uniformed thermal environment for the entire space such that even if the occupancy rate is low, the load processed by anyone air-conditioning unit for the entire space remains unchanged.

Another method has also been proposed: an air-conditioning system that changes unit blowout direction or temperature by measuring occupants' skin temperature or heart rate. However, this is mainly for housing and is unsuitable for office buildings (Miwa et al., 2014).

A study by Murakami and Kato (1986) confirmed that the indoor temperature field is formed by the circulating air flow generated by the interchange of supply air and return air from the air-conditioning units. Therefore, as shown in Figure 3, this study proposes a ceiling-hanging panel vertically attached to the ceiling so that airflow is trapped in a zone that requires cooling, with the air-conditioning system only processing the target zone load. The panel is made of transparent material such as acrylic to avoid blocking light. The proposed method can improve air-conditioning efficiency in existing buildings by installing cost-effective panels on the ceiling without an additional air-conditioning system design or changing the office layout. This study aims to quantitatively evaluate the effect of the proposed ceiling-hanging panel by CFD analysis on cooling efficiency.

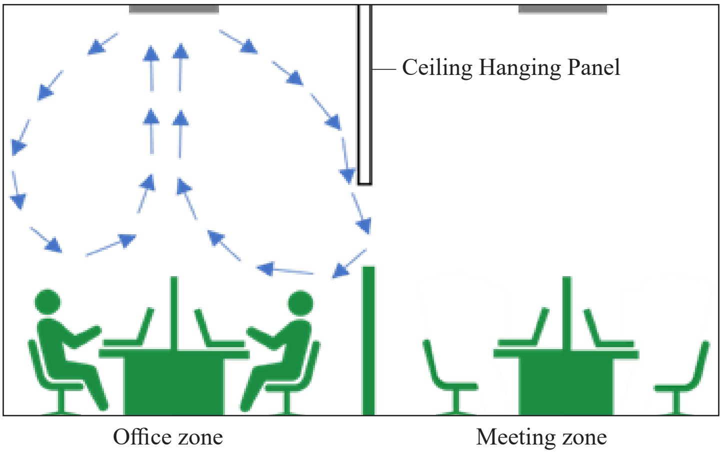

Figure 3. Concept of ceiling-hanging panel. Vertically attached to the ceiling, airflow is trapped in a zone that requires cooling, with the air-conditioning system only processing the target zone load

MATERIALS AND METHODS

To identify the effect of ceiling-hanging panels on cooling efficiency, the indoor air temperature distribution, airflow distribution, and average air temperature were evaluated using CFD analysis (https://www.cradle-cfd.com/product/scflow.html).

Figure 4 shows the office floor plan analyzed in this study. To ensure the effect of ceiling-hanging panels on the air-conditioning efficiency of the air-conditioning system, the office floor plan was simplified by excluding the interference of parameters such as solar radiation, infiltration, and outdoor air temperature. By setting the non-target zones on both sides of the target zone, air blowing from the air-conditioning system was spread to the non-target zones on both sides. Therefore, The office has three zones, each extending from east to west with a width of 6000 mm, a depth of 6500 mm, and a ceiling height of 2700 mm. The height was 2600 mm or more based on the architectural design standards of the Ministry of Land, Infrastructure, Transport and Tourism in Japan (Ministry of Land, Infrastructure, Transport and Tourism, Japan, 2020). In addition, the study assumed that desks and partitions were installed as in a typical office and used these as they were. Moreover, desks, an air-conditioning unit, and a ventilation unit were installed in the middle zone, and seven people also occupied the space.

Ventilations are separated with an inlet on the north side and an outlet on the south side. These are operated in all zones, with or without occupants, while the air-conditioning system is operated only in the middle zone. This middle zone is the target area, and the other two are non-target areas on opposite ends. The ceiling-hanging panels and partitions are installed between each zone. The effect of ceiling-hanging panels on air-conditioning efficiency is evaluated during the cooling period. Figure 5 shows the cross-sectional view A-B (north-south center) in Figure 4.

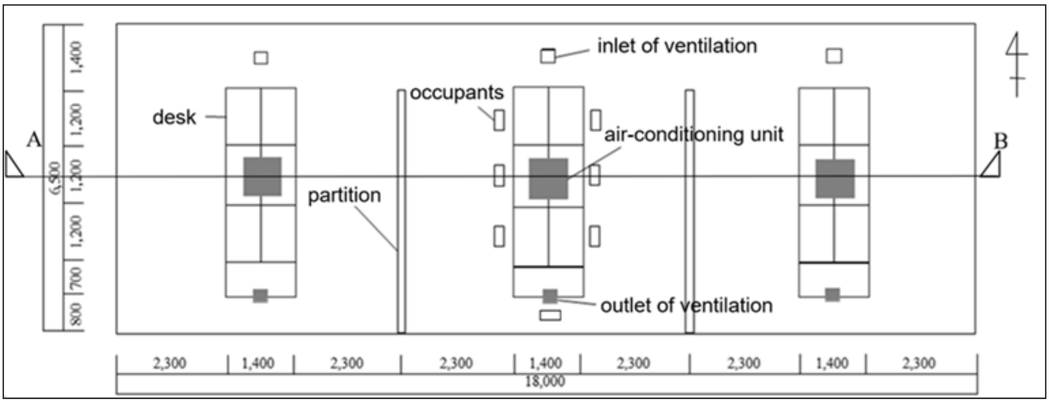

Figure 4. Floor plan of the targeted office. It has three zones, each extending from east to west, with a width of 6000 mm, a depth of 6500 mm, and a ceiling height of 2700 mm

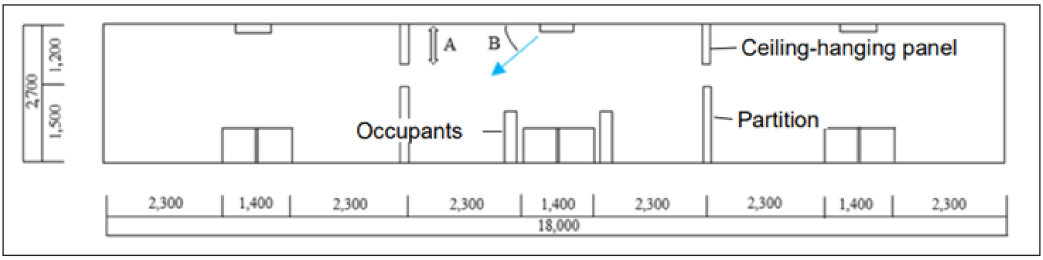

Figure 5. Cross-sectional view A-B (north-south center) in Fig. 4. A represents the ceiling-hanging panel length from the ceiling to the floor, and B is the air-conditioning unit blowout angle from the ceiling

Meanwhile, Figure 6 shows the screen setting of the scFLOW analysis condition. Since the office is symmetrical from east to west, the M face in Figure 6 is set as a mirror surface, and the area from the west wall up to 9000 mm is analyzed to reduce the calculation load. The partition depth from the southern wall is set to 5000 mm to have an aisle width of 1500 mm from the northern wall. In addition, the partition height and thickness are 1500 mm and 50 mm, respectively.

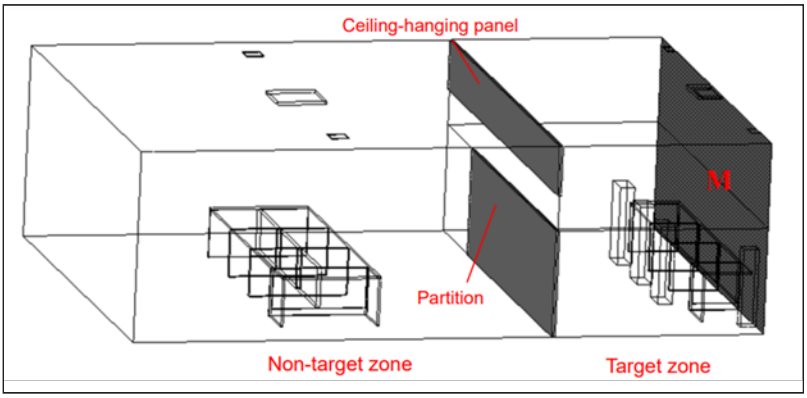

Figure 6. Modeling in CFD. Since the office is symmetrical from east to west, the M face is set as a mirror surface, and the area from the west wall up to 9000 mm is analyzed to reduce the calculation load

Based on Japanese Industrial Standards S 1010, desk dimensions are set to 1200 mm (except for the south desk, which has a width of 1400 mm) and 700 mm for both depth and height. The desk thickness is 30 mm. The boxes that model the occupants are assumed to be sitting; each has a width of 440 mm, a depth of 205 mm, and a height of 1100 mm, with a surface area of 1.6 m² (the average human body surface area of Japanese). Each model is placed 150 mm away from the desk. In Figure 5, A represents the ceiling-hanging panel length from the ceiling to the floor, and B is the air-conditioning unit blowout angle from the ceiling. In the study analysis, A is changed to 350 mm, 700 mm, and 1100 mm, respectively, and B is changed to 15°, 30°, and 45°, respectively.

Table 1 shows the conditions for analysis, such as cooling, ventilation, and internal heat generation. Table 2 shows analysis cases that change the presence or absence of a ceiling-hanging panel or partition, the ceiling-hanging panel length, the air-conditioning unit blowout angle, and the number of blowout directions.

The View Factor method is applied to consider radiation effects in the analysis, and the emissivity is set at 0.95 on all sides in contact with air, except for the flow boundary surface and symmetry surface. Standby power was also considered, wherein equipment and lighting in non-target zones generated 20% of the target zone heat generation amount. On the analysis software, heat generation from equipment such as computers, monitors, and copy machines is set to occur on the desk, while heat caused by lighting occurs throughout the ceiling surface, except for the areas in contact with air-conditioning units, ventilation units, and ceiling-hanging panels. The number of meshes for CFD analysis is approximately 260000. Also, the Realizable k-ε model is adopted as the turbulence model (Japan Construction Equipment Engineers, 2017).

Cooling efficiency is defined as the amount of cold heat flux used to cool the air in the target zone divided by the amount of cold heat flux supplied to the target zone (otherwise known as cooling load). The amount of cold heat flux used to cool the air in the target zone was calculated from the target zone average air temperature derived by CFD analysis.

Table 1
Analysis conditions

Initial Conditions	**Initial Temperature [°C]**		**26**	
Air-Conditioning	Air-conditioning Unit (cooling)	Outlet	Blowout area [mm × mm] × number of blowout directions	700 × 45 × 4
			Air Temperature [°C]	17.26
			Blowout Angle [°]	30
			Mass Flow Rate [kg/s]	0.455868
		Return (Inlet)	Area [mm × mm]	525 × 525
			Mass Flow Rate [kg/s]	0.1823472
	Ventilation Unit	Outlet	Area [mm × mm]	250 × 250
			Air Temperature [°C]	26
			Blowout Angle [°]	90
			Mass Flow Rate [kg/s]	0.0587925
		Exhaust (Inlet)	Area [mm × mm]	250 × 250
			Mass Flow Rate [kg/s]	0.0587925
Internal Heat Generation	Equipment		Target Zone [W]	585
			Non-Target Zone [W]	117
	Lighting		Target Zone [W]	585
			Non-Target Zone [W]	117
	Human [W/person]			53 × 7 persons

Table 2
Analysis case

Case	**Length of Ceiling-Hanging Panels [mm] × : not installed**	**Presence of Partition × : not installed ○ : installed**	**Blowout Angle of Air-conditioning Unit [°]**	**Blowout Direction of Air-conditioning Unit**
0	×	×	30	4
1	×	○	30	4
2	700	×	30	4
3	700	○	30	4
4	350	○	30	4
5	1100	○	30	4
6	700	○	15	4
7	700	○	45	4
8	700	○	30	2

Table 2 shows the analysis parameters for Cases 0 to 8. For Case 3, the basic condition is a 700-mm-long ceiling-hanging panel, a partition installation, a 30° blowout angle, and four blowout directions.

While the cooling efficiency is estimated by the presence or absence of panels from Cases 0 to 2, it is also determined by changing the panel length to 350 mm and 1100 mm in Cases 4 and 5, respectively, by changing the blowout angle to 15° and 45° in Cases 6 and 7, respectively, and by changing the number of blowout directions to 2 in Case 8. The basic length of the ceiling-hanging panels of 700 mm was set on the assumption that furnace accessories of 2000 mm were transported in the analysis target with a ceiling height of 2700 mm. The ceiling-hanging panels extend to 1100 mm until the spacing with the partition of 1500 mm becomes 100 mm.

To increase the cooling effect by utilizing the property of cold air moving downward, the supply air during cooling is generally blowout at an angle smaller than 45° with respect to the ceiling. Accordingly, the basic blowout angle was set to 30°. This angle is changed by 15° and 45°, respectively, assuming the air-conditioning unit blows closer to the ceiling and toward the floor.

Even if the ceiling-hanging panel length is 1100 mm in Case 5, the ceiling-hanging panel length at the aisle is 700 mm. In Case 8, the mass flow rate per outlet is doubled compared to the case where the number of blowout directions is 4. Therefore, if the air is blown in the east and west directions, cold air is expected to flow relatively easily into the non-target zones through the ceiling-hanging panels and partitions due to the high blowout speed. So, the outlet of Case 8 is blown toward the north and south, where there is a wall.

RESULTS AND DISCUSSIONS

Figures 7 and 8, respectively, show the air temperature and airflow distribution of Case 0 at cross-section A-B in Figure 4. The conditions in Case 0 are as follows: the ceiling-hanging panels and partitions are not installed. Also, the air-conditioning unit blowout angle is 30°. In addition, the number of blowout directions for cooling is 4. As a result of

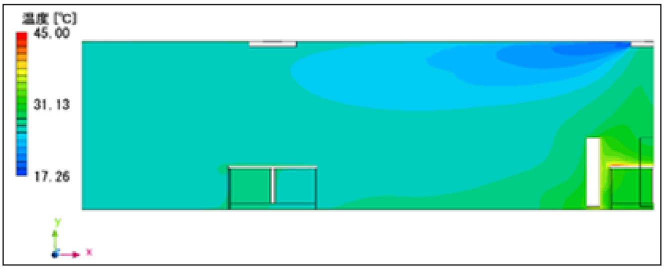

Figure 7. Air temperature of Case 0. The target zone's average air temperature was 27.5°C, while the average air temperature in the non-target zones was 26.7°C

the calculation, the target zone's average air temperature was 27.5°C, while the average air temperature in the non-target zones was 26.7°C. Meanwhile, the air-conditioning unit's cooling efficiency was 82.8%. Due to the Coanda effect (Miozzi et al., 2010), the air flowed slightly along the ceiling surface even though the blowout angle was 30°. In Case 0, without the ceiling-hanging panels and partitions, cold air from the air-conditioning unit leaked into the non-target zones relatively easily, lowering the air temperature of the non-target zones to that of the target zone.

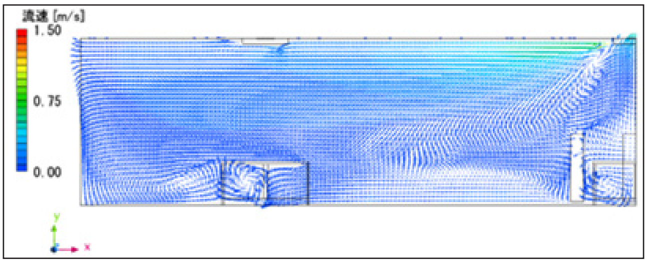

Figure 8. Airflow of Case 0. Cold air from the air-conditioning unit leaked into the non-target zones relatively easily

Figures 9 and 10 are the results of the Case 1 condition, in which only partitions were installed under the Case 0 condition. The height of the partitions was 1500 mm. Meanwhile, the average air temperature in the target and non-target zones were 27.7°C and 27.0°C, respectively, while the cooling efficiency was 80.5%. Similar to Case 0, the Case 1 air temperature in the non-target zones was lower than that of the target zone. In addition, the average air temperature of the two zones in Case 1 was higher than that of Case 0. This is because cold air blown from the air-conditioning unit was taken back into the air-conditioning unit without processing the target zone cooling load. The installation of partitions made it difficult for the cold air leaking into the non-target zones to return to the target zone. Also, air processed with the load in non-target zones flowed into the target zone through the north aisle. As a result, the target zone's average air temperature was higher than the non-target zones.

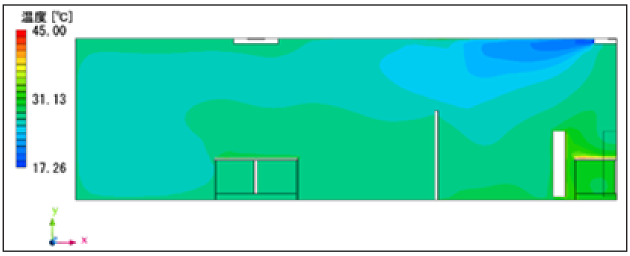

Figure 9. Air temperature of Case 1. The target zone's average air temperature was 27.7°C, while the average air temperature in the non-target zones was 27.0°C, respectively

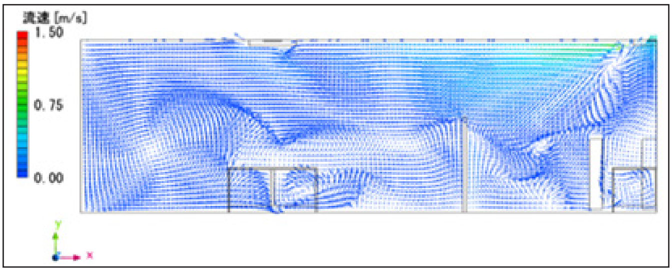

Figure 10. Airflow of Case 1. The installation of partitions made it difficult for the cold air leaking into the non-target zones to return to the target zone

Figures 11 and 12, respectively, show the air temperature and airflow distribution of Case 2, in which the panel was installed under Case 0 conditions. The ceiling-hanging panel length was 700 mm. Also, the target zone's average air temperature was 26.9°C, the average air temperature in the non-target zones was 27.4°C, and the cooling efficiency was 89.7%. In Case 2, the target zone's average air temperature was lower, and the average air temperature of the non-target zones was higher than in Case 0. This result indicates the effect of the ceiling-hanging panel on cooling. It can be concluded that most of the cold energy from the air-conditioning unit is used to cool the target zone, wherein installing ceiling-hanging panels increases the air-conditioning unit's cooling efficiency.

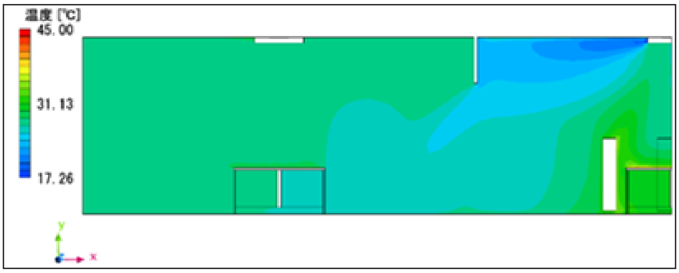

Figure 11. Air temperature of Case 2. The target zone's average air temperature was 26.9°C, while the average air temperature in the non-target zones was 27.4°C

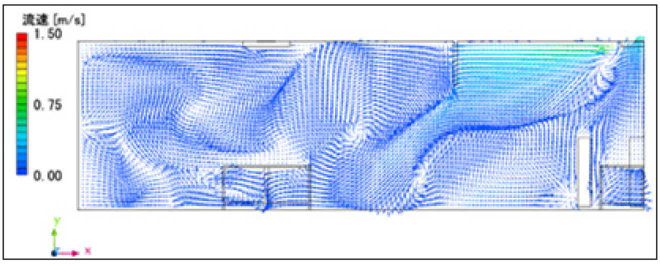

Figure 12. Airflow of Case 2. Some of the airflow on the floor forms a vortex and returns to the target zone

Figures 13 and 14 show the results of Case 3, which is the basic condition. In this case, both ceiling-hanging panels with a length of 700 mm and partitions with a height of 1500 mm were installed, the air-conditioning unit blowout angle was 30°, and the number of blowout directions was 4. The target zone's average air temperature was 27.4°C, the average air temperature in the non-target zones was 27.6°C, and the cooling efficiency was 84.0%. In Case 3, the target zone average air temperature was higher than in Case 2, in which only ceiling-hanging panels were installed. As shown in the air flow distribution of the two cases (Figures 12 and 14), the discharged air flow from the air-conditioning unit goes to the floor of the non-target zones after meeting the panel. Without a partition in Case 2, some of the airflow on the floor forms a vortex and returns to the target zone. However, in Case 3, airflow is blocked by the partition, preventing its return to the target zone. Most of the cold air leaking into the non-target zones returns to the target zone through the north aisle after obtaining heat in the non-target zones, resulting in a higher target zone temperature than in Case 2. From the average target zone air temperature results, it can be concluded that installing only ceiling-hanging panels is more advantageous for cooling than installing both ceiling-hanging panels and partitions.

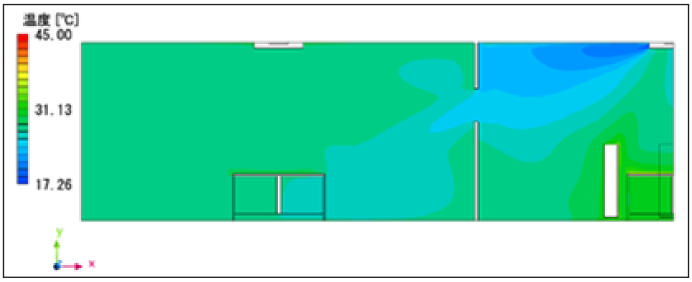

Figure 13. Air temperature of Case 3. The target zone's average air temperature was 27.4°C, while the average air temperature in the non-target zones was 27.6°C, respectively

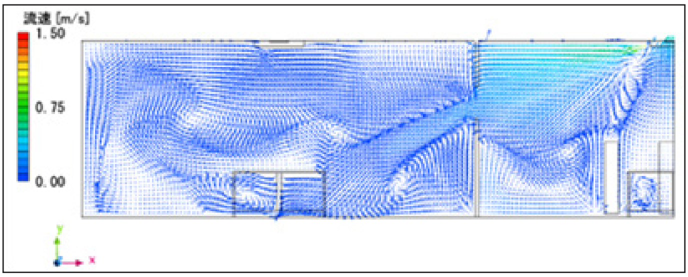

Figure 14. Airflow of Case 3. Airflow is blocked by the partition, preventing its return to the target zone

The cooling efficiency can also confirm this. Figure 27 compares the air conditioning unit's cooling efficiencies in Cases 0–3. Comparing Cases 0 and 1 as well as Cases 2 and

3, the results indicate that installing partitions reduces the air conditioning unit's cooling efficiency and that cooling efficiency is highest when only ceiling-hanging panels are installed.

Figures 15 and 16 show the calculation results of the Case 4 conditions in which the ceiling-hanging panel length was shortened from 700 mm to 350 mm under basic conditions (Case 3). Also, the average target zone air temperature was 27.9°C, the average air temperature in the non-target zones was 27.4°C, and the cooling efficiency was 78.2%. In Case 4, shorter than the 700 mm panels under basic conditions, it was determined that a large amount of cold air leaked into the non-target zones, resulting in a higher average air temperature in the target zone than in Case 3.

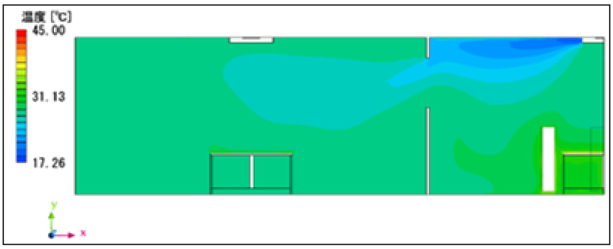

Figure 15. Air temperature of Case 4. The target zone's average air temperature was 27.9°C, while the average air temperature in the non-target zones was 27.4°C, respectively

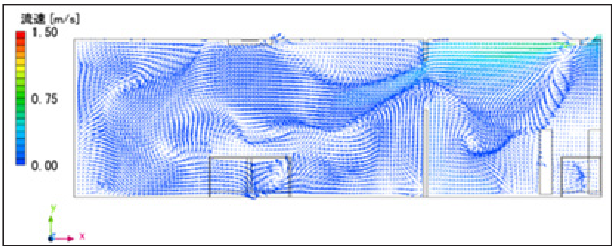

Figure 16. Airflow of Case 4. A large amount of cold air leaked into the non-target zones compared to case 3

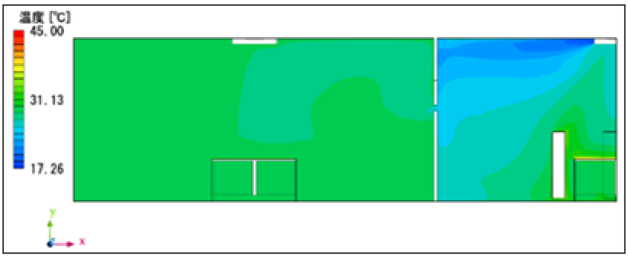

Figure 17. Air temperature of Case 5. The target zone's average air temperature was 26.7°C, while the average air temperature in the non-target zones was 28.5°C, respectively

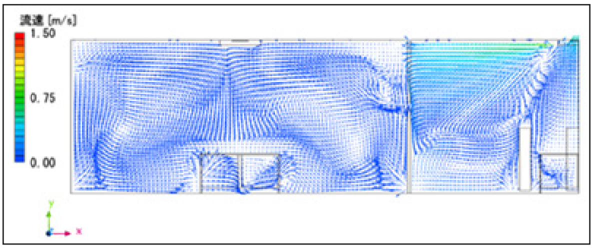

Figure 18. Airflow of Case 5. Most of the cold air did not leak into the non-target zones and, therefore, more efficiently cooled the target zone

Figures 17 and 18 show the calculation results of the Case 5 conditions in which the ceiling-hanging panel length was increased from 700 mm to 1100 mm under basic conditions (Case 3). The target zone's average air temperature was 26.7°C, the average air temperature in the non-target zones was 28.5°C, and the cooling efficiency was 92.0%. In Case 5, it was confirmed that most of the cold air did not leak into the non-target zones and, therefore, more efficiently cooled the target zone.

It can be concluded from Figure 28 that the longer the panels, the better the cooling efficiency.

Figures 19 and 20, respectively, show the air temperature and airflow distribution of the Case 6 conditions in which the air conditioner blowout angle is changed from 30° to 15° under the basic condition (Case 3). Therefore, ceiling-hanging panels with a length of 700 mm and partitions with a height of 1500 mm were installed. The number of blowout directions was 4. The target zone's average air temperature was 27.2°C, the average air temperature in the non-target zones was 28.2°C, and the cooling efficiency was 86.2%. In Case 6, air flow discharged from the air-conditioning unit meets the panel at a faster velocity so that a greater amount of cold air reaches the floor. In addition, since the downward pressing force is active, it becomes difficult for cold air to leak into the non-target zones. As a result, the target zone's average air temperature is lower, while the average air temperature in the non-target zones is higher than in Case 3.

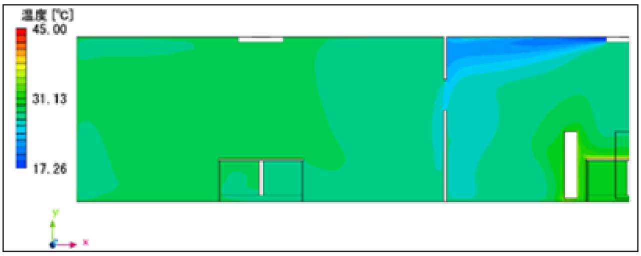

Figure 19. Air temperature of Case 6. The target zone's average air temperature was 27.2°C, while the average air temperature in the non-target zones was 28.2°C, respectively

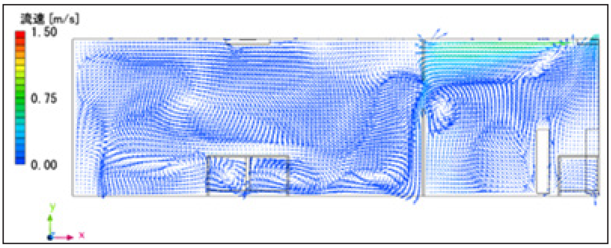

Figure 20. Airflow of Case 6. Since the downward pressing force is active, it becomes difficult for cold air to leak into the non-target zones

Figures 21 and 22 show the calculation results of the Case 7 conditions in which the blowout angle of the air-conditioning unit is changed from 30° to 45° under the basic condition (Case 3). The target zone's average air temperature was 28.6°C, the average air temperature in the non-target zones was 29.2°C, and the cooling efficiency was 70.2%. In Case 7, from the air temperature distribution (Figure 21), airflow distribution (Figure 22), and average air temperature of each zone, the discharged air from the air-conditioning unit is not diffused into the target zone. It is still taken back into the air-conditioning unit without processing the target zone cooling load, so the cooling efficiency is lowest among all cases.

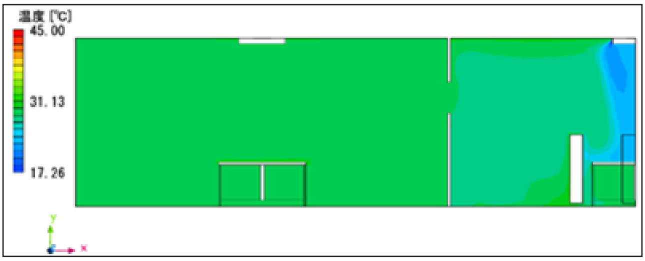

Figure 21. Air temperature of Case 7. The target zone's average air temperature was 28.6°C, while the average air temperature in the non-target zones was 29.2°C, respectively

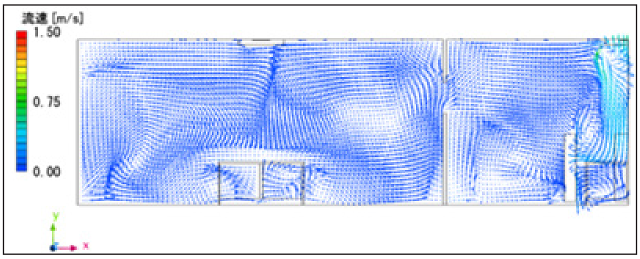

Figure 22. Airflow of Case 7. The discharged air from the air-conditioning unit is not diffused into the target zone

Figure 29 compares the cooling efficiency of the air conditioning unit when the blowout angle is changed in Case 3 (30°), Case 6 (15°), and Case 7 (45°). It was confirmed that the closer the blowout angle is to the ceiling, the higher the cooling efficiency.

Figures 23–26 show the results of Case 8. In Case 8, cold air is blown in two directions of the south and north walls, while the mass air flow rate per outlet is doubled compared to the basic condition. Other conditions, such as the installation of panels and partitions as well as a 30° blowout angle, are the same as the basic condition (Case 3). Figures 23 and 24 are the northern aisle results compared to the calculation results in cross-section A (Figure 4), which is the floor plane center. Therefore, cross-section A-B is 3250 mm away from the northern wall, while the cross-sections of Figures 23 and 24 are 300 mm away from the north wall. Figures 25 and 26, respectively, show the air temperature and airflow distribution of the cross-section A-B in the floor plane center.

The target zone's average air temperature was 27.1℃, the average air temperature in the non-target zones was 27.2℃, and the cooling efficiency was 87.3%. In Case 3, since the blowout angle was set to 30° and the number of blowout directions was 4, cold air easily leaked to the non-target zones through the gap between the ceiling-hanging panels and partitions. On the other hand, in Case 8, the air-conditioning unit blows cold air only toward the walls while the mass flow rate per outlet doubles so that cold air tends to remain in the target zone. Figure 26 shows that cold air flows from the north aisle into the non-target zones while air flows into the target zone through a gap between the ceiling-hanging panels and partitions.

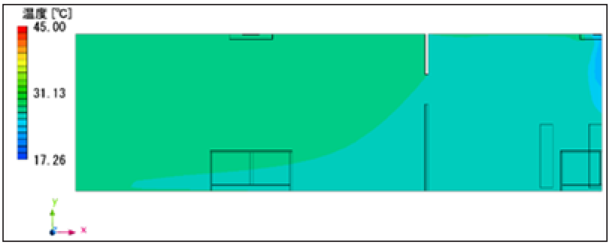

Figure 23. Air temperature of Case 8 at 300 mm from the north wall. Cold air is blown in two directions of the south and north walls

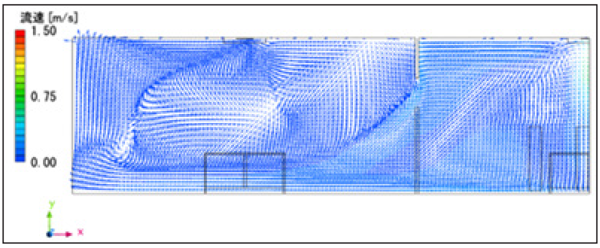

Figure 24. Airflow of Case 8 at 300 mm from the north wall. Cold air tends to remain in the target zone

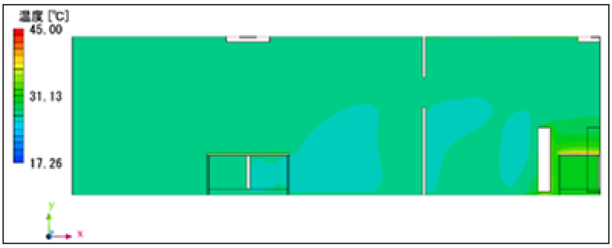

Figure 25. Air temperature of Case 8. The target zone's average air temperature was 27.1°C, while the average in non-target zones was 27.2°C

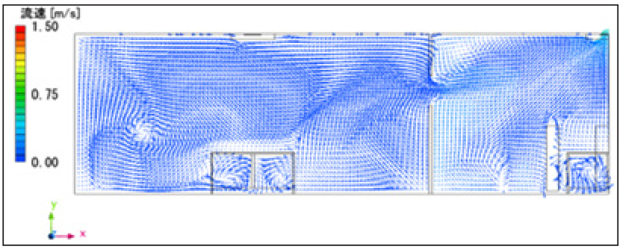

Figure 26. Airflow of Case 8. Air flows into the target zone through a gap between the ceiling-hanging panels and partitions

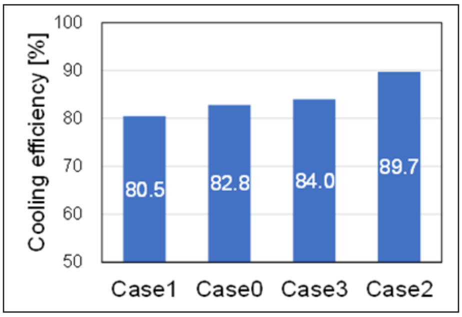

Figure 27. Cooling efficiency of Cases 0~3. The results indicate that cooling efficiency is highest when only ceiling-hanging panels are installed

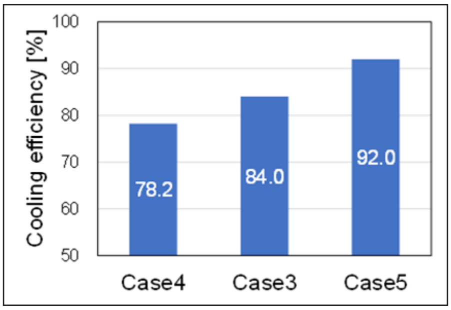

Figure 28. Cooling efficiency of Cases 3, 4, and 5. The longer the panel, the better the cooling efficiency

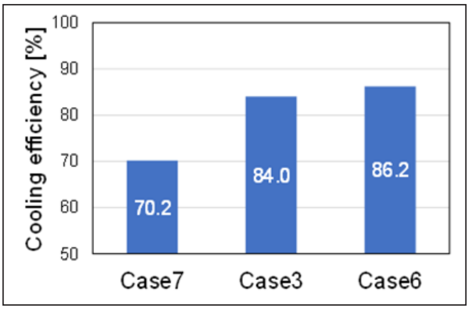

Figure 29. Cooling efficiency of Cases 3, 6, and 7. The closer the air-conditioning unit blowout angle is to the ceiling, the higher the cooling efficiency

Figure 30 shows cooling efficiency when the number of blowout directions is changed. A blowout in two directions, south and north, is more advantageous than in four directions

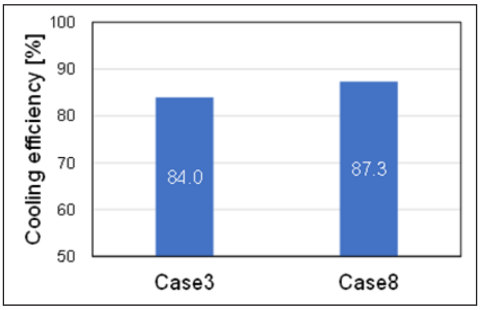

Figure 30. Cooling efficiency of Cases 3 and 8. It is more advantageous to blowout in 2 directions, the south and north, than in 4

CONCLUSION

This study reviewed a more efficient air-conditioning method when different air-conditioning loads occur in a single space that is not separated by walls in an office building. Considering that indoor air temperature is formed by airflow from air-conditioning units and ventilation units, installing panels on the ceiling to trap air flow from air-conditioning units where cooling is needed was proposed. In addition, by CFD analysis, the impact of the ceiling-hanging panels on cooling efficiency was analyzed by varying the presence or absence of ceiling-hang panels and partitions, the length of the ceiling-hanging panels, the blowout angle, and the number of blowing directions from the air-conditioning unit. The conclusions drawn from the analysis results are as follows:

1. In Cases 0–3, the effect of installing ceiling-hanging panels or partitions on cooling efficiency was evaluated. Analyses were conducted for Case 0, in which both ceiling-hanging panels and partitions were not installed; Case 1, in which only partitions

were installed; Case 2, in which only panels were installed; and Case 3, in which both ceiling-hanging panels and partitions were installed. Cooling efficiency was highest in Case 2 and the lowest in Case 1. Therefore, cooling efficiency can be expected just by installing a ceiling panel.

2. In Cases 3, 4, and 5, cooling efficiency was determined by changing the length of the ceiling-hanging panels to 350 mm, 700 mm, and 1100 mm, respectively. Cooling efficiency was the lowest for Case 4, which has 350 mm ceiling-hanging panels and the highest for Case 5, which has 1100 mm ceiling-hanging panels. Therefore, the longer the ceiling-hanging panels, the better the cooling efficiency.
3. In Cases 6 and 7, the effect of the air-conditioning unit blowout angle on cooling efficiency was investigated. The outlet angle was changed from 30° to 15° in Case 6 to 45° in Case 7. Cooling efficiency was highest in Case 6 and the lowest in Case 7. Therefore, as the blowout angle of the air-conditioning unit decreases, cooling efficiency increases.
4. In Case 8, it was confirmed whether the cold air from the air-conditioning unit could be reduced by blowing to the north and south walls except for the direction in which the panels and partitions were located. The cooling efficiency of Case 8 improved compared to Case 3, in which the number of blowout directions was 4.

Future studies may evaluate the ceiling-hanging panel performance based on the location and number of air-conditioning and ventilation units while considering the furniture layout, such as desks and bookshelves. In addition, as this study only focused on a small office with three zones, an investigation into interference between air-conditioning units should be conducted for larger offices.

ACKNOWLEDGEMENT

The authors thank the Korea Institute of Energy Research for providing technical data on building equipment and BEL Technology Co. Ltd. for technical assistance with the numerical simulation.

REFERENCES

De dear, R. J., & Brager, G. S. (1998). Developing an adaptive model of thermal comfort and preference/discussion. *ASHRAE Transactions,* 104(1), Article 145.

Lipczynska, A., Stefano, S., & Lindsay, G. T. (2018). Thermal comfort and self-reported productivity in an office with ceiling fans in the tropics. *Building and Environment*, *135*, 202–212. https://doi.org/10.1016/j.buildenv.2018.03.013

Ministry of Land, Infrastructure, Transport and Tourism, Japan (2020) *Architectural design standards 8.* Ministry of Land, Infrastructure, Transport and Tourism, Japan. https://www.mlit.go.jp/common/001473336.pdf .

Miozzi, M., Lalli, F., & Romano, G. P. (2010). Experimental investigation of a free-surface turbulent jet with coanda effect. *Experiments in Fluids, 49*, 341–353. https://doi.org/10.1007/s00348-010-0885-1

Miwa, S., Watanabe, S., Hirai, T., & Matsumoto, T. (2014). Air conditioner controlling temperatures we feel. *Journal of the Robotics Society of Japan, 32*(3), 218–221. https://doi.org/10.7210/jrsj.32.218

Mizuide, K., Ishino, H., Kohri, K., Nagata, A., Ngiao, T., Otaka, K., & Oohara, K. (2007). Design method and performance verification about air conditioning system with ceiling fans: A study on performance evaluation and control method design about a hybrid air conditioning system with a combination of natural ventilation and ceiling fans part 2 (in Japanese). *Journal of Environmental Engineering (Transactions of AIJ), 72*(620), 59–66. https://doi.org/10.3130/aije.72.59_5

Murakami, S., & Kato, S. (1986). New scales for ventilation efficiency and calculation method by means of 3-dimensional numerical simulation for turbulent flow - Study on evaluation of ventilation efficiency in room. *Transactions of the Society of Heating, Air-Conditioning Sanitary Engineers of Japan*, *32*, 91–101.

Nishimura, T., Chikamoto, T., & Ninomiya, K. (2006). Study on the energy performance for every rooms and every loads in architectural space (Part2) methods and study on the cooling load and contro1 strategy in office zone. *Proceedings of the Society of Heating, Air-Conditioning Sanitary Engineers of Japan, D-54,* 1845–1848. https://doi.org/10.18948/shasetaikai.2006.3.0_1845

Japan Construction Equipment Engineers. (2017). *Guidebook of Computational Fluid Dynamics.* Ohmsha Publisher.

Sudo, M., Murakami, S., Kato, S., Song, D., & Chikamoto, T. (2004). Study on the personal air-conditioning system considering human thermal adaptation part1- Evaluation of conventional personal AC system by subjective experiment. *Transactions of the Society of Heating, Air-Conditioning Sanitary Engineers of Japan*, *29*(95), 53–60. https://doi.org/10.18948/shase.29.95_53

Pertanika J. Sci. & Technol. 33 (S2): 73 - 84 (2025)

SCIENCE & TECHNOLOGY

Journal homepage: http://www.pertanika.upm.edu.my/

Dynamic Hand Gesture Recognition by Hand Landmark Classification Using Long Short-Term Memory

Khawaritzmi Abdallah Ahmad[1]*, Takahiro Higashi[2] and Kaori Yoshida[2]

[1]*Department of Information Systems, Hasanuddin University, Jl. Perintis Kemerdekaan No.KM.10, Tamalanrea Indah, Kec. Tamalanrea, Kota Makassar, Sulawesi Selatan 90245 Indonesia*
[1, 2]*Graduate School of Life Science and Systems Engineering Kyushu Institute of Technology, 2-4, Hibikino, Wakamatsu, Kitakyushu City, Fukuoka 808-0196 Japan*

ABSTRACT

Hand gestures are a valuable modality for human-computer interaction, conveying information that can be used as input. Dynamic hand gestures, prevalent in real-world scenarios, necessitate considering temporal factors such as gesture initiation, termination, and frame sequence. A Long Short-Term Memory (LSTM) based recognition model was proposed to address this challenge. Data availability for dynamic hand gesture research is a significant hurdle. The dataset introduced by Fronteddu et al. provides 27 classes of dynamic hand gestures, serving as a suitable training resource. MediaPipe Hands, a computer vision framework, was leveraged to extract keypoints from each frame, capturing spatial features fed into the LSTM model. Experiments were conducted to determine the optimal dropout rate for the LSTM model. Results indicated that a dropout rate of 70% yielded the highest accuracy, achieving up to 98.53% validation accuracy and 99.71% test accuracy. These findings demonstrate the effectiveness of the proposed LSTM-based recognition model for dynamic hand gestures. Future research could explore integrating other deep learning techniques, such as attention mechanisms, to enhance the accuracy and robustness of dynamic hand gesture recognition systems. Additionally, investigating the application of the proposed model in real-world scenarios, such as virtual and augmented reality, would be valuable in assessing its practical utility.

Keywords: Classification, dynamic hand gesture, human-computer interaction, long short-term memory

INTRODUCTION

The advancement of technology has elevated computer vision to a pivotal role in human-computer interaction, serving as a bridge between humans and machines. The increasing sophistication of computers has empowered them to augment human capabilities, streamlining various tasks.

ARTICLE INFO

Article history:
Received: 13 February 2023
Accepted: 18 October 2024
Published: 25 February 2025

DOI: https://doi.org/10.47836/pjst.33.S2.05

E-mail addresses:
khawaritzmi@gmail.com (Khawaritzmi Abdallah Ahmad)
higashi.takahiro231@mail.kyutech.jp (Takahiro Higashi)
kaori@brain.kyutech.ac.jp (Kaori Yoshida)
*Corresponding author

ISSN: 0128-7680
e-ISSN: 2231-8526

Consequently, human-computer interaction has become an inseparable part of human life (Sharma & Verma, 2015). Fang et al. (2007) stated that traditionally, humans use tools such as keyboards, mice, and joysticks as media to interact with computers, which is unnatural. Natural interaction can be done with speech, body movements, handwriting, and vision interfaces and is referred to as Natural User Interface (NUI) (Camargo et al., 2021). NUI is an emerging computer interaction methodology focusing on human abilities such as touch, vision, voice, motion and higher cognitive functions such as expression, perception, and recall (Camargo et al., 2021). Hand gestures are one of the many human modalities used in human-computer interaction and contain information that can be used as input for natural human-computer interaction (Hakim et al., 2019).

There are two kinds of hand gestures: static and dynamic. A single frame or spatial dimension characterizes static hand gestures. In contrast, dynamic hand gestures encompass multiple layers of temporal information, making them more prevalent in real-world applications. To effectively recognize dynamic hand gestures, it is imperative to employ methods capable of simultaneously processing both spatial and temporal features. To create and research dynamic hand gesture recognition models, researchers also face problems with the availability of suitable data for experiments. The dataset for dynamic hand gesture recognition systems provided by Fronteddu et al. (2022) proposes a dataset of 27 dynamic hand gesture types acquired at full HD resolution from 21 subjects (Fronteddu et al., 2022). Each subject performed 27 hand gestures three times for 1,701 videos, which is the proper dataset to be a sample to train a recognition model (Fronteddu et al., 2022). A hand landmark classification method was implemented using the MediaPipe Hands framework in this study. The hand landmark classification method is a classification method that uses 21 hand landmark keypoints produced by MediaPipe Hands at x, y, and z coordinates, which are used as features that are then used in the training process using machine learning or deep learning algorithms. The hand landmark classification method allows for easy determination and adjustment of the recognized class of hand gestures for a specific purpose. This method has worked very well on static hand gesture datasets using artificial neural networks (ANN) and support vector machines (SVM) (Ahmad et al., 2022, 2023). However, for the dynamic hand gesture dataset, the resulting features must be connected and interdependent inputs on certain frames, so a more complex architecture is needed to handle sequence data. For that, a long short-term memory (LSTM) model will be used to handle the temporal features of the dynamic hand gesture dataset.

Another problem faced when training a machine learning model with multiclass classification tasks is overfitting, where the model has the ability to classify different classes in the training data but is not good when given test data. Therefore, one way is to apply the dropout method to the architecture (Srivastava et al., 2014). Five different models were utilized in this study, each with a different dropout rate: 50%, 60%, 70%, 80%, and 90%. The performance results using LSTM can achieve a validation accuracy of 96.77% and an accuracy of 100.00% in 200 epochs. This method works very well on dynamic hand gesture datasets. The model's good performance could be a reference for its integration into industrial machinery, mining equipment, and healthcare devices. It would allow users to interact with the systems more intuitively and efficiently, especially when touching traditional input devices like keyboards or mice is impractical or hazardous.

MATERIALS AND METHODS

This methodology uses the dataset to train an LSTM-based model for hand gesture recognition. Keypoints representing hand movements are extracted using the Mediapipe Hands model, followed by data preprocessing and splitting. The LSTM model is trained with various dropouts to improve generalization, and its performance is evaluated and visualized, completing the gesture recognition pipeline, as shown in Figure 1.

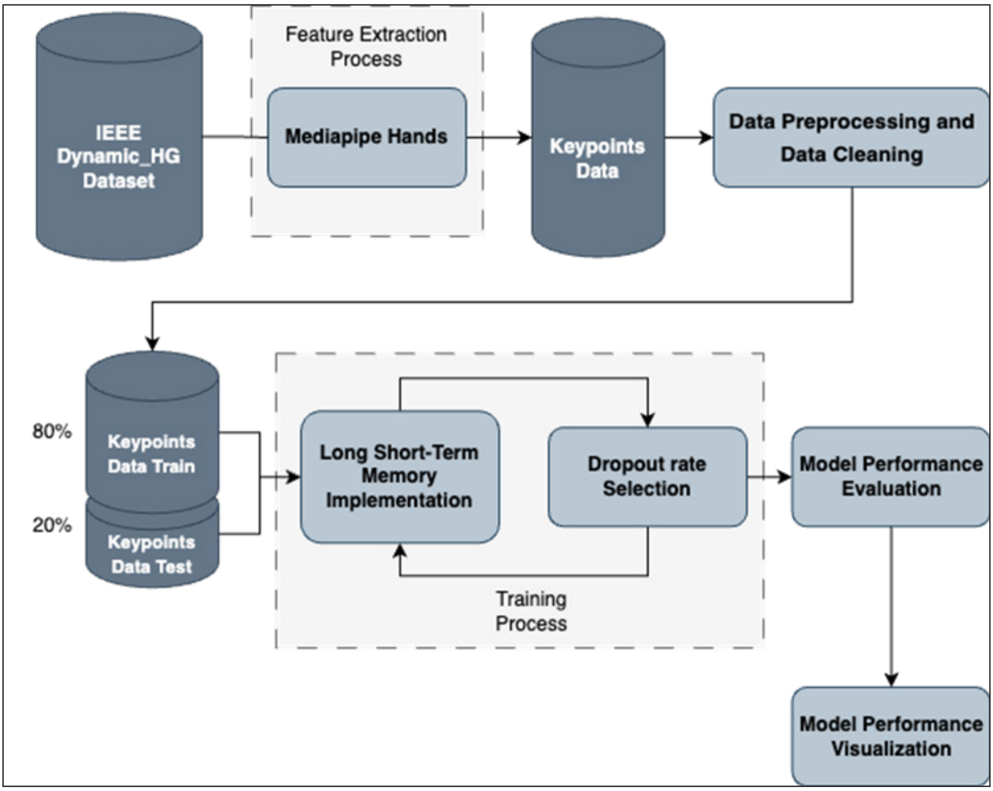

Figure 1. Method implementation flowchart

Mediapipe Hands

MediaPipe Hands is a framework used in this study to extract spatial features from hand gestures. Google LLC developed MediaPipe Hands, a framework that can be used to track and produce hand landmarks in the form of key points that indicate 21 connecting points on the finger and palm, as shown in Figure 2. (Zhang et al., 2020). The MediaPipe Hands framework detects palms by training on three types of datasets with over 116,000 samples. These are 6000 samples from the In-the-wild dataset, 10,000 In-house collected dataset, and 100,000 samples from synthetic hand gestures (Zhang et al., 2020). A *z* value that points to the wrist depth value represents the relative depth of landmarks, and all *x, y*, and *z* data are normalized to [0.0, 1.0] (Zhang et al., 2020).

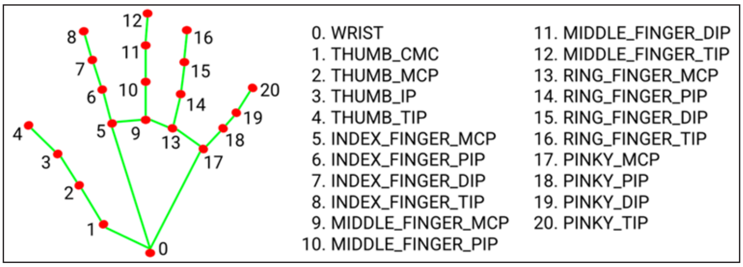

Figure 2. Mediapipe Hands keypoints (Zhang et al., 2020). 21 Keypoints represent human bone joints

Dataset

The dataset used in this research is the dataset provided by Fronteddu et al. (2022). This dataset was created by recording the subject's hand movements from the front using a camera with a full HD image resolution of 1080p (1,920*1,080 pixels) (Fronteddu et al., 2022). There were 21 subjects who demonstrated 27 classes of dynamic hand gestures labeled class_01 to class_27, as shown in Figure 3, where each subject was monitored very carefully in demonstrating hand gestures by the author to produce hand gestures consistent

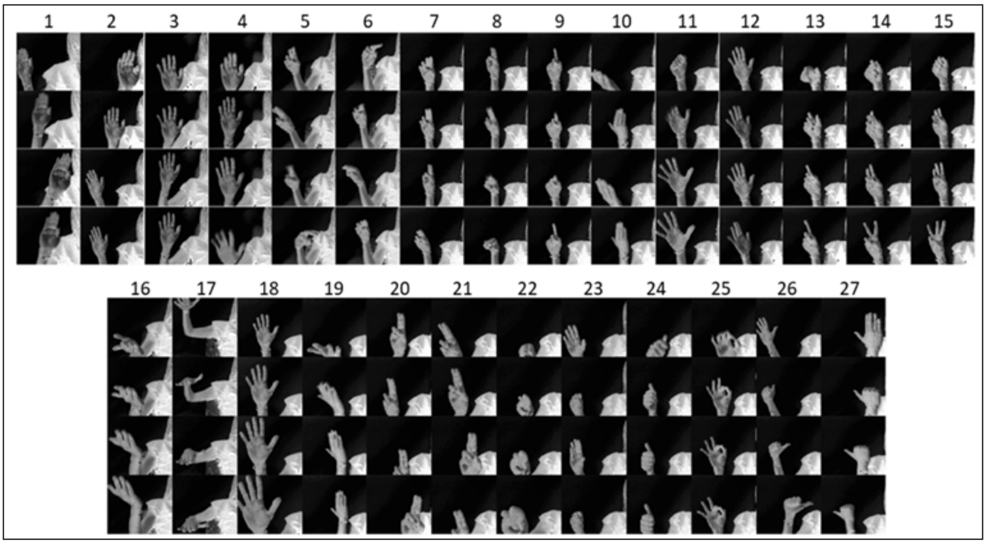

Figure 3. A representative of each 27 class on the dataset for dynamic hand gesture recognition systems (Fronteddu et al., 2022). The gesture frame comes from top to bottom

with those instructed (Fronteddu et al., 2022). Each subject made 27 hand gestures three times, with 1,701 videos and 204,120 corresponding video frames. The overall dataset video file size is 21.34 GB, with the video format being (.avi) (Fronteddu et al., 2022).

Preprocessing

Before entering the model training process, the data resulting from feature extraction enters the preprocessing process. In this process, the data has 120 frames and will produce features for each sample with dimensions of 120 rows and 63 columns. The preprocessing is to match the duration of the hand gesture made by the subject to each video sample provided in the metadata. In the metadata, two variables are provided, namely *start_frame,* which represents the frame at which the hand gesture starts to be counted as the desired hand gesture in the video.

The second variable is *end_frame*, which shows which frame the hand gesture ends at. After adjusting the duration of the hand gesture with the metadata provided, normalization is carried out on the feature vector. For each frame that occurs outside of the hand gesture's initial and final times, the entire value of the feature vector in that frame is converted to a "0" value so that all feature dimensions for each sample remain 120 rows. The preprocessing process result is visualized in Figure 4.

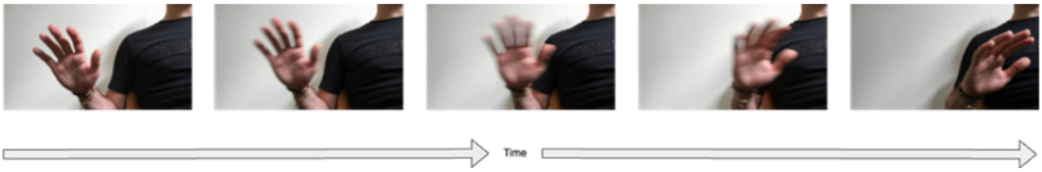

(a) Video dataset example from sample user1_1 on class_1 (Fronteddu et al., 2022)

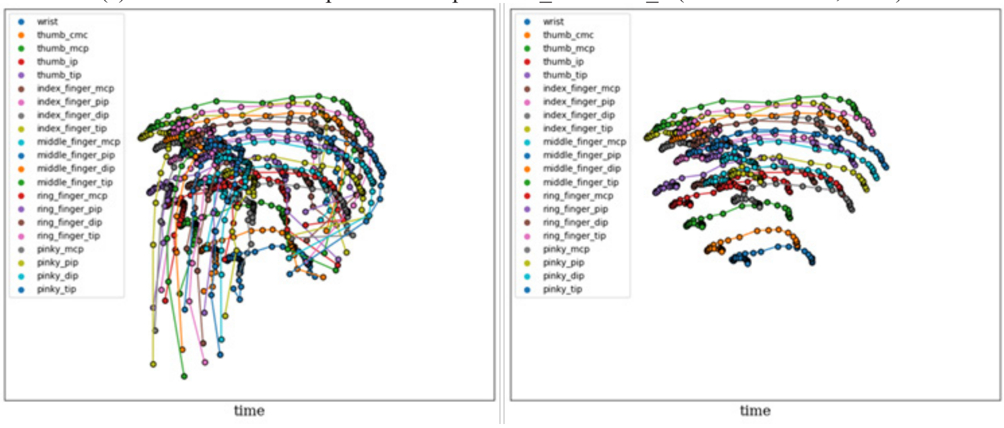

(b) Keypoints tracking visualization before cleaning (left) and after cleaning (right) from sample user1_1 on class_1

Figure 4. The preparation approach involves cleaning the data, converting hand gestures from video to keypoints using Mediapipe Hands, and then fitting the hand gesture duration using metadata given by the dataset creators

Long Short-Term Memory (LSTM)

The LSTM is a recurrent neural network (RNN) commonly used for sequence modeling and analysis (Hochreiter & Schmidhuber, 1997). The LSTM model extracts temporal features from keypoint data generated from the preprocessing step. LSTM networks are crucial in deploying dynamic hand gesture recognition systems because they effectively capture temporal dependencies in sequential data. Unlike traditional models, LSTMs are designed to remember information for long periods, making them particularly suited for interpreting the continuous nature of gestures, which can vary in speed and duration.

The LSTM networks have been demonstrated to be highly effective in handling temporal features, particularly in real-time gesture recognition applications. By combining 3D Convolutional Neural Networks (3D CNNs) with LSTMs, spatial and temporal features can be extracted from video sequences, leading to significant improvements in accuracy. Studies have shown that this approach can achieve accuracy rates as high as 99% (Rehman et al., 2021; Hakim et al., 2019). With the advancement of LSTM, MediaPipe Hands is utilized to investigate the impact of skeleton-based spatial features combined with LSTM for handling temporal features in a dynamic hand gesture dataset. The aim is to develop a robust gesture recognition system that can effectively operate in dynamic environments and real-world scenarios.

Model Design, Training, and Evaluation

The dataset is represented by 120 rows representing the number of frames from one sample, 30 frames per second, with a duration of 4 seconds per sample, and 63 columns representing the dimensions of the spatial feature, which is initially 21*3 from $\vec{x} \in \mathbb{R}^{21}$, $\vec{y} \in \mathbb{R}^{21}$ and $\vec{z} \in \mathbb{R}^{21}$ and then arranged using the flattening method to become , resulting in the dataset $S = \{(\mathcal{X}_i \in \mathbb{R}^{120*21*3}, \mathcal{Y}_i \in \mathbb{R}^{27})\}_{i=1}^{n=1701}$ as shown in Figure 5. The training model employs an LSTM layer with 256 units of LSTM cells with dropout rates of 50%, 60%, 70%, 80%, and 90%. The *softmax* activation function is used in the classification stage. The total number of parameters in the model is 334,619.

The model is then constructed using loss function: categorical cross entropy and Adaptive Moment Estimation (Adam) optimizer before beginning the training phase, as shown in Table 1. The training procedure employs 200 epochs, 32 *batch_size*, and 0.1 *learning_rate*. The dataset is separated into 80% for the training process and 20% for testing data utilized in the validation step before beginning the training process. A portion of 80% is considered sufficient to train a model, with the data for each training session for each class being 50–51 samples and for training data being 12–13 samples.

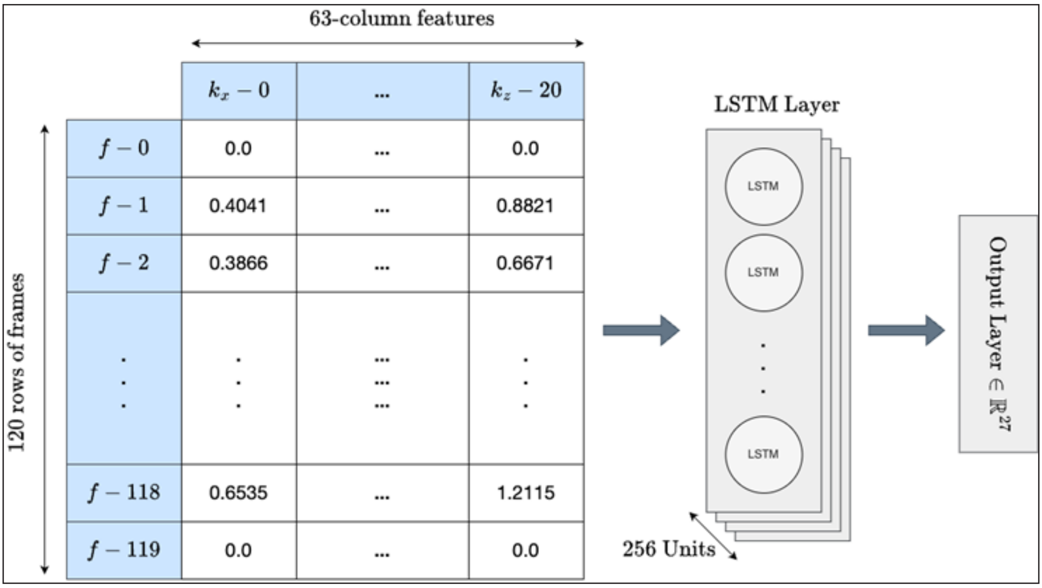

Figure 5. Model architecture using LSTM. Model input is the keypoints coordinate flattened in 1 row each frame for every sample

Table 1
Model Hyperparameters

Training Parameters	Proposed Value
Learning Rate	0.1
Batch Size	32
Epoch	200
Shuffle	False
Optimizer	Adam
Loss Function	Categorical Crossentropy
Activation Function	Softmax
Dropouts	50%, 60%, 70%, 80%, 90%
Total Parameters	334,619

Performance Evaluation Method

This study employs a multiclass classification methodology appropriate for datasets with more than two distinct categories. Given the dataset's 27 classes, it is well-suited for this approach. The model's performance after training was evaluated using standard metrics: accuracy, precision, recall, F1-score, and loss. Accuracy is the ratio of correct predictions to all predictions, independent of class (Equation 3). In contrast, the F1-score (Equation 4) is the harmonic average of the model's precision and recall, where precision (Equation 1) is the proportion of how many relevant items are predicted and recall (Equation 2) is the ratio of how many relevant items are predicted. The variable values for precision, recall, accuracy, and F1-score can be derived from the confusion matrix in Table 2.

$$Precision_a = \frac{TP_a}{TP_a + \sum_X F_{a|X}} \qquad [1]$$

$$Recall_a = \frac{TP_a}{TP_a + \sum_X F_{X|a}} \qquad [2]$$

$$Accuracy = \frac{\sum_a TP_a}{\sum_a TP_a + \sum_a F_{X|a} + \sum_a F_{a|X}} = \frac{\sum_a TP_a}{N} \qquad [3]$$

$$F1 - Score = 2 \cdot \frac{precision \cdot recall}{precision + recall} \qquad [4]$$

$$Categorical\ CE\ loss = -log\left(\frac{e^{s_i}}{\sum_j^C e^{s_i}}\right) \qquad [5]$$

Table 2
Multiclassification confusion matrix

		PREDICTED Class		
	Classes	***a***	***b***	***c***
Actual Class	*a*	TP_a	$F_{b\|a}$	$F_{c\|a}$
	b	$F_{a\|b}$	TP_b	$F_{c\|b}$
	c	$F_{a\|c}$	$F_{b\|c}$	TP_c

Categorical cross-entropy, a function commonly used for multiclass classification tasks, was used for the loss calculation. This function is also usually called softmax loss (Equation. 5). Accuracy, loss rate, and F1-score will be evaluated to determine the quality of the built model. A model's efficacy correlates directly with its accuracy, particularly when the gap between validation and training accuracy is minimal. A high F1-score indicates the model's ability to effectively classify each class. A significant disparity between validation and training accuracy characterizes overfitting. Conversely, a lower loss rate value (closer to 0), with minimal divergence between validation and training loss, generally signifies a more effective model.

RESULTS AND DISCUSSIONS

The training and evaluation process was followed, and the results were analyzed and visualized. Five models were trained to assess the impact of different dropout rates with varying percentages (50%, 60%, 70%, 80%, and 90%). Figure 6 illustrates that the LSTM model with a 50% dropout rate consistently outperformed the others, demonstrating optimal and stable results. In contrast, models with higher dropout rates (60%, 70%, 80%, and 90%) exhibited slightly overfitting and lower validation accuracy.

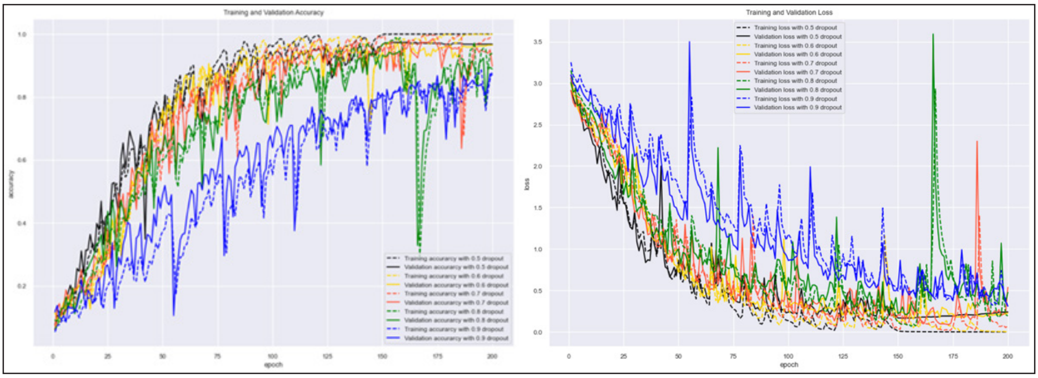

Figure 6. Model training result Accuracy Chart Comparison (left) and Loss Chart Comparison (right). This chart shows the model's accuracy and loss over 200 epochs, making it possible to evaluate the difference in accuracy and loss between the training and validation phases and whether there are any abnormalities

Table 3 demonstrates that the highest achievable accuracy was obtained with a dropout rate of 70%, reaching up to 98.53% validation accuracy and 99.70% test accuracy when the *early_stopping* function was implemented. This function terminates the training process based on specified parameters, such as validation accuracy. However, a *monitor_callback*

Table 3
Model performance comparison

Models (Dropout)	loss	accuracy	val_loss	val_accuracy	Epochs-n
MP-LSTM (0.5)	**0.00052933**	**100%**	**0.24167494**	**96.77%**	**200**
Best MP-LSTM (0.5)	**0.00447017**	**100%**	**0.16992576**	**97.36%**	**155**
MP-LSTM (0.6)	0.0050257	99.92%	0.22635585	96.48%	200
MP-LSTM (0.7)	0.0704495	98.75%	0.53832334	89.73%	200
Best MP-LSTM (0.7)	**0.01964993**	**99.70%**	**0.08934013**	**98.53%**	**173**
MP-LSTM (0.8)	0.19443941	93.82%	0.47621825	88.85%	200
MP-LSTM (0.9)	0.31087446	88.16%	0.31144518	87.09%	200

function was employed, providing checkpoints and indicating optimal training performance. This function continued the training process until this research's predetermined epoch parameter value reached 200. Consequently, the best results were selected to showcase the performance up to 200 epochs. The LSTM model's loss value in the 173rd epoch training process, using a 70% dropout rate, was 0.0196 out of 200, while the validation loss was 0.0893.

By not stopping the training process, the model's performance after the most optimal point during the training process, where the model's performance starts to decline, can also be visualized. In the LSTM model with a 50% dropout, the performance declines slowly after 155/200 epochs, which means the optimal training point is at the LSTM model generated at training epoch 155/200. Meanwhile, Figure 6 shows that the model with 70% has an optimal point at epoch 173/200, which then experiences a volatile performance decline and, at some point, is very significant. The training results of the LSTM model use a 50% dropout rate, as seen in Figure 6. Training accuracy is 100%, and validation accuracy is 97.36%. Likewise, the validation loss score value from the results obtained at the 200th epoch was 0.2417; at the 155th epoch, it was 0.1699.

The confusion matrix of the model resulting from the training process using the built LSTM model is shown in Figure 7. The result is that the number of misclassifications is 2/12

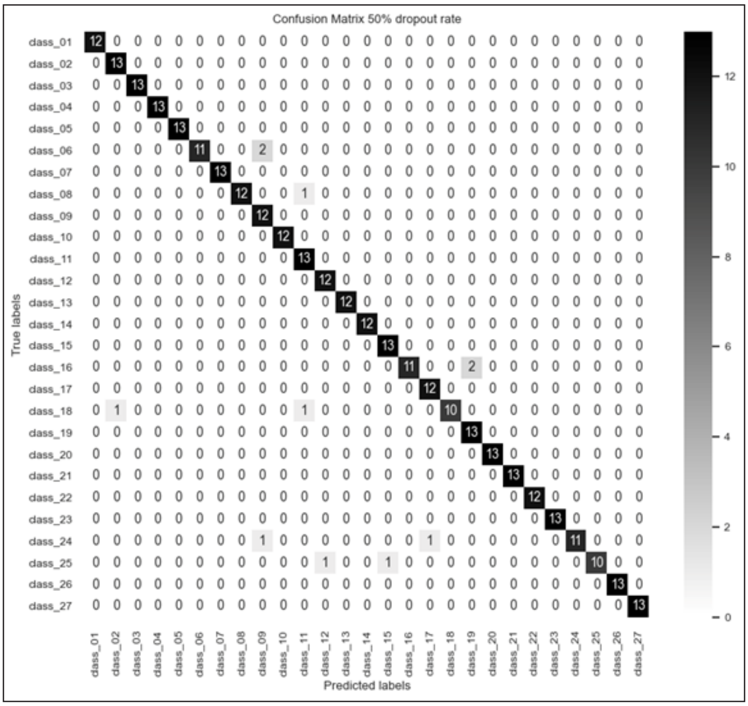

	class_01	class_02	class_03	class_04	class_05	class_06	class_07	class_08	class_09	class_10	class_11	class_12	class_13	class_14	class_15	class_16	class_17	class_18	class_19	class_20	class_21	class_22	class_23	class_24	class_25	class_26	class_27
class_01	12	0	0	0	0	0	0	0	0	0	0	0	0	0	0	0	0	0	0	0	0	0	0	0	0	0	0
class_02	0	13	0	0	0	0	0	0	0	0	0	0	0	0	0	0	0	0	0	0	0	0	0	0	0	0	0
class_03	0	0	13	0	0	0	0	0	0	0	0	0	0	0	0	0	0	0	0	0	0	0	0	0	0	0	0
class_04	0	0	0	13	0	0	0	0	0	0	0	0	0	0	0	0	0	0	0	0	0	0	0	0	0	0	0
class_05	0	0	0	0	13	0	0	0	0	0	0	0	0	0	0	0	0	0	0	0	0	0	0	0	0	0	0
class_06	0	0	0	0	0	11	0	0	2	0	0	0	0	0	0	0	0	0	0	0	0	0	0	0	0	0	0
class_07	0	0	0	0	0	0	13	0	0	0	0	0	0	0	0	0	0	0	0	0	0	0	0	0	0	0	0
class_08	0	0	0	0	0	0	0	12	0	0	1	0	0	0	0	0	0	0	0	0	0	0	0	0	0	0	0
class_09	0	0	0	0	0	0	0	0	12	0	0	0	0	0	0	0	0	0	0	0	0	0	0	0	0	0	0
class_10	0	0	0	0	0	0	0	0	0	12	0	0	0	0	0	0	0	0	0	0	0	0	0	0	0	0	0
class_11	0	0	0	0	0	0	0	0	0	0	13	0	0	0	0	0	0	0	0	0	0	0	0	0	0	0	0
class_12	0	0	0	0	0	0	0	0	0	0	0	12	0	0	0	0	0	0	0	0	0	0	0	0	0	0	0
class_13	0	0	0	0	0	0	0	0	0	0	0	0	12	0	0	0	0	0	0	0	0	0	0	0	0	0	0
class_14	0	0	0	0	0	0	0	0	0	0	0	0	0	12	0	0	0	0	0	0	0	0	0	0	0	0	0
class_15	0	0	0	0	0	0	0	0	0	0	0	0	0	0	13	0	0	0	0	0	0	0	0	0	0	0	0
class_16	0	0	0	0	0	0	0	0	0	0	0	0	0	0	0	11	0	0	2	0	0	0	0	0	0	0	0
class_17	0	0	0	0	0	0	0	0	0	0	0	0	0	0	0	0	12	0	0	0	0	0	0	0	0	0	0
class_18	0	1	0	0	0	0	0	0	0	0	1	0	0	0	0	0	0	10	0	0	0	0	0	0	0	0	0
class_19	0	0	0	0	0	0	0	0	0	0	0	0	0	0	0	0	0	0	13	0	0	0	0	0	0	0	0
class_20	0	0	0	0	0	0	0	0	0	0	0	0	0	0	0	0	0	0	0	13	0	0	0	0	0	0	0
class_21	0	0	0	0	0	0	0	0	0	0	0	0	0	0	0	0	0	0	0	0	13	0	0	0	0	0	0
class_22	0	0	0	0	0	0	0	0	0	0	0	0	0	0	0	0	0	0	0	0	0	12	0	0	0	0	0
class_23	0	0	0	0	0	0	0	0	0	0	0	0	0	0	0	0	0	0	0	0	0	0	13	0	0	0	0
class_24	0	0	0	0	0	0	0	0	1	0	0	0	0	0	0	0	1	0	0	0	0	0	0	11	0	0	0
class_25	0	0	0	0	0	0	0	0	0	0	0	1	0	0	1	0	0	0	0	0	0	0	0	0	10	0	0
class_26	0	0	0	0	0	0	0	0	0	0	0	0	0	0	0	0	0	0	0	0	0	0	0	0	0	13	0
class_27	0	0	0	0	0	0	0	0	0	0	0	0	0	0	0	0	0	0	0	0	0	0	0	0	0	0	13

Figure 7. Confusion matrix of LSTM with 50% Dropout. This confusion matrix compares ground truth labels and prediction labels produced by the LSTM model with a 50% Dropout rate

misclassifications on two samples of test data and 2/13 misclassifications on four samples of test data. The highest percentage of misclassification is 15.384%, which is quite high, with the number of test data only reaching 12–13 samples, but in terms of performance, this is very good. The time required for the training process with data dimensions of reaches 2 minutes, 39.1 seconds, where the training process is considered very fast with 32 *batch_size* at 200 epochs.

CONCLUSION

This research was conducted to look at the performance of the hand landmark classification method, which can be obtained using MediaPipe Hands on dynamic hand gesture datasets. The dataset for dynamic hand gesture recognition systems with 27 classes and 21 different subjects, with each subject producing three different samples for each class, was used in this study. The result is that the hand landmark classification method, successfully used in previous studies using static hand gesture datasets (Ahmad et al., 2022; Ahmad et al., 2023), also works well for dynamic hand gesture datasets.

In this study, long short-term memory architecture is used to handle temporal features in the dataset, resulting in 100% accuracy training results with a validation accuracy that can achieve 97.36% for a 50% dropout rate, and 99.71% accuracy, 98.53% validation accuracy for 70% dropout rate. The misclassification rate with four classes from the dataset only reaches 15.38%, with more than that being less than that percentage. The F1-score, another performance metric used to evaluate the model, was 96.77% for the macro average F1-score at the 200th epoch, indicating the model's strong performance in classifying hand gestures with 27 different classes.

The model's demonstrated efficacy suggests its potential for widespread integration across diverse domains, including industrial machinery, mining equipment, and healthcare. This integration will contribute to developing more intuitive user interfaces, particularly in contexts where traditional input devices pose challenges due to safety or practicality concerns. Future research endeavors will involve the application of the proposed method to our self-curated dataset of natural hand gestures collected for human-robot interaction, human-computer interaction, and dynamic hand gestures in virtual reality. These studies will comprehensively evaluate the method's practical applicability by employing significantly larger datasets.

ACKNOWLEDGEMENT

This research was supported by the MEXT Scholarship from the Ministry of Education, Culture, Sports, Science and Technology, Japan.

REFERENCES

Ahmad, K. A., Silpani, D. C., & Yoshida, K. (2022). Hand gesture recognition by hand landmark classification. *International Symposium on Affective Science and Engineering*, *2022,* Article 8. https://doi.org/10.5057/isase.2022-C000026

Ahmad, K. A., Silpani, D. C., & Yoshida, K. (2023). The impact of large sample datasets on hand gesture recognition by hand landmark classification. *International Journal of Affective Engineering*, *22*(3), 253–259. https://doi.org/10.5057/ijae.ijae-d-22-00022

Camargo, V. P. D., Balancieri, R., Teixeira, H. M., & Guerino, G. C. (2021, October 18-22). *Touchless modalities of human-computer interaction in Hospitals*. [Paper presentation]. Proceedings of the XX Brazilian Symposium on Human Factors in Computing Systems, Sao Paulo, Brazil. https://doi.org/10.1145/3472301.3484328

Fang, Y., Wang, K., Cheng, J., & Lu, H. (2007, July 2-5). *A real-time hand gesture recognition method*. [Paper presentation]. IEEE International Conference on Multimedia and Expo, Beijing, China. https://doi.org/10.1109/icme.2007.4284820

Fronteddu, G., Porcu, S., Floris, A., & Atzori, L. (2022). A dynamic hand gesture recognition dataset for human-computer interfaces. *Computer Networks*, *205*, Article 108781. https://doi.org/10.1016/j.comnet.2022.108781

Hakim, N. L., Shih, T. K., Kasthuri Arachchi, S. P., Aditya, W., Chen, Y. C., & Lin, C. Y. (2019). Dynamic hand gesture recognition using 3DCNN and LSTM with FSM context-aware model. *Sensors*, *19*(24), Article 5429. https://doi.org/10.3390/s19245429

Hochreiter, S., & Schmidhuber, J. (1997). Long short-term memory. *Neural Computation*, *9*(8), 1735–1780. https://doi.org/10.1162/neco.1997.9.8.1735

Sharma, R. P., & Verma, G. K. (2015). Human computer interaction using hand gesture. *Procedia Computer Science*, *54*, 721–727. https://doi.org/10.1016/j.procs.2015.06.085

Srivastava, N., Hinton, G., Krizhevsky, A., Sutskever, I., & Salakhutdinov, R. (2014). Dropout: A simple way to prevent neural networks from overfitting. *The Journal of Machine Learning Research*, *15*(1), 1929-1958.

Rehman, M. U., Ahmed, F., Attique Khan, M., Tariq, U., Alfouzan, F. A., Alzahrani, N. M., & Ahmad, J. (2021). Dynamic hand gesture recognition using 3D-CNN and LSTM networks. *Computers, Materials & Continua*, *70*(3), Article 4676. https://doi.org/10.32604/cmc.2022.019586

Zhang, F., Bazarevsky, V., Tkachenka, A., Sung, G., Chang, C. L., & Grundmann, M. (2020). *Media pipe hands: On-device real-time hand tracking*. arXiv. https://doi.org/10.48550/arXiv.2006.10214

REFEREES FOR THE PERTANIKA
JOURNAL OF SCIENCE & TECHNOLOGY

Vol. 33 (S2) 2025

The Editorial Board of the Pertanika Journal of Science and Technology wishes to thank the following:

Alvin Lim Teik Zheng
UPM, Malaysia

Norhisam Misron
UPM, Malaysia

Ribhan Zafira
UPM, Malaysia

Shyam S. Pandey
Kyutech, Japan

Siti Anom Ahmad
UPM, Malaysia

Yoshiaki Ushifusa
The University of Kitakyushu, Japan

Kyutech – *Kyushu Institute of Technology*
UPM – *Universiti Putra Malaysia*

Pertanika Journal of Science & Technology
Vol. 33 (S2) 2025

Content

e-ISSN 2231-8526
9 772231 852000

ISSN 0128-7680
9 770128 768083

Pertanika Editorial Office, Journal Division,
Putra Science Park,
1st Floor, IDEA Tower II,
UPM-MTDC Center,
Universiti Putra Malaysia,
43400 UPM Serdang,
Selangor Darul Ehsan
Malaysia

http://www.pertanika.upm.edu.my
Email: executive_editor.pertanika@upm.edu.my
Tel. No.: +603- 9769 1622

PENERBIT
UPM
UNIVERSITI PUTRA MALAYSIA
BERILMU BERBAKTI
PRESS

http://penerbit.upm.edu.my
Email: penerbit@upm.edu.my
Tel. No.: +603- 9769 8855